Reconfiguring Colloidal Solids with Defects Using Active Matter
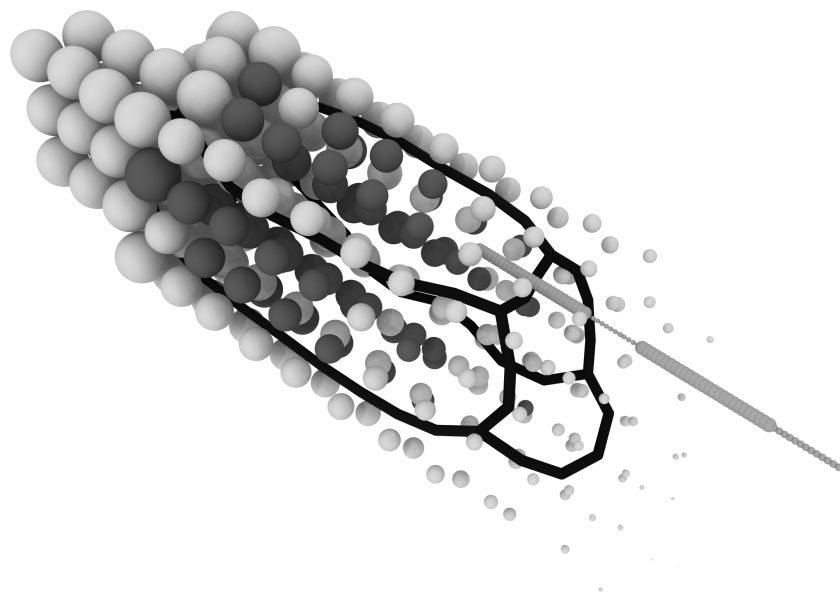
by

Bryan VanSaders

A dissertation submitted in partial fulfillment
of the requirements for the degree of
Doctor of Philosophy
(Materials Science and Engineering)
in the University of Michigan
2019

Doctoral Committee:

Professor Sharon C. Glotzer, Chair
Assistant Professor Yue Fan
Assistant Professor Liang Qi
Professor Michael J. Solomon

Bryan VanSaders

bvansade@umich.edu

ORCID: 0000-0001-6469-4329

Dedicated to my family; my parents and sisters who have always supported me, and Jill, the start of my new family. They have kept me afloat.

Acknowledgments

Firstly I would like to thank my adviser, Professor Glotzer for providing a great environment for my research. I've always felt like I had the freedom to do the work that excited me. Her enthusiasm made doing the research fun, and her support and trust is the reason that this dissertation exists. I would also like to thank my committee members, Professors Solomon, Qi, and Yue. At various times you have all been sounding boards for my ideas and helped me navigate the idea of life after graduate school.

The entire Glotzer research group deserves an acknowledgment. It has been a welcoming and invigorating place to think about science. From help with any and every problem to great friendships, I feel truly spoiled to have worked with such a group of people. Dr. Julia Dshemuchadse has in particular been a wonderful mentor and collaborator. Furthermore, essentially all of my work presented in this dissertation depends on the efforts of many Glotzer group members, current and past, who built and maintained the excellent computational tools we use. Dr. Josh Anderson deserves special mention as the computational heart-and-soul of the group, but many others including Dr. Matthew Spellings and Dr. Jens Glaser made software without which my work would not have even gotten started. The whole group owes a lot to Karen Coulter, who is really our best defense against the general chaos of so many researchers working together on so many different projects. Beyond our group, I have enjoyed collaborating with Professor Solomon and two of his students, Peng-Kai Kao and Tianyu Liu. We have managed to pack a lot of topics into our projects together, and it has been a pleasure.

It is impossible not to thank my friends and family who supported me throughout my graduate career. I simply would not have made it through these past four years without them. My parents, John and Maryanne, were always there through all the highs and lows. My sisters, Dr. Jen and Morgan, and brother-in-law, Dr. Ben, have been the best siblings I could ask for. From mountain biking in California to Lord of the Rings at Christmas time, you were an important part of my life these years. While Ann Arbor is a fantastic place in itself, it is my friendships that have made this city into a place I will miss dearly. Great friends are hard to come by, and when you find them, they deserve recognition. Many thanks to: James Proctor for preparing me more dinners than I can count; Ben Swerdlow, Kelsey Mengle, and Zach Pritchard for meeting and maybe exceeding my love for board games; and Avi Bregman for general co-conspiring on everything from camping trips to pit roasts. Julia, while also being a fantastic colleague, was a pillar for me during my stay at UM and a vital part of my support 'structure'.

Lastly I would like to thank my partner, Jill. Our relationship very nearly covers the whole span of my graduate studies here, and you deserve an acknowledgment on everything I've done.

TABLE OF CONTENTS

Chapter

LIST OF FIGURES

Figure

LIST OF APPENDICES

Appendix

ABSTRACT

Engineering defect configurations within atomic crystalline materials, particularly metals, is a cornerstone of material science. Crystalline defects affect every facet of a material's properties, and in this regard, crystals composed of colloidal particles are no different from their atomic analogues. What is different, at the colloidal scale, is that new techniques have been developed to allow for the application of local forces by independently operating μm-scale particles. The capacity of such *active* matter to manipulate, produce, and remove colloidal defects is only just starting to be explored. This dissertation seeks to establish the feasibility of directly controlling crystalline defects through the action of a particle species that exerts work locally, via computer simulation. The goals of such microstructure manipulation are to create materials with dynamic properties that change in response to external stimuli. Dynamic modification of crystallite shape, optical properties, or mechanical properties such as resistance to deformation are examples of what can be achieved through the action of active particles strongly coupled to colloidal defects. This dissertation is built around four studies of the behavior of defects in colloidal materials.

First, I examine the nature of dislocations in crystals composed of particles interacting through repulsive pair potentials. By comparing attractive potentials to a family of repulsive ones with differing slopes, I explore the changes to mechanical properties and dislocation structure that occur as entropy comes to dominate the deformation free energy of a material. By comparing the deformation free energy of materials across a collection of strain modes, I introduce a way to compare systems composed of attractive particles with systems of repulsive particles bound together by pressure. By varying the confining pressure, I find that attractive and repulsive systems can be matched in material properties. Furthermore, I investigate the strain fields that surround disloca-

tions in these materials. I find that the framework of linear elasticity is most applicable to hard particle systems at pressures near the melting transition. As the pressure is further increased, the range of linear elastic behavior shrinks and greater tension-compression asymmetry arises. This study demonstrates that colloidal solids near their melting pressure can be analyzed and engineered for mechanical properties using well-established formalisms developed for atomic systems.

Second, I study the interactions between colloidal dislocations and anisotropic interstitial particles that are capable of exerting local forces. By representing this interstitial by the strain field it produces when embedded in the crystal, I formulate a method of optimizing the interaction of the dislocation and interstitial by allowing the strain field to fluctuate. Once an optimal strain field is found, this field is mapped back to an interstitial particle geometry that produces it. The mapping between strain field and geometry is achieved using the method of eigenstrains, which allows for rapid prediction of strain fields without any particle-based simulation. As a result, the optimization can be carried out very quickly compared to schemes requiring molecular dynamics simulation to assess a trial geometry's fitness. I study the interaction of interstitials with straight edge dislocations and dislocation loops. Dislocation loops are found to be capable of stronger binding to optimized interstitials due to the way that dislocation bending localizes strain fields. By molecular dynamics simulation of optimized particles with dislocations, I show that both lines and loops can be induced to glide by the action of bound active interstitials.

Third, I explore the interaction of active rod-like interstitial particles with stacking faults in face-centered cubic colloidal crystals of repulsive spheres. I find that certain geometries of active interstitials are capable of efficiently searching through a crystal and binding strongly to a stacking fault. High mobility and strong binding of the active interstitial are antagonistic properties, both primarily controlled by the length of the active rod. I find that active rod length influences mobility and binding by changing the probability of reorientation. Active rods that compromise between high mobility and strong binding to stacking faults are able to impede the motion of partial dislocation pairs. They rapidly encounter the stacking faults that link partial dislocations in the FCC crystal, and when absorbed provide an additional barrier to dislocation glide. The presence of

such optimized active, stacking-fault seeking interstitials can be detected in the shear deformation properties of dislocated crystals even at concentrations as small as 64 per million host particles.

Fourth, I explore how a crystalline colloidal robot could be reconfigured using shear displacements resulting from the biased migration of dislocations. I propose a means of creating and controlling the migration of dislocations in 2D colloidal crystals based on embedded clusters of particles capable of changing size. I discuss how such clusters should produce dislocation pairs on a single glide plane, with consistent dislocation biasing. The geometry of the cluster is a key parameter; effective clusters have anisotropies that result in the necessary biasing. I show that for clusters of particular geometries, cyclic expansion and contraction of their constituent particles produce dislocations that accumulate slip. Single or multiple slip planes can be used to reshape the boundaries of a 2D colloidal crystallite.

Lastly, I conclude with an overview of all chapters, emphasizing how these studies are part of an overarching investigation. I also discuss directions for experimental and theoretical future work to continue progressing this interdisciplinary topic.

CHAPTER 1

Introduction

1.1 Colloidal Solids

Colloidal matter refers to substances that are comprised of (at least) two phases, with one phase being sub-micrometer (μm) particles immersed in the other fluid-like phase. Familiar examples of colloidal suspensions include milk, fog, and clay [1]. Recently, sophisticated synthesis techniques have been developed that allow direct control over a variety of colloidal particle properties [2, 3]. This new-found control has driven an explosion of research into how such colloidal materials can be designed for exotic or exceptional material properties.

At colloidal length scales, individual particles behave less like familiar macroscopic objects (i.e. grains of sand) and more like 'large atoms', in the sense that thermal fluctuations cause them to randomly diffuse and explore their environment. This motion, the product of atomic collisions with the fluid environment, is known as Brownian motion. Such incessant movement results in ergodic sampling of the configuration space of systems of colloidal particles. This means, in essence, that the probability of observing a configuration of colloids is directly related to the free energy of that configuration. By leveraging powerful statistical methods initially developed for use in atomic systems, collective properties of large numbers of particles (for instance, bulk modulus [4], equations of state [5] and phase transitions [6]) can be predicted.

A topic of intense interest in the past several decades has been phase transitions between a dispersed, fluid-like arrangement of colloidal particles and a condensed solid-like arrangement

with crystalline ordering. Even in the simplest of cases, i.e. with the only interaction between particles being that they cannot overlap each other, many distinct crystalline phases can be obtained depending upon the shape of the colloids [7, 8, 9, 10, 11, 12, 13, 14, 15, 16]. Many schemes exist for inducing attractive interactions between colloids, including depletion [17, 18, 19, 20], DNA functionalization [21, 22, 23, 24], and electric field interactions [25, 26, 27, 28], among others [29]. Consequently, there is a large variety of crystalline colloidal materials that have been realized experimentally and predicted computationally.

Such crystalline assemblies present enticing opportunities to materials scientists. When designing a material, we are limited by the atoms themselves; they cannot be engineered for specific properties or functionalities. In a colloidal crystal however, much ingenious work has shown that a great deal of functionality and tailored properties can be bestowed upon individual sub-μm scale particles. This raises tantalizing possibilities for the design of colloidal *metamaterials* that have exotic properties not possible with a traditional material. Information storage, properties that change in response to stimuli, self-healing, and shape reconfiguration are examples of properties that next-generation materials science seeks to realize with colloidal materials.

1.2   Colloidal Solids as Metamaterials

Metamaterial [30] is a term referring to a material comprised of designed subunits (which are each composed of many atoms). The designed subunits are sometimes referred to as *meta-atoms* and are often treated as the fundamental unit of the material. Metamaterial research has been particularly successful in producing materials with exotic optical properties [31]. Metamaterials that produce exceptional mechanical [32] or acoustic [33] properties have also been explored. I will focus on two areas in this introduction, mechanical and optical, in which colloid-based metamaterials have been shown to be promising.

1.2.1 Mechanical Applications

A colloidal metamaterial is held together by inter-particle forces that are generally weaker per unit volume than the forces that bind together atomic materials. Therefore, it is unreasonable to attempt to create an exceptionally strong material composed of colloidal particles. However, other properties, such as phononic spectra, can be engineered by tuning the composition or length scale of a colloidal solid [34]. Furthermore, it is now possible to create colloids with the ability to exert work individually and independently [35], so-called *active* matter.

The most commonly studied varieties of active colloids are capable of directed or self-propelled motion. This has several interesting consequences, most obviously for materials with switchable properties. A recent example are so-called 'living crystals' [36], which are self-propelled under illumination by ultraviolet light. When self-propelled, particle-particle collisions lead to the formation of clusters that behave like a condensed phase. Similarly, the emergent interactions of magnetic colloidal particles driven by rotating external magnetic fields have been exploited to demonstrate a variety of behaviors and functionalities [37, 38, 39, 40, 41]. Beyond self-propulsion, out-of-equilibrium processes such as DNA conformation changes [42] have been used to produce crystals of nanoparticles that expand or contract in response to environmental signals.

These examples collectively suggest a future colloidal metamaterial capable of dynamic reconfiguration and mechanical property change in a manner similar to the cytoskeletal matrix of single-celled organisms. Such organisms have sophisticated assemblies of macromolecules that permit the growth of appendages to engulf food or move in their environment [43, 44]. Fittingly, much work on active materials is concerned with liquid crystals composed of actin filaments that are extracted from cells and induced to activity by the application of biological agents [45]. A robotic device of sufficiently small scale would require a material with similar capabilities to interact with and control its environment. To successfully realize the dream of a fully artificial cellular-scale robot, a synthetic medium capable of similar mechanical property changes is needed.

1.2.2 Optical Applications

A wide variety of interesting optical properties have been realized using designed meta-atoms. Notable examples are the prediction and realization of metamaterials capable of optical cloaking [46, 47] and negative refraction [48, 49]. However even simple meta-atoms (particles composed of a single material) arranged in a crystalline structure can produce useful optical effects. If the assembly has variations in refractive index that are on the same length scale as the wavelength of optical light, intense wavelength- and angle-dependent reflections can occur [50]. The brilliant colors of opals are one natural example. Certain crystal structures have wavelength ranges over which all angles of incident light are totally reflected, known as a 'photonic bandgap'. Wavelengths within the gap evanescently decay (without absorption) in the crystal bulk [51].

1.3 Defects and Material Properties

When a material is crystalline, the presence of defects can have dramatic impact on the material properties of the solid. The engineering of defect configurations (referred to as 'microstructure' in the structural metals community) has been a major factor in the improvement of engineering alloys. This is because the plastic deformation properties of a crystalline material depend sensitively on the quantity, arrangement, and nature of defects within it. Finding new methods to produce, remove, or reconfigure defects allow us to exercise control over the mechanical properties of metals [52]. Similar techniques can be applied to colloidal crystals. The resistance of a colloidal crystal to plastic deformation could be modified dynamically if defects within it could be manipulated in response to external stimuli by local work exerted by active particles.

Defects also dominate other colloidal metamaterial properties of interest. The optical properties of structural color and photonic bandgaps are highly sensitive to the ordering (or lack thereof) in the crystalline assembly. In the past several decades a large number of computational and experimental studies have been conducted that demonstrate how defects in photonic materials can be fashioned into functional devices [53, 54, 55, 56, 57, 58] A linear break in crystalline order,

for example, produces a path of propagation for frequencies of light not permitted to propagate in the photonic crystal bulk [53, 54]. The details of this defect path can produce a variety of useful effects, such as power-splitting at junctions, low loss at sharp bends, or designed phase delaying. To date, these studies have employed photolithography techniques to create defective photonic crystals from the 'top down', resulting in a fixed final structure. The possibility of mobile, reconfigurable defects raises interesting potentialities for photonic circuits. Consider the possibility of moving two waveguiding paths together (and in so doing creating a junction). Optical junctions that could be brought together and split apart, perhaps in response to environmental cues, would be an important step towards the realization of neuromorphic optical computing.

The ability to (dynamically) specify a defect configuration for crystalline materials has many advantages for material property and functional device engineering. The way in which this dissertation explores how to manipulate defect microstructure is by coupling active particles in the colloidal assembly to *dislocations*. At a fundamental level, dislocations are responsible for much of the internal reconfiguration that occurs when crystalline materials change shape. By taking control of dislocations, we gain the ability to both modify the presence of other defects within a colloidal crystallite or change its shape through the action of internal work dissipation.

1.4   Dislocations

If we wish to reshape or reconfigure a material, we can state this goal in another way; we wish to transport mass through the material. When we consider a condensed, crystalline phase, this goal seems inherently difficult. Close-packed crystals (which are the easiest crystals to form from excluded volume interactions) are crowded environments, lacking room to redistribute their constituent (meta)atoms without collective rearrangement. The resolution of this problem arises naturally in the form of the dislocation. Dislocations are linear defects in crystals that have a distinct pattern of elastic deformation surrounding them. Dislocations were first theoretically considered by mathematicians studying singularities in isotropic elastic media [59, 60] in the early 1900s, but

they were not connected to the behavior of metals until long after the discovery of x-rays and the crystallinity of metals.
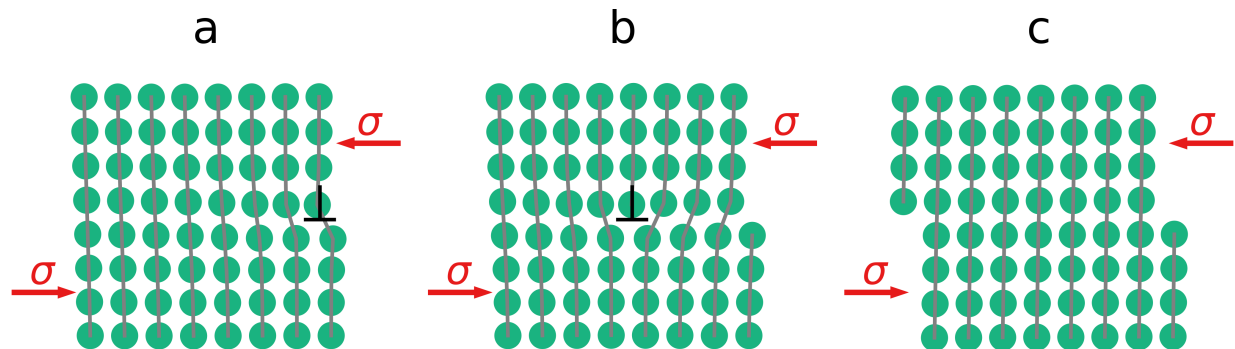
Figure 1.1: **a** A simplified crystal domain under shear stress (red arrows). Shear has resulted in a misalignment of lattice planes in the top half relative to the bottom. The location of maximum misalignment is the dislocation core (indicated by ⊥). **b** The dislocation propagates into the crystal. As it passes, lattice sites in the top half-space shift neighbors in the bottom half-space over to the left. **c** The dislocation has passed fully through the crystal, leaving a domain with no elastic shear but a permanent surface deformation. At macroscopic scales, plastic shear is the result of many such dislocation passages.

The shearing of a discretized material occurs by the switching of neighbor bonds. Within a crystal, if all bonds across a plane are cut, and the top half-space shifted relative to the bottom-half space and re-attached, then some amount of permanent shear deformation occurs. In 1926 Frenkel [61] showed that reasonable theoretical estimates of the force required to deform metals by such a mechanism was many orders of magnitude larger than the forces that experimentally deformed metals. It was hypothesized that bonds between atoms were being switched locally in the vicinity of mobile defects, which lowered the shear required for plastic deformation. Between 1934-1939, the atomic structure and properties of dislocations were proposed by Orowan, Taylor, Polanyi, and Burgers [62, 63, 64, 65], and experimental evidence was found soon after to support the dislocation mechanism of deformation [66]. These dislocation defects could be linked back to the theoretical elastic singularities postulated before the discovery of metal's crystalline structure.

The process of local bond switching that occurs as a dislocation propagates through a crystal is shown in Fig. 1.1. Under external shear stress, a dislocation (core indicated by ⊥) is driven to move in its glide plane (or created, if none existed initially). Near the dislocation core, distortions

to the lattice positions are large. However, after it has passed all elastic strains are relaxed and neighbor bonds that crossed the glide plane of the dislocation have been exchanged. The end result is the same as cutting all bonds and shifting the crystal above the glide plane relative to the region below the glide plane. The distance of the slip in the glide plane produced by a dislocation is set by a topological quantity of the defect known as the *Burgers vector*, $\vec{b}$ [67].
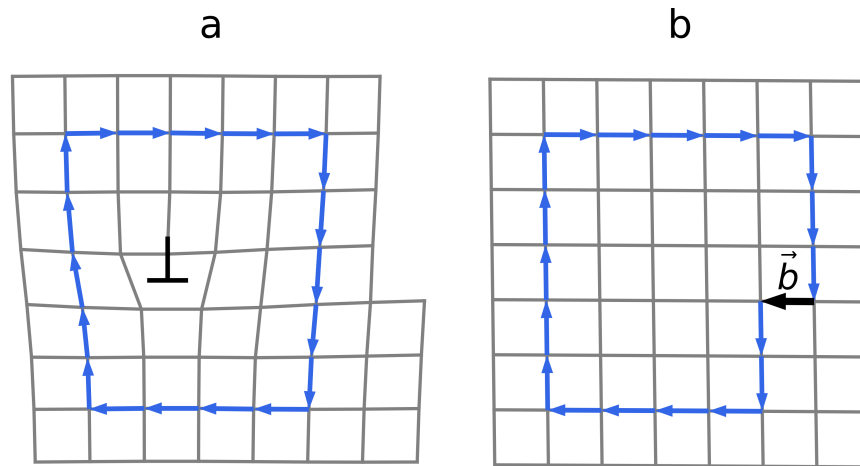
Figure 1.2: **a** A simplified crystal with a dislocation ($\perp$). A loop, drawn by hopping from lattice point to neighboring lattice point, encloses the dislocation core. **b** The same loop, drawn in a crystal without a dislocation, fails to close. The vector that completes the loop ($\vec{b}$) is the Burgers vector of the dislocation.

The Burgers vector is visually defined in Fig. 1.2. A path drawn by hopping from lattice site to neighboring lattice site around a dislocation core will not form a closed path if repeated in a dislocation-free crystal. The specifics of the path are irrelevant; if the path encloses the dislocation, then the closure failure in the dislocation-free crystal will be equal to the Burgers vector. The relationship between $\vec{b}$ and the dislocation's line direction, $\vec{l}$ (in Fig. 1.2, the dislocation core extends out of the plane of the page) determines the glide plane. Dislocation motion in the glide plane has a low activation energy compared to motion out of the glide plane (which is called *climb*). Generally, the glide plane is the plane that contains both $\vec{b}$ and $\vec{l}$. When $\vec{b}$ is perpendicular to $\vec{l}$ (as shown in these schematics), the dislocation is called an *edge* dislocation. When $\vec{b}$ is parallel to $\vec{l}$, the dislocation is called a *screw* dislocation. Screw dislocations do not have a unique plane that contains both $\vec{b}$ and $\vec{l}$, and so they are not confined to move in a single plane. Dislocations can

be curved or have mixed edge-screw character. They can also undergo reactions that conserve the vector sum of $\vec{b}$ [67].

Dislocations act as the fundamental unit of rearrangement within a crystal. Other mechanisms that transport mass through a crystal are based on the migration of vacancies and self-interstitials. Dislocation migration can be many orders of magnitude faster than point-defect mediated transport in isotropically bonded materials [67]. In Fig. 1.1, the dislocations are motivated to glide by the application of shear stress across the entire crystal domain. However, this need not be the case. Dislocations can also be motivated to glide by local stress fields. The classic example of local stress manipulating dislocations is a nanoindentation experiment, in which a tip of nm scale diameter is indented into a metal surface. This local deformation drives the creation and migration of dislocations [68].

Fundamentally, dislocations are important to the deformation of materials that are 1) crystalline and 2) have predominantly isotropic bonding between their subunits (atoms or meta-atoms). The archetypical colloidal metamaterial is the face-centered cubic (FCC) hard sphere crystal, which has isotropic inter-particle interactions. Therefore dislocations dominate the deformation of this material, as evidenced by experimental observation [69, 70]. Generally, we expect large classes of colloidal assemblies with isotropic or near-isotropic interactions to deform via mechanisms that would be familiar to a metallurgist.

The large scale of colloidal crystals means that defects can be directly imaged with optical microscopes. Several studies [69, 70, 71] have reported observation of dislocation creation and migration in experiments that mimic indentation experiments on a larger (i.e. colloidal) length scale. Due to the ease of characterization, more has been done to study 2D dislocations in sheets of colloidal particles [72, 73, 74]. The dynamics of dislocations in colloidal metamaterials generally behave the same as their atomic counterparts. This equivalence suggests that the insights that have been accumulated about the behavior of atomic dislocations can point us forward in understanding how to manipulate defects in crystalline colloidal metamaterials.

However, there is a greater opportunity in colloidal metamaterials to apply local forces than

8

in atomic systems. The large scale of colloidal particles allows for the application of external fields, such as optical tweezers [73, 74] or magnetic fields. These forces can be applied directly to defects in order to manipulate them, which is not possible in atomic materials. Individual particles themselves are also large enough to be designed to exert work locally through chemical reactions [75, 76, 77, 78].

1.5 Dislocations as Tools for Colloidal Crystal Reconfiguration

We have seen that the deformation of a colloidal metamaterial can be controlled by focusing on the dynamics of its defects. Using locally generated stresses to motivate or arrest the motion of defects could deform (reshape) or strengthen a colloidal material. If change in defect behavior was linked to an environmental signal, then a mechanically-adaptive material would result. Such a material would be desirable for the creation of μm-scale robotic devices. Furthermore, the internal arrangement of optically useful defects in a photonic crystal could be manipulated by the passage of dislocations. This opens up possibilities for dynamic optical circuits

Moving forward, I focus on how active particles can be strongly coupled to colloidal dislocations, so as to enable reconfiguration functionalities at the μm-scale. To motivate the studies that will be presented, I first give several examples of reconfigurations that could be accomplished with control over colloidal dislocations.

1.5.1 Bending and Grain Boundary Formation

The core of an edge dislocations can be thought of as the terminating line of an extra half plane that has been inserted into a crystal. The dislocation core marks a location where the number of crystal planes changes. For this reason, the density of edge dislocations controls the bending curvature of a crystalline domain. A region of crystal with a high density of dislocations with the same Burgers vector will be curved. Consider a beam built from a colloidal metamaterial with a net-zero Burgers vector, but non-zero dislocation density. If edge dislocations of both handednesses are

9
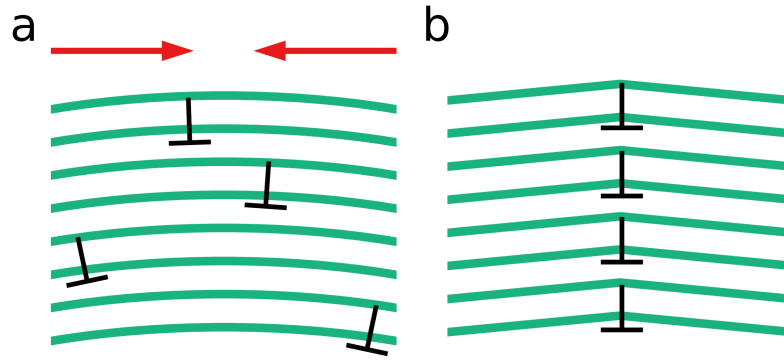
Figure 1.3: **a** A gently curved crystal lattice (green) with distributed edge dislocations (⊥). Forces (red arrows) are applied to the dislocations that collect them in one region. **b** After dislocations have been collected, the crystal has increased local curvature. If this local curvature exceeds a threshold, a misorientation grain boundary can be created.

evenly interspersed within the beam, then it will have little or no long range curvature. If, however, many dislocations with the same $\vec{b}$ are collected together, then the beam will bend. Fig. 1.3 shows how local curvature could be changed by concentrating dislocations with the same $\vec{b}$. The same logic applies to screw dislocations, however their concentration would produce a global twist in a beam.

If same-handedness dislocations are concentrated enough, then a grain boundary can be formed (Fig. 1.3b). This same boundary could be disrupted by bringing in dislocations of the opposite handedness. Local control, precise enough to fractionate dislocations by Burgers vector, could produce arbitrary grain boundaries, or remove them.

1.5.2   Dislocation Slicing

A pair of opposite handed dislocations is known as a dislocation dipole. This configuration can have a zero net Burgers vector (identical opposite handedness dislocations). For edge dislocations, a dipole can be thought of as a finite extra crystal plane (or a finite missing plane). If the pair is moved, the location of the extra (or missing) plane is effectively shifted as well. Similar to how a single edge dislocation results in slip between the crystal regions above and below its glide plane, a dislocation dipole results in slip of the interior region (between the glide planes) relative
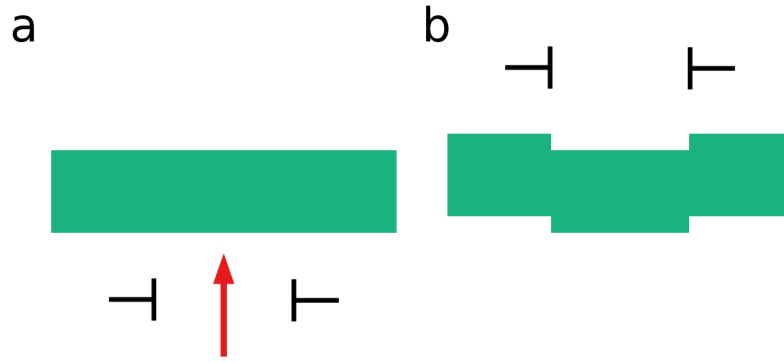
Figure 1.4: **a** Force (red arrow) is applied to a dislocation dipole to drive it towards a coherent grain (green). **b** After passage through the coherent grain, the dipole has roughened the boundaries with a local shift of one Burgers vector.

to the exterior region. Fig. 1.4 illustrates the effect of a dislocation dipole gliding past a coherent crystal grain (green). Here, 'coherent' refers to a region of crystal that is somehow distinct from its surrounding, but shares the same crystal structure, orientation, and mechanical properties. In atomic systems, such a grain might be composed of a different species with very similar atomic radius. In colloidal systems, such a region might be composed of particles that have been tagged with fluorescent dye, or have a difference in optical or chemical properties from the rest of the crystal.

Dislocation dipoles are possible in two and three dimensions, however in 3D dislocation loops are also possible. A dislocation dipole can be thought of as a limiting case of very large loop. Dislocations prefer to be straight [67]; therefore a very large loop will have at its center a region where the dislocations are arranged like a dipole of straight dislocations.

By using multiple passages of dislocation dipoles, the interior of a crystalline domain could be rearranged. This could be particularly useful if the regions contained optically tagged particles or optical defects. Regions of similar optical properties could be disconnected or reattached intentionally to change optical circuit behavior or bulk material optical properties. The creation of bumps on a plane of fluorescently tagged particles, for instance, could in theory be used to store information.

1.5.3 Surface Reorganization
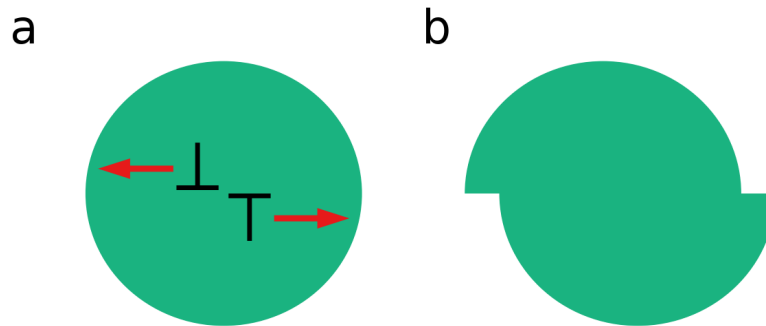
Figure 1.5: **a** A finite crystal domain (green), has a complimentary pair of dislocations created within it. Forces (red arrows) drives these dislocations towards the domain boundary. **b** Upon reaching the surface, dislocations produce step edges with a height of one Burgers vector.

As implied by the discussion of dislocations under shear (Fig. 1.1), edge dislocations that encounter a free surface will be absorbed, leaving behind a step with a height of $\vec{b}$. Were it possible to create dislocations within the bulk of a material, and then direct them as desired to the surface, a sequential reorganization of the surface could be carried out. Fig. 1.5 illustrates how the creation and migration of dislocation pairs can change the cross-sectional shape of a disk of material.

This method of surface reshaping requires both a means to produce dislocations oriented in an arbitrary way as well as a means to direct them towards the free surface to be manipulated. In theory, a wide range of crystallite shape changes are possible using this method. Tasks such as engulfing a target or crawling across a surface could be achieved by the sequential production of many dislocations that reshape the crystallite boundary. Fig. 1.6 schematically shows three such functional operations. In Fig. 1.6a a colloidal crystallite (green) is moved along a wall (gray) by sequential shear displacement. Fig. 1.6b and c show how a target object could be transported and captured by exploiting shape change due to dislocation-induced shear. Such operations are potentially useful for colloidal-scale robots.
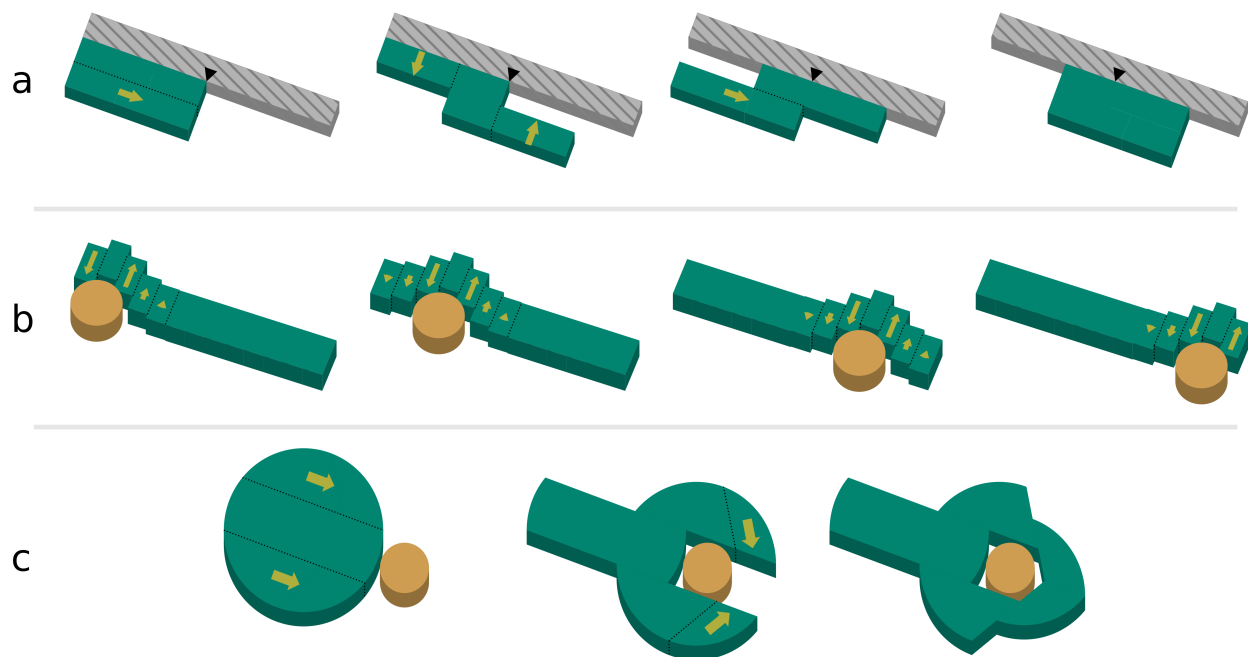
Figure 1.6: Functional reconfigurations that are possible with control of shear displacement on arbitrary planes. Yellow arrows represent planned shear displacements. **a** Locomotion of a colloidal domain (green) against a wall (gray) by sequential shearing. **b** Peristaltic transport of a cargo object (yellow cylinder) by sequential shearing. **c** Cargo (yellow cylinder) capture by sequential shearing.

1.6 Outline

This dissertation is built around four computational studies. In Chapter 2 I begin with a brief overview of the simulation methods and concepts which are common, or fundamental to these studies.

Chapter 3 compares the mechanical properties and dislocation characteristics of crystals composed of a family of repulsive pair potentials. By varying the steepness of the potentials, the mechanical response of the material can be switched from predominantly enthalpic to predominantly entropic. This chapter lays the groundwork for later chapters focused on driving the motion of dislocations. Its contents were published in Ref [79].

In Chapter 4, I introduce a method of optimizing the shape of an active interstitial so as to maximize strain-field-mediated interactions with a colloidal dislocation. Using an FCC crystal of

nearly hard spheres, I demonstrate how active interstitials can be used to drive dislocations to glide. The contents of this chapter were published in Ref [80].

Chapter 5 examines how the shape of an active interstitial controls its binding to void sites in an FCC crystal, as well as its transport properties. I show that the topology of voids found near stacking faults can trap active interstitials of certain sizes, and that this trapping can impede the motion of partial dislocations that are associated with those faults. This chapter is a demonstration of how small quantities of active particles can be used to impact the bulk deformation resistance of a colloidal crystal. The contents of this chapter are as yet unpublished (Ref [81]).

In Chapter 6, I consider a 2D system of attractive colloidal particles that form a crystallite. Embedded within this crystal is a cluster of particles that change their diameter. I show how for certain geometries of embedded clusters, the change in diameter produces dislocation pairs that are driven to the crystallite surface and so affect a change in its shape. While previous chapters focus on controlling preexisting dislocations, this study demonstrates a scheme for producing them on demand, resulting in a more general toolset for crystalline reconfiguration. The contents of this chapter are as yet unpublished (Ref [82]).

Lastly, I conclude in Chapter 7 with a summary and suggestions for further work, both experimental and computational.

CHAPTER 2

Simulation Methods

2.1 Molecular Dynamics Simulation

In this dissertation, the majority of simulations of interacting particles are carried out using an implementation of the molecular dynamics (MD) method. MD is a simulation method in which particles move according to Newton's kinematic laws of motion [83]. An energy-distance relationship is prescribed for particles depending upon their type (a *pair potential*). The derivative of this pair potential defines the interaction forces that particles feel from each other. MD is carried out (typically) in a domain that has periodic boundary conditions, i.e. particles that leave through a box face reappear on the opposite side of the box as though coming from an identical copy of the system. As a result, a maximum range of interaction must be imposed, so as not to encounter a situation where a particle applies a force to itself. Typically, pair potentials are truncated at a much smaller distance than this in order to improve the speed of force calculation. The most basic form of MD is energy-conserving, and corresponds to the NVE (constant number of particles, constant volume, constant energy) thermodynamic ensemble. Common variants are NVT (constant number of particles, constant volume, constant temperature) and NPT (constant number of particles, constant pressure, constant temperature). Most simulations in this dissertation are conducted under a variant of the NPT ensemble.

2.1.1 The Constant Stress Isothermal Ensemble

The constant stress isothermal ensemble ($N\sigma T$) is an extension of the NPT, or isobaric isothermal ensemble. In this realization, the periodic box size and shape is changed according to a stress matrix computed from the sum of all forces acting in the system being simulated. The stress tensor of the system is maintained at a prescribed value by changing the six degrees of freedom that the simulation box has (these are the side lengths and angles between sides). Simultaneously, the velocities of all particles are rescaled so that the total kinetic energy in the system is consistent with a prescribed temperature. This ensemble is essential for simulating solids accurately, especially when said solids are undergoing deformation.

In a simulation with a fixed domain size, crystals that span the simulation box may have stresses induced by a mismatch of the the length of the box and the periodic order of the crystal in that direction. If the intent is to simulate a periodic crystal that is commensurate with the periodic domain of an MD simulation, then an NVT (constant volume) simulation must be carefully set to the correct domain size for the crystal, state point, and orientation of interest. The same result can be obtained without prior detailed knowledge of the crystal's properties (such as, for instance, the thermal expansion coefficient) by simulating the crystal in an $N\sigma T$ domain. Such a simulation will be rescaled by inter-particle forces, and equilibrate at a domain size for which forces driving expansion and contraction of the domain are balanced.

The box matrix is used to define the extent of the periodic domain:

$$
\vec{\mathbf{h}} = \begin{pmatrix} L_x & xyL_y & xzL_z \\ 0 & L_y & yzL_z \\ 0 & 0 & L_z \end{pmatrix} \tag{2.1}
$$

The particles are represented in reduced coordinates, relative to this box matrix. Therefore, when the box matrix is scaled, so too are all the positions of the particles in that box. The box matrix is scaled according to the virial pressure, which is calculated from the tensorial virial theorem

16

$$(P_{int})_{\alpha\beta} = \frac{1}{V} \left[\sum_{i=1}^{N} \frac{(\mathbf{p}_i)_\alpha (\mathbf{p}_i)_\beta}{m_i} + (\mathbf{F}_i)_\alpha (\mathbf{r}_i)_\beta - (\vec{\phi}'\vec{\mathbf{h}}^t)_{\alpha\beta} \right], \qquad (2.2)$$

$$\mathbf{F}_i = -\nabla_{r_i} \phi(\mathbf{r}, \mathbf{V}), \qquad (2.3)$$

$$(\phi')_{\alpha\beta} = \frac{\partial \phi(\mathbf{r}, \vec{\mathbf{h}})}{\partial (h)_{\alpha\beta}}. \qquad (2.4)$$

where i runs over all N particles in the system, α and β reference matrix elements, $\mathbf{p}_i$ is the momentum vector of particle i, $\mathbf{F}_i$ is the force (summed from all sources) acting on particle i, $\mathbf{r}_i$ is the position of particle i in reduced coordinates, and ϕ is the potential energy.

2.2   Stress and Strain

Stress and strain are fundamental concepts which greatly aid in the analysis of anisotropic solids undergoing deformation [85]. If we define an initial configuration $\mathbf{X}$ and an end configuration – reached by homogeneous transformation – $\mathbf{x}$, then we can relate the configurations by a linear transformation

$$x_i = \sum_j \alpha_{ij} X_j. \qquad (2.5)$$

We want a rotationally invariant version of α, because we will explicitly connect it to system free energy, and system free energy should not vary with the rigid rotation of all elements. The Lagrangian strain parameter is a symmetrization of the linear transformation matrix α_{ij},

$$\eta_{ij} = \frac{1}{2} \left(\sum_k \alpha_{ki} \alpha_{kj} - \delta_{ij} \right). \qquad (2.6)$$

To relate this strain variable to the thermodynamic properties of a crystal, we must extend the notion of work due to applied stress beyond pressure-volume work relations. An applied stress σ

on a surface element dS of a crystal results in a force

$$f_i = \sum_j \sigma_{ij} dS_j. \tag{2.7}$$

In direct analogy to the relation $dW = PdV$ for isotropic pressures, the work done by the crystal against this stress can be written as

$$dW = -V \sum_{ij} \sigma_{ij} d\eta_{ij}. \tag{2.8}$$

From here, thermodynamic state functions can be expressed as functions of configuration

$$dU = TdS + V \sum_{ij} \sigma_{ij} d\eta_{ij}. \tag{2.9}$$

Since the Helmholtz free energy (F) is related to the system energy by $F = U - TS$:

$$dF = -SdT + V \sum_{ij} \sigma_{ij} d\eta_{ij}. \tag{2.10}$$

In order to ensure applicability to experimental conditions in which the number of particles and temperature are constant, we will work with the Helmholtz free energy and quantities derived from there. Similar quantities applicable to other ensembles can be found in a similar way. Because we have already developed a strain variable that is rotationally invariant, we can describe the free energy as a function of that variable and configuration:

$$F(\mathbf{x}, T) = F(\mathbf{X}, \eta_{ij}, T). \tag{2.11}$$

The compressibility derived for isotropic systems, $k_T = -V^{-1} \left(\partial V / \partial P \right)_T$, is replaced with the elastic constants. They can be found to arbitrary order:

$$C_{ijkl}^T = V^{-1} \left(\partial^2 F / \partial \eta_{ij} \partial \eta_{kl} \right)_{T\eta'}, \tag{2.12}$$

$$C^T_{ijklmn} = V^{-1} \left(\partial^3 F / \partial\eta_{ij} \partial\eta_{kl} \partial\eta_{mn} \right)_{T\eta'}, \tag{2.13}$$

$$C^T_{ijklmnpq} = V^{-1} \left(\partial^4 F / \partial\eta_{ij} \partial\eta_{kl} \partial\eta_{mn} \eta_{pq} \right)_{T\eta'}. \tag{2.14}$$

Here, η' indicates that all other η_{ij} are held constant during differentiation. Using these constants, state functions can be expanded in powers of η:

$$F(\mathbf{x}, \eta_{ij}, T) = F(\mathbf{X}, T) + V \sum_{ij} \sigma_{ij}\eta_{ij} + \frac{1}{2} V \sum_{ijkl} C^T_{ijkl}\eta_{ij}\eta_{kl} + \ldots \tag{2.15}$$

We can see that the terms of second order and higher represent the free energy cost of deformation of the anisotropic system. The error present in this series is controllable by the choice of series truncation. For our discussions of linear elasticity, we will consider only the second order term. This is the same as describing all restoring forces in the material as linear in displacement. Under this approximation, the strain energy of a system is written as

$$E = \frac{1}{2} \sum_{ijkl} C_{ijkl}\eta_{ij}\eta_{kl}. \tag{2.16}$$

Here, the superscript on C_{ijkl} has been dropped because it is assumed that we are in an isothermal system. Changes in the strain energy of a system will be our main tool by which the interaction of strain-producing objects (such as active particles and defects) can be estimated, provided the strains are within the range well described by the second order C. Furthermore, strain states are assumed to be linearly additive.

Equation 2.15 also shows how the Helmholtz free energy of an elastic solid is related to the Gibbs free energy. The relation $G = U - TS - PV$ can be recast as

$$G = U - TS - V \sum_{ij} \sigma_{ij}\eta_{ij} \tag{2.17}$$

The term that must be subtracted is simply the first order term in eq. 2.15. With this conversion the

free energy of solids under constant temperature and pressure can be expressed as

$$G(\mathbf{x}, \eta_{ij}, T, \sigma_{ij}) = F(\mathbf{X}, T) + \frac{1}{2}V \sum_{ijkl} C_{ijkl}^{T} \eta_{ij} \eta_{kl} + \dots \tag{2.18}$$

2.3 Calculation of Elastic Moduli

To assign a free energy cost to the strains measured for a system we must know the elastic modulus of our solid. The method I employ for computing this modulus is known as the fluctuation method [86]. This method relies upon thermal agitation in the system to sample strain space. If the periodic simulation box is given full degrees of freedom during the simulation, then the distortions of the box from its ensemble average shape can be interpreted as system strains. Therefore, in this method the box distortions are recorded over the course of one simulation, and all modulus components are solved for via a system of equations.

Parrinello and Rahman first proposed the (PR) fluctuation method for the isothermal constant stress ensemble ($N\sigma T$) [86]. In the PR formulation, only the fluctuations of system strain are used to calculate the elastic modulus tensor. Ultimately, the equation

$$C_{ijkl} = \frac{k_B T}{\langle V \rangle} \langle \eta_{ij} \eta_{kl} \rangle^{-1} \tag{2.19}$$

is solved, which is a straightforward application of energy equipartition; on average, the free energy stored in strain fluctuations must be consistent with the temperature of the system. The angle brackets represent ensemble averages, k_B is the Boltzmann constant, and $\langle V \rangle$ is the average system volume. The strain of the system is found from the box scaling matrix h:

$$\eta_{ij} = \frac{1}{2} \left(h_{nl} \langle h \rangle_{lj}^{-1} h_{np} \langle h \rangle_{pi}^{-1} - \delta_{ij} \right). \tag{2.20}$$

Here the ensemble average scaling matrix $\langle h \rangle$ defines a neutral, unstrained reference state and δ_{ij} is the Kronecker delta tensor. In practice, the inversion required can be carried out by switching to

the Voigt representation [87] of the matrix (6×6). Despite the simplicity of its formulation and the convenience of not needing to know anything about the interaction pair potentials of particles in the system, this fluctuation method is of limited use because it suffers from very poor convergence [88].

Using newer formulations of the method that incorporate stress fluctuations [88], quick convergence can be obtained in a single simulation run to completely characterize the elastic modulus. For a description of the stress-strain fluctuation method, see AppendixA.

2.4   Local Strains

In section 2.2, the strain was interpreted as a linear transform to all points within the entire system. This need not be the case. All stress and strain variables can be expressed as tensor fields, describing local linear transformations. Defects (such as dislocations) can then be described by the characteristic strain field that they produce. Generally, defects have a short range length scale (the 'core' of the defect) for which the small strain assumption of linear elastic theory broken, and a longer range length under which they can be approximated as a linear strain field. Because the region of small strain is long-ranged, it typically contains more free energy than the core, despite the high free energy density of the highly distorted core region.

Ultimately, the local strain concept views a system as a collection of sub-domains with homogeneous (constant) strains within them. Each sub domain then obeys the expressions derived in section 2.2. There is the additional consideration of what happens at the interface of two sub-domains with different strain states. When considering a domain without internal voids or free surfaces, the tensor field that describes the location dependent strain must obey compatibility relations. For a continuum material at rest, this relation states that $\eta_{ij} = \frac{1}{2} \left(\frac{\partial u_i}{\partial x_j} + \frac{\partial u_j}{\partial x_i} \right)$ (where $\vec{u}$ is the displacement vector and $\vec{x}$ is the position vector). Stated another way, this condition requires that the strains be obtainable from integration of the displacements. In this context, displacements are vectors describing how far a reference point has moved during a deformation.

These properties of strain fields can be exploited to allow us to numerically predict a strain

field resulting from a prescribed space-varying deformation. Consider the case of an inclusion embedded within a material. If the inclusion and the material have different thermal expansion properties, then a change in temperature will produce a strain at the inclusion's edge. The strain field produced by this expansion need not be associated with a corresponding stress field, and therefore it need not obey compatibility. However, the strain will induce a stress and strain state in both the material and inclusion. The superposition of the 'non-elastic' expansion strain, and the elastic strain must be compatible (if no voids are formed). While thermal expansion mismatch is a classic example, this general concept can be applied to any situation where we want to find the total strain resulting from a 'non-elastic' strain.

Analytic solutions for particular geometries of non-elastic strain fields derived in the literature follow the general approach of a Green's function method, analogous to the same method as employed in studies of electrostatics [89]. Green's functions have been obtained explicitly only for isotropic and transversely isotropic solids. For general anisotropic solids under arbitrary non-elastic strains, the best solution for finding elastic strains is the *method of eigenstrains*, developed by Mura [90]. For an outline of the mathematics of this method, as well as a code snippet for calculating strains from eigenstrains, see Appendix B.

If we break a large crystal down into sub-domains that have their own strain state, the smallest meaningful distance to consider is the distance between nearest neighbors. Indeed, it is possible to use the positions of neighbors around each particle in a simulation to define a set of vectors and compute its state of linear transformation. For a more detailed discussion of how to compute the strain state of a collection of neighbor reference points, see Appendix C.

CHAPTER 3

Strain Fields in Repulsive Colloidal Crystals

This chapter and its figures are adapted from Ref [79], a publication in *Physical Review Materials* authored in 2018 by Bryan VanSaders, Julia Dshemuchadse, and Sharon C. Glotzer.

3.1 Colloidal Crystals with Designed Material Properties

Our ability to synthesize nanoparticles with desired shape or surface functionalization continues to improve [2, 91, 92], and research on colloidal crystals has largely focused on finding connections between interaction potentials and assembled crystal structures [8, 22, 24, 93, 12, 94, 91, 95]. As colloidal research continues to develop, it is expected that desired material properties beyond crystal structure will become targets of investigation for colloidal engineering [96]. One such property of interest is the mechanical response of colloidal materials. Metallurgists have accumulated a wealth of knowledge and models to describe, predict, and explain the various ways in which bulk properties and defects contribute to the mechanical behavior of a material. A central concept is the linear elastic strain field, which has been used to understand dislocation interaction energies, enabling the creation of high-strength metals.

The time is now ripe to investigate how such concepts can be applied in colloidal matter. There are two compelling reasons to do so. The first is to inform the use of colloidal crystals as analogues of atomic crystals. Given the large size and long time scales of colloidal particles, it is possible to directly observe processes that range from challenging to impossible to observe with

atoms. Therefore it is attractive to re-create the circumstances that surround a hidden atomic process in a colloidal crystal and observe the system's evolution. Some pioneering work has already been done along this line. Schall et al. [69] devised an interferometry method for viewing dislocations in hard-sphere colloidal crystals. Later, the same authors employed this technique to observe the formation of dislocation loops in colloidal crystals following indentation by sewing needles [70]. More recently, Lin et al. [71] reported a method for directly measuring local stress fields around dislocations and other defects within colloidal crystals using confocal microscopy. Van der Meer et al. [97] investigated the strain fields that surround point defects in simulated hard-sphere crystals and used them to explain interstitial clustering behavior. While these works are foundational for establishing the connection between colloidal and atomic material defect dynamics, many unanswered questions remain. Importantly, it is not yet clear which atomic phenomena can be meaningfully studied via colloidal analogues. By investigating the use of core metallurgical concepts such as linear elastic strain fields in colloids, we aim to further inform the use of these model systems.

The second motivation for our study is to explore what is possible *beyond* phenomena seen in atomic materials. Colloidal crystals are famous for their exotic optical properties [98, 99, 100, 101]. The creation of metamaterials with exotic mechanical properties requires greater understanding of the mechanical behavior of colloidal assemblies, which is currently lacking [102, 103, 104, 105]. Beyond the realization of unusual material properties, there is also compelling evidence that metallurgical concepts are important throughout the assembly processes. For example, it has been shown that local material strain plays an important role in the evolution of self-limiting assemblies [106]. A more complete understanding of the nature of strain fields in colloidal materials enables greater sophistication both in the search for exotic material properties and the exploitation of geometric constraints for assembly engineering [72, 107, 108, 109].

In this study we focus on a family of isotropic pair potentials (see Fig. 3.1) that smoothly range from the canonical Lennard-Jones (LJ) potential used to model atomic systems [110]:

$$V_{\mathrm{LJ}}(r) = \quad 4\varepsilon\left[\left(\tfrac{\sigma}{r}\right)^{12} - \left(\tfrac{\sigma}{r}\right)^{6}\right] \qquad r < r_{\mathrm{cut}} \tag{3.1}$$

$$= \qquad\qquad 0 \qquad\qquad r \geq r_{\mathrm{cut}}$$

to a hard-sphere potential used to model excluded volume interactions in colloids. This is done with the Shifted Weeks-Chandler-Andersen (SWCA) [111] potential:

$$V_{\mathrm{SWCA}}(r) = \quad 4\varepsilon\left[\left(\tfrac{\sigma}{r-\Delta}\right)^{12} - \left(\tfrac{\sigma}{r-\Delta}\right)^{6}\right] + \varepsilon \qquad r < (r_{\mathrm{cut}} + \Delta) \tag{3.2}$$

$$= \qquad\qquad 0 \qquad\qquad r \geq (r_{\mathrm{cut}} + \Delta).$$

Δ is the average of particle diameters between which the potential is calculated. $\varepsilon = 1$ for all potentials used in this study. The pair potential parameter h is used to indicate potential 'hardness'. The value of σ used in the SWCA potential is related to h as $\sigma = 1 - h$. The radial shifting of the SWCA potential is then chosen so potentials of different hardness value are zero at the same distance between particle centers (as shown in Fig. 3.1). As $h \to 1$, $\sigma \to 0$ and the potential approaches a step function. By parameterizing our potential space in this way, we can interpolate between a broad range of soft to hard repulsive interactions. The key difference is the length scale over which the potential varies. In atomic systems, the sharpness of potentials is fundamentally limited by natural constants and the behavior of electrons. In colloidal systems, the pair potential values can change rapidly over distances much smaller than the particle separation distances (such as in hard-sphere systems, for instance). We examine the extent to which these materials obey the linear elastic approximation by computing the strain fields around edge dislocations and the stress-strain relationships for homogeneous uniaxial strains.
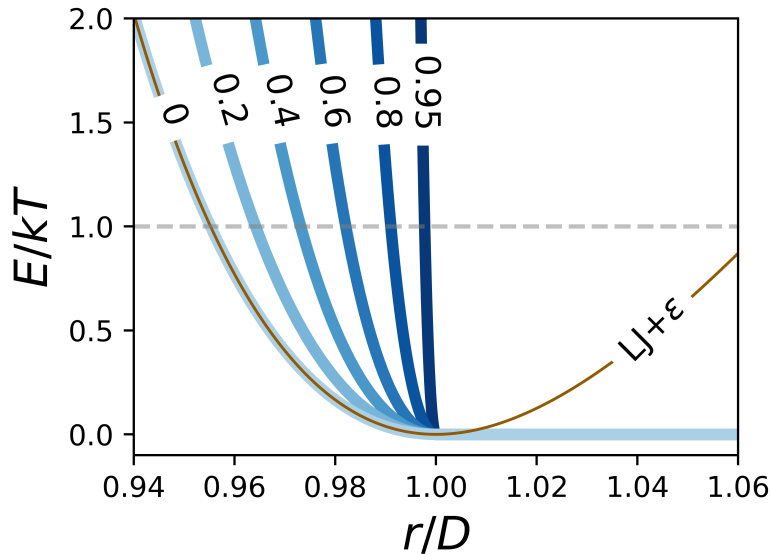
Figure 3.1: The isotropic pair potentials used in this study, shown in units of system thermal energy. Darker blue curves are potentials with larger hardness values (labeled on curves). The Lennard-Jones potential (shifted in energy by ϵ) is also shown for comparison.

3.2 Study Methods

3.2.1 Molecular Dynamics

All molecular dynamic (MD) simulations reported here are performed with `HOOMD-blue` [112, 113]. Particles are simulated in a periodic box with Cartesian directions x, y, z aligned to crystal directions $[1\bar{1}0]$, $[11\bar{2}]$, $[111]$ in the face-centered cubic (FCC) structure. Simulations are carried out in the NPT ensemble via equations derived by Martyna et al. [84]. System thermal energy is held at $kT = 0.1$ and particle mass is fixed at $m = 10$ (in simulation units). This thermal energy is chosen so that the LJ system at zero pressure forms a solid. If simulation units are chosen to correspond to a system of silica particles of diameter 1.12 μm and bulk silica density (2650 kg/m^3) evolving at room temperature (291.8 K), then the depth of the LJ attractive well corresponds to a binding energy equal to three times that required to lift such a particle by its own diameter while immersed in water (at sea level).

26

3.2.2 Strain Fields of Dislocations in Continuum Materials

The analytical form of the strain distribution surrounding a periodic dislocation array can be most easily found with the method of eigenstrains derived by Mura [90]. In that approach, the distortions from the defect are introduced as singularities and regularized by the application of a function constructed from the elastic modulus tensor of the material in the Fourier domain. The result is a continuous periodic strain distribution.

Strain distributions for edge dislocations are calculated from the eigenstrain procedure by introducing a region of η_{xx} strain bounded by a bi-variate Gaussian in the x and z directions and constant in the y direction (along the dislocation line). The center of the eigenstrain region contains a discontinuity, which defines the location of the dislocation core. This procedure is an adaptation of methods used by Chiu [114] and Daw [115].

3.2.3 Elastic Moduli Sampling

The eigenstrain calculation has only a single material-dependent input, the elastic modulus tensor. We sample the elastic modulus tensor from MD simulations following the method of Gusev et al. [88]: moduli are calculated from the fluctuations of virial stress and box strain for an MD simulation which permits the box geometry to change ($N\sigma T$ ensemble).

As shown by Tretiakov et al. [116], the calculated value of the elastic modulus of a LJ crystal depends upon the value of the r_{cut}, even when the r_{cut} is large. A well-defined system is the nearest-neighbor LJ (nnLJ) potential, in which the LJ interaction is calculated only for a particle's nearest neighbors. For homogeneous systems, this can be approximated with a fixed cutoff value r_{cut} between the radius of the first and second nearest neighbor shells. Discontinuities in the pair potential are created, but never crossed by particles in a dense crystalline system. However, in defective crystals (such as those involving dislocations), particles will cross these discontinuities. To avoid such discontinuities, we do not use the nnLJ potential and instead employ a constant $r_{\text{cut}} = 3\sigma \cdot 2^{1/6}$. At this range, the potential value is $\leq 0.3\%$ of the attractive well depth. The potential is shifted and a smoothing function applied so potential energy and force are zero at

$r = r_{cut}$.

A σ value of 1 is used for the LJ potential. SWCA shifting parameters (σ and Δ) are chosen so that all potentials are zero at $D = 2^{\frac{1}{6}}$.

3.2.4   Strain Field Sampling

The strain fields surrounding dislocations were sampled by histogramming per-particle strain matrices. Per-particle strain was calculated using the analysis software `OVITO` [117]. To map the per-particle data onto the output of the eigenstrain calculation, the individual strain tensors were assigned to spatial bins and averaged over time. The number of bins was chosen to be similar to the number of particles, as this yielded the highest-resolution voxelized strain field data. The mean and standard deviation of the mean for per-particle strain fields were calculated with bootstrapping [118].

3.3   Elastic Property Matching via Pressure

To compare repulsive and attractive potentials meaningfully, a pressure (or density) must be chosen for the repulsive systems. Simply selecting identical densities for attractive and repulsive interaction potentials is not sufficient to ensure similar mechanical properties. Instead, we outline a deformation free energy matching procedure which results in material systems with similar elastic properties. The Lennard-Jones (LJ) solid at zero pressure was chosen as the reference against which to match the elastic properties of the repulsive systems. To agnostically compare materials formed by different potentials the sum of homogeneous deformation strain free energy under a collection of modes was calculated. The matching pressure is defined here as the pressure which satisfies the equation:

$$min \left[\sum_m \left| \sum_{ijkl} C_{ijkl}^{(\text{LJ},P=0)} \eta_{ij}^m \eta_{kl}^m - \sum_{ijkl} C_{ijkl}^{(\text{SWCA},P=P_{match})} \eta_{ij}^m \eta_{kl}^m \right| \right]_{P_{match}} . \tag{3.3}$$

Here, C_{ijkl} is the second-order elastic modulus tensor and η_{ij}^m is a homogeneous strain. Note that the first term in Eq. 3.3 is the deformation free energy density of a material under no external stresses (LJ crystal), while the second term is the deformation free energy density of a material under the external hydrostatic pressure P_{match} (SWCA crystal). The η_{ij}^m (strain modes) over which to sum deformation free energy differences could be chosen to emphasize a particular kind of deformation. As an example, if the target of matching was to produce two materials with similar behavior under uniaxial loading, then a single strain mode corresponding to that loading could be used in Eq. 3.3. Since here we are concerned with a general measure of the mechanical similarity of two materials, we use an even weighting of all non-zero strains. Using the six independent components of the linear strain tensor η_{ij} and combining them with equal weight, 64 permutations are possible, with one permutation being the trivial zero strain case.

The result of this property-matching search is shown in Fig. 3.2. It is clear that the mechanical properties of softer potentials can be better matched to the LJ solid by varying the pressure, however it is possible to match with less than 10% deformation free energy variation for all pair potential hardness values studied. We observed that the pressure window of optimal matching shrinks as the pair potential hardness increases. All subsequent simulations of repulsive potentials, unless otherwise stated, are conducted under the appropriate P_{match} shown in Fig. 3.2.

3.4 Deformation Entropy for Property-Matched Crystals

As the hardness of the SWCA potential is increased, the behavior of the system more closely approaches that of hard spheres. For a material of hard spheres, system configurations with particle overlaps are impossible, as these have infinite internal energy. All other configurations have zero internal energy. Therefore these materials are 'entropic' solids, with no enthalpy changes upon crystallization. It follows that the mechanical properties of solids studied here must also become increasingly dominated by entropy effects as h approaches 1. Fig. 3.3 demonstrates this point explicitly: as pair potential hardness is increased, the internal energy of deformation decreases in
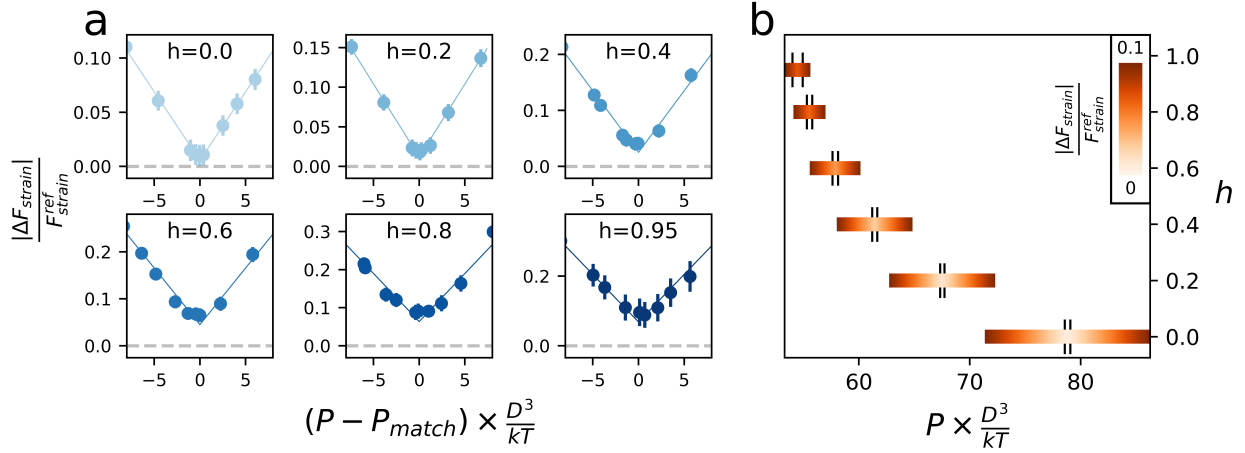
Figure 3.2: Pressures at which the moduli of SWCA systems most closely approach those of an LJ system at zero pressure. **(a)** Plots of the absolute value of the fractional difference in strain free energy between the SWCA and LJ system. Here F_{strain}^{ref} is the strain free energy of the LJ system against which the matching is being evaluated. Error bars are calculated via bootstrapping of moduli measurements, and represent one standard deviation. **(b)** Absolute pressure versus hardness. Tick marks indicate the uncertainty of P_{match}, one standard deviation of the minima from the fit in (a), and the color map is the fit value from (a), truncated at 10% maximum difference.

magnitude, indicating that entropic changes contribute more to the free energy of deformation (and the elastic modulus) than energetic interactions between particles. As hardness is increased, the contribution of potential energy to the free energy of deformation becomes negligible. This demonstrates that the h parameterization is useful for studying the transition from energetic deformation to entropic deformation.

3.5 Statistics of Strain Fields in Entropic Solids

Working with entropic materials presents a complication for analyzing strain fields: fluctuations in particle position are so large that accurate strain fields cannot be calculated from a single snapshot of a particle's local neighborhood. In materials with energetically dominated free energies of deformation, temperature can be lowered to improve the accuracy of strain fields sampled from a single snapshot. This is not possible for materials with significant deformation entropy. Therefore the strain fields must be calculated from averages of particle positions.
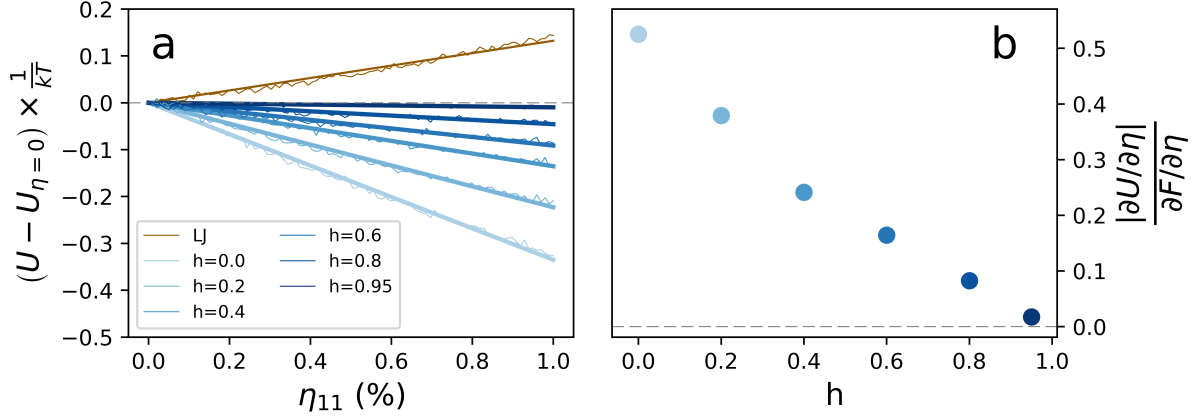
Figure 3.3: Energy and entropy of deformation. **(a)** Internal (potential and kinetic) energy of deformation of potentials in this hardness family. Solid lines are linear fits to data collected from systems homogeneously deformed along the $[1\bar{1}0]$ direction. **(b)** Ratio of internal energy change to free energy change (evaluated at 1% strain). Free energy is calculated from the sampled elastic moduli and the applied homogeneous strain. Error bars of one standard deviation are much smaller than shown data points.

To understand how the accuracy of strain field sampling changes as snapshots are collected, the per-particle strain of defect-free simulation domains were calculated with methods implemented in the visualization and analysis tool `OVITO` [117, 119]. Samples were collected with adequate time lag to assure decorrelation. The behavior of the standard deviation of averaged measurements with the number of samples is shown in Fig. 3.4. Harder potentials converge with fewer decorrelated samples. This is a consequence of collision behavior for different hardness potentials. For soft potentials, velocities slow gradually as particles overlap and are eventually accelerated apart. A hard particle ($h = 1$) has instantaneous collisions. Since collisions occur far from the average position of a particle at its lattice site, slow collisions spread the particle's probability distribution function farther from the average, i.e. increasing positional variance. Hard particles with fast collisions spend less time far from their lattice sites. Consequently, variables that are functions of particle position (such as strain) converge faster for harder particles.
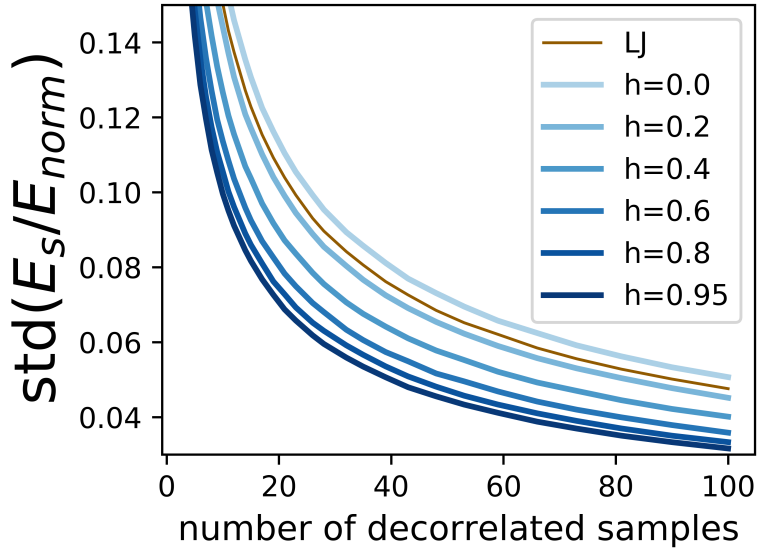
Figure 3.4: The standard deviation of per-particle strain energy values (normalized to a reference strain) as a function of the number of decorrelated samples considered. For each sample number, bootstrapping is used to obtain the standard deviation. The normalization strain is chosen to be the per-particle strain energy of a 1% volumetric expansion in LJ, which estimates the strain energy of a dilatory point defect such as a vacancy. With increasing h, fewer samples are required to obtain the same standard deviation values.

3.6 Strain Fields Around Edge Dislocations

The strain fields around dislocations arrays were collected for different hardness potentials simulated under the P_{match} pressures shown in Fig. 3.2. Dislocations arrays were created by subtraction of a half plane of particles in a simulation box spanning 60 unit cell lengths in the x direction (aligned with crystal direction $[1\bar{1}0]$), 24 unit cell lengths in the y direction (aligned with crystal direction $[11\bar{2}]$), and 20 unit cell lengths in the z direction (aligned with crystal direction $[111]$). Box boundary conditions are all periodic, and the final particle count was 346,992 for all cases. All systems studied here readily dissociate into partial dislocations. The per-particle strain fields, produced from 100 decorrelated samples, are shown in Fig. 3.5 (η_{xx}, η_{zz} and η_{xz}, the largest magnitude strain components) and Fig. 3.6 (the remaining, small magnitude components). In the analytic solution for the strain field of a straight dislocation the strain components which include the dislocation line direction (y) have very small values because of the symmetry along the dislocation line

direction. In the sampled distributions there are additional contributions from the bends and kinks, which occur in a thermalized dislocation. As these are averaged strain field values, a distribution of dislocation line conformations contribute to these fields.

Only one pair of partials is shown, the full simulation domain contains four partial dislocations. For comparison, analytic strain distributions calculated with the method of eigenstrains [90] are shown for the LJ solid and the hardest potential, $h = 0.95$. Sampled dislocation strain fields closely follow those predicted by linear elasticity for LJ and $h = 0$ systems. As h approaches 1, greater asymmetry appears in the sampled distributions (Fig. 3.9).

The geometry of the dislocation array changes as potential hardness is increased, with the separation between partials shrinking. This separation is typically a function of elastic interaction free energies between partial dislocations (favoring repulsion) and a free-energy penalty for stacking fault creation (favoring closely bound dislocations). Pronk et al. calculated the stacking fault free energy for hard spheres, and found it to be very small [120]. This logically follows from analytic calculations of stacking fault energy [67], in which only second-nearest neighbor interactions and farther contribute. For short-range potentials, second and farther neighbor interactions are very weak, and should reduce further as the hard sphere limit is approached. This means that the trend in partial separation distance shown here is opposite of what would be expected if stacking fault free energies were the primary driving force.

Instead of stacking fault creation energy, the driving force for dislocation array geometry change is the way in which different components of the elastic modulus tensor change with potential hardness. Fig. 3.7 shows the cubic symmetry elastic modulus constants for SWCA potentials of different hardness (under appropriate P_{match}), normalized by the zero-pressure LJ solid. The deformation free energy matching minimization used to find P_{match} does not enforce a relationship between individual components of elastic constants, but rather the sum of all deformation free energies. As the potentials become harder, the relative strength of uniaxial terms ($C_{ii,i<4}$) remains constant, while shear ($C_{ii,i>3}$) and uniaxial coupling ($C_{ij,i\neq j}$) change in a complimentary way. Because uniaxial and shear lobes have different geometries, changing the relative strengths of these
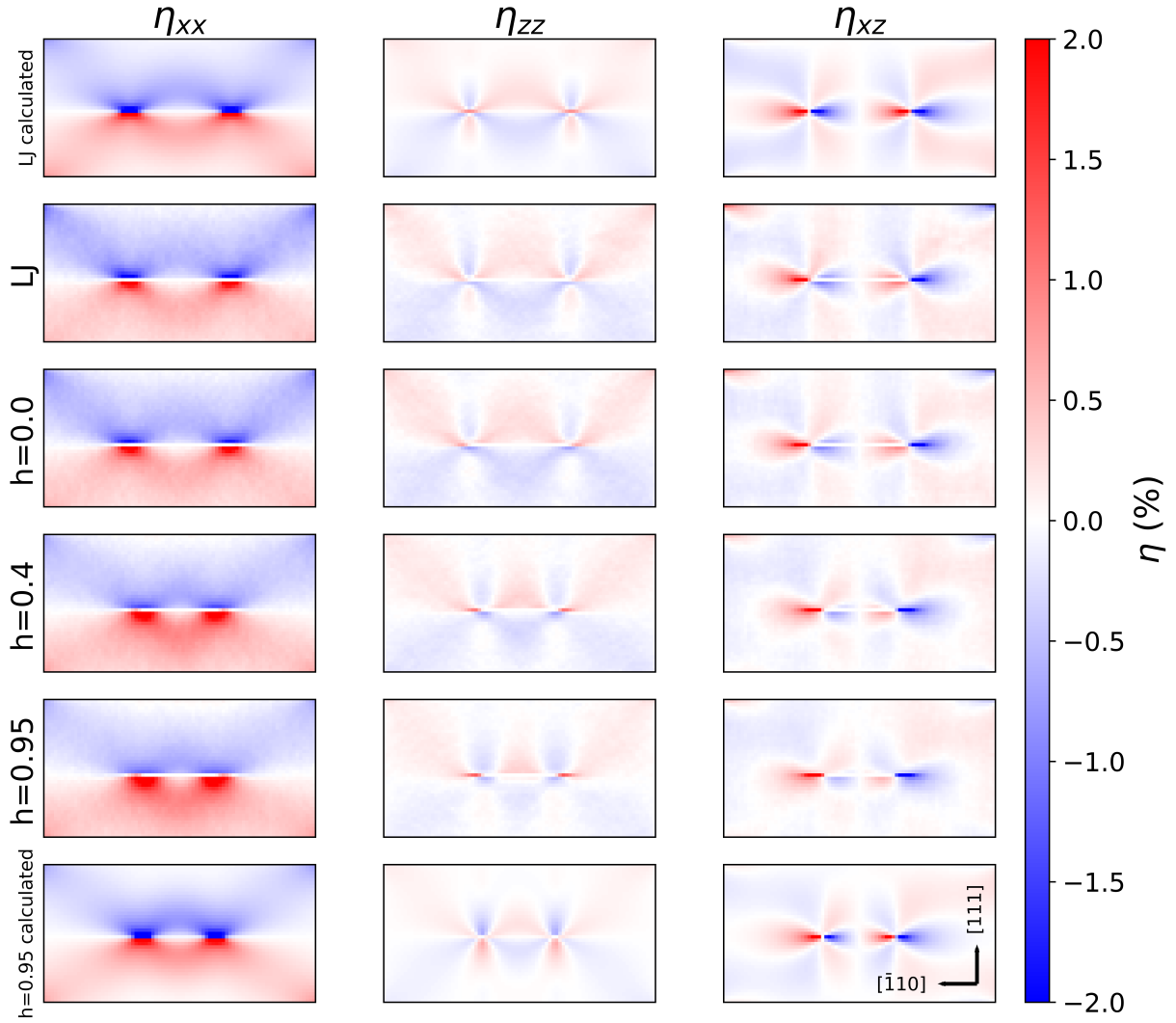
Figure 3.5: Strain fields around partial dislocation pairs. This view is along the length of the dislocation line, with the Burgers vector pointing from left to right in the plane of the image. The three strain components with the largest magnitudes are shown. At low hardness, and in particular for LJ, we find a close match between the analytically generated strain distribution and the sampled one. As the hardness of the potential is increased, an asymmetry develops between the compressive and tensile regions of η_{xx} and η_{zz}.
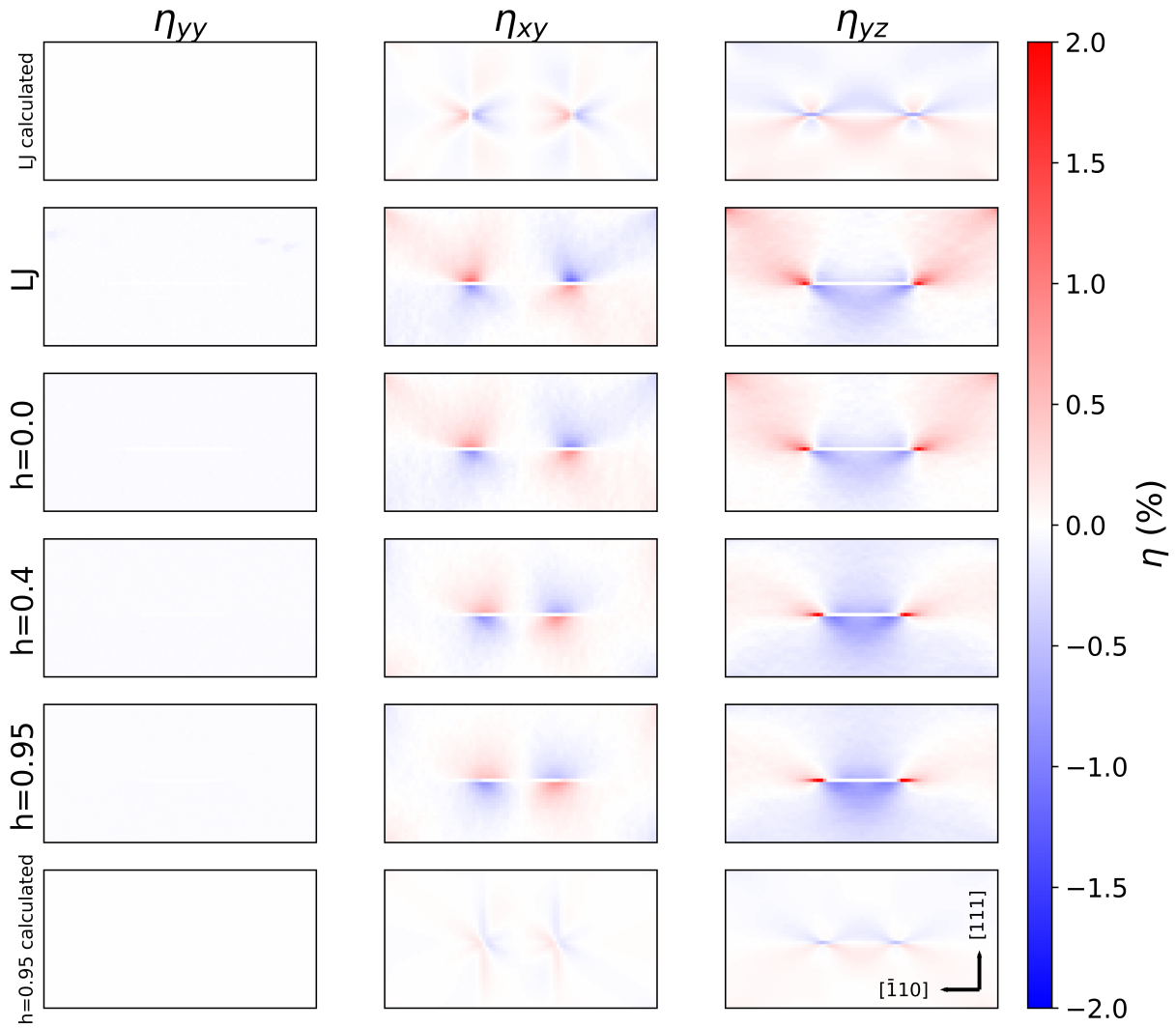
Figure 3.6: Strain field components which involve the y direction. Simulated dislocations contain kinks and bends, which produce average values of η_{yy}, η_{xy}, and η_{yz} that are larger and differently distributed than the perfectly straight calculated dislocations.

interactions causes a change in the dislocation array geometry.
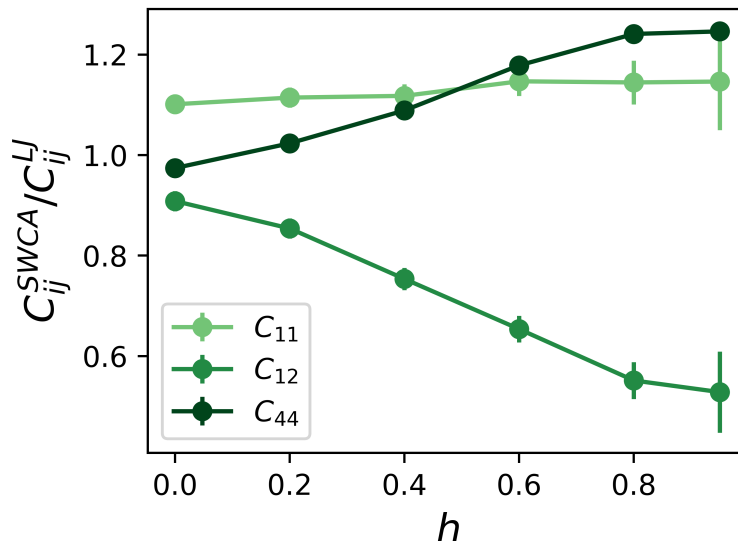
Figure 3.7: Cubic symmetry elastic modulus constants, relative to the zero-pressure LJ solid, for SWCA potentials at different hardness values (sampled under appropriate P_{match}). Uniaxial terms (C_{11}) are relatively stable as hardness is increased, while shear terms (C_{44}) and uniaxial coupling terms (C_{12}) change in a complimentary way. Error estimates were generated with a bootstrapping procedure.

To explore the origins of strain asymmetry in the dislocation cores, we simulated defect-free systems and imposed a homogeneous uniaxial strain in the x direction. Fig. 3.8 shows the difference in stress-strain relation for the application of a compressive or tensile strain. This result explains the asymmetry in the strain field surrounding dislocation cores. The system can be said to be elastically linear when the stress depends linearly on strain and strain energy is symmetric for positive and negative strains. From this plot, we can see that systems with higher h have a more limited range of strains where these two conditions are true. The LJ solid is the most symmetric, however the inherent asymmetry of the bonding well for this potential produces a difference for tension and compression at large strains (compression into the repulsive particle core increases system energy more than tension). The pure repulsive solids all display greater stress-strain asymmetry than the LJ solid. Furthermore, as h approaches 1, the linear strain region shrinks.

These factors together explain the strain field asymmetry of dislocations in hard-potential col-
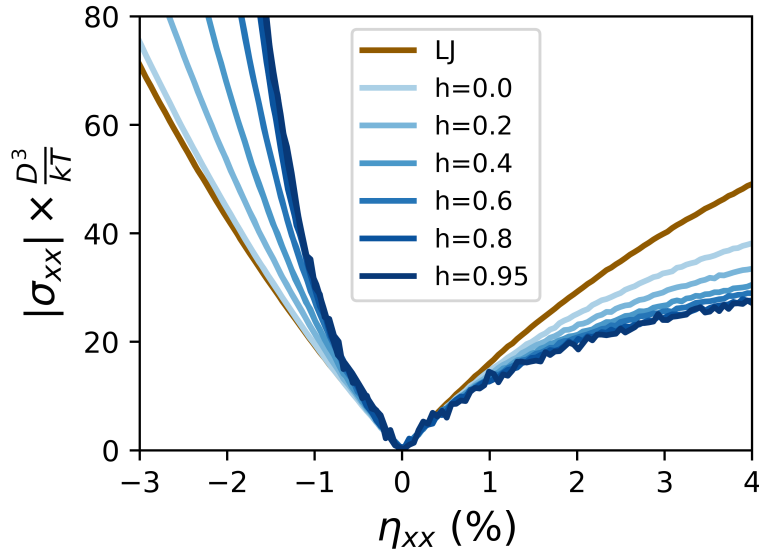
Figure 3.8: Stress-strain relationship for different values of h under a strain ramp. The region of linear behavior shrinks and the asymmetry of the stress curve increases as the pair potential hardness is increased. All potentials are first equilibrated under appropriate P_{match} and then a uniaxial strain is applied.

loidal crystals. The number density of dislocation lines remains the same for all systems studied here. As the linear strain limit reduces with increasing h, the field close to the dislocation core begins to exceed these limits; at this point it is energetically much less costly to increase the tensile strain than the compressive strain. As h approaches 1, the size of the region near the core that experiences nonlinear strain increases. Fig. 3.9 shows the strain asymmetry of sampled strain fields near dislocation cores. To better highlight asymmetry, value of the η_{xx} component is shown, mirrored across the glide plane, differenced, and the absolute value taken. As hardness is increased, the region of significant strain asymmetry around the dislocation core grows. The onset of this asymmetry marks locations where the second order linear elastic approximation is no longer applicable, and so is a potential definition of core radius. This core region increases in size as the hardness of the potential is increased.

Interestingly, conventional definitions of core size, such as the distance from the core at which the shear stress is equal to the theoretical shear stress of the material [121], show the opposite trend when applied to these systems (i.e. decreasing core size with increasing pair potential hardness,
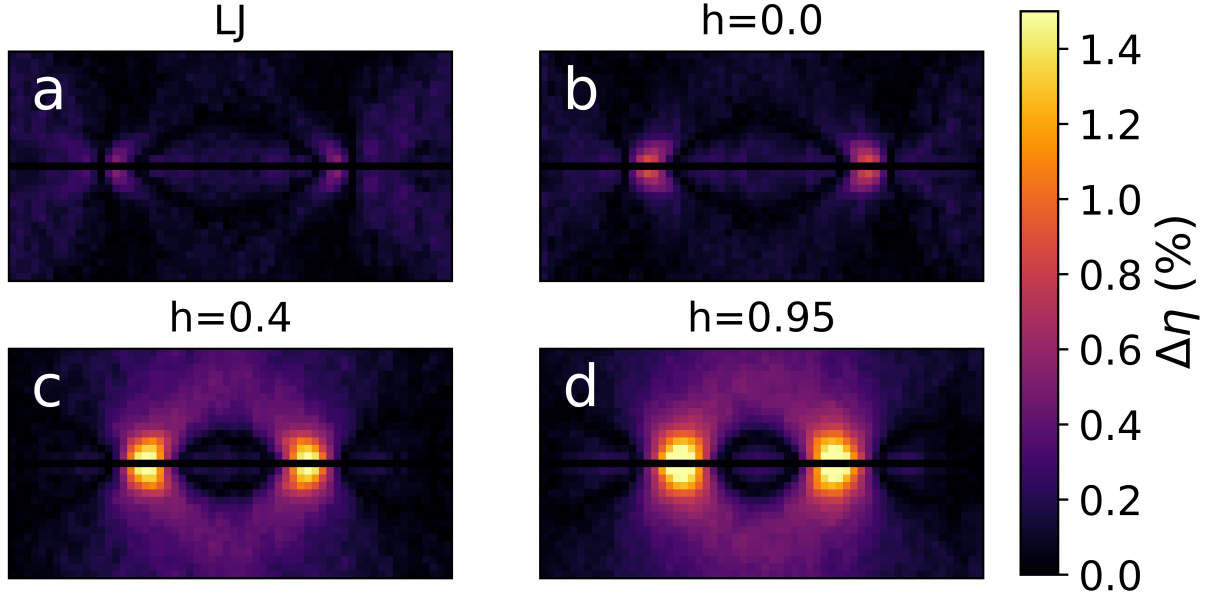
Figure 3.9: η_{xx} strain distributions mirrored across the glide plane (111), differenced, and the absolute value taken. As the hardness of the potential is increased, the symmetry of the distribution across the glide plane decreases.

Fig. 3.10). The radii of the core region for materials simulated in this study are estimated via the method used by Chrzan et al. [121], in which the edge of the core region is defined to be where the dislocation shear stresses are equal to the ideal shear strength of the material:

$$\frac{r_{core}}{b} = \frac{K}{2\pi G_{\{111\}}\gamma(1-\nu)},$$

(3.4)

where K is the elastic constant for the dislocation, $G_{\{111\}}\gamma$ is the ideal shear modulus, b is the Burgers vector, and ν is the Poisson's ratio. Expressions for K used in this study were those derived by Chou et al. [122] (not shown here due to length). The ideal shear strength was found using expressions derived by Roundy et al. [123]:

$$G_{\{111\}} = \frac{3C_{44}(C_{11} - C_{12})}{4C_{44} + C_{11} + C_{12}}$$

(3.5)

At pressures lower than the property matching pressure (P_{match}) found in Fig. 3.2, strain asymmetry is reduced. Fig. 3.11 shows the results of the same measurement as Fig. 3.8 for particles with
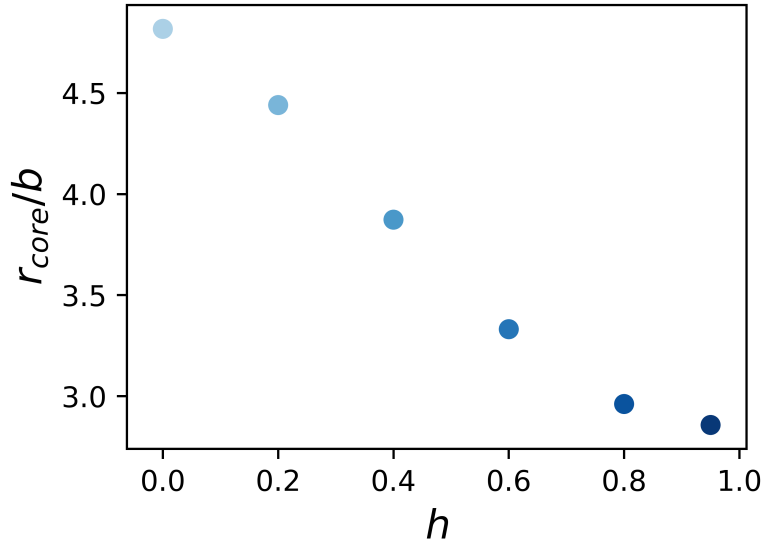
Figure 3.10: The radius of the dislocation core estimated from the colloidal crystal modulus. Error bars of one standard deviation are much smaller than data points. As potential hardness is increased, the core radius calculated by this measure decreases. This behavior is due to changes in the value of $C_{11} - C_{12}$ as potential hardness increases.

$h = 0.95$ at a range of pressures lower than P_{match}. As the pressure is lowered, the range of linear strain increases. Fig. 3.11b shows that nonlinear strain behavior begins to occur at values that correspond to a fraction of the inter-particle spacing. Entropic solids have inter-particle spacings significantly larger than the diameter of the particles. Hard particles explore a volume of crystal and interact with neighbors via collisions. When such ballistic motion is averaged over sufficiently long time scales, the effect is for a repulsive colloidal particle to behave as though bound to its lattice site through a harmonic potential (for small strains). Hence, linear elastic behavior is recovered from hard particle solids without any explicitly defined (energetic) binding wells. As pressure is reduced, the rattle volume of a hard particle at its lattice site increases. Local stress results in changes to the particle rattle volume, and Fig. 3.11 demonstrates that large rattle volumes tend to change more linearly with local stress changes.
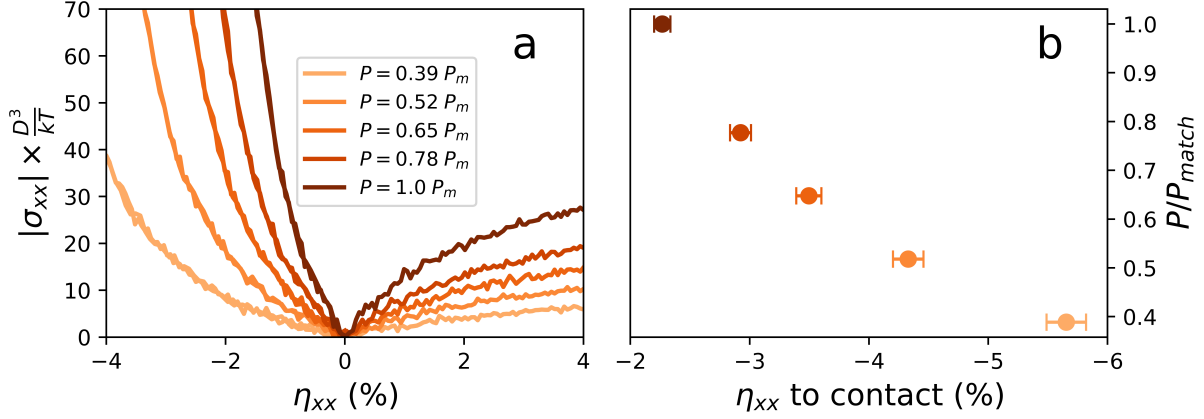
Figure 3.11: **(a)** Stress-strain curves for a system with $h = 0.95$, found by equilibrating the system under a hydrostatic pressure and then applying a uniaxial strain. As the pressure is reduced, the linearity of the stress-strain relationship improves. However, at pressures other than P_{match}, the solids cannot be said to have similar mechanical properties to the other systems shown in this study. **(b)** Strain to contact for systems in (a). Strain to contact is the strain needed geometrically to make particle centers sit a distance of r_{cut} from each other. Error bars represent one standard deviation (due to uncertainty in measurement of the lattice parameter). The region of linear behavior for a hard repulsive material must be a fraction of the strain-to-particle contact. Together this data shows that hard potentials behave most elastically linear when the rattle volume of a particle at its lattice site is large. The time averaged effect of many hard-particle collisions produces an effective harmonic potential.

3.7 Conclusions

We explored the linear elastic properties of a family of isotropic pair potentials. The parameterization variable for the hardness of the potential, h, was shown to correspond to an increasing importance of entropy in the deformation free energy of colloidal crystals. We demonstrated a method to define and search for state point conditions of maximum mechanical similarity between systems with different pair potentials. We showed that for this family of potentials the increased importance of entropy in deformation has several consequences for strain fields: 1) faster convergence (smaller variance) of strain field fluctuations, 2) higher stress-strain asymmetry, and consequently 3) larger nonlinear strain regions around dislocation cores. We also showed that the linear regime for these materials could be increased by lowering the pressure and thereby increasing the per-particle rattle volume. However, this changes the mechanical properties of the solid and so precludes matching

to a reference material.

Overall, the linear elastic approximation can be usefully employed in colloidal crystals, as long as care is taken to operate within the linearity limits for the state point in question. Applying linear elastic concepts to hard spheres at pressures significantly above the crystallization pressure will not yield good results, however at pressures near the melting point the mechanical behavior of hard spheres can be well approximated. The LJ solid at low temperatures and zero pressure is a well-behaved harmonic solid, and the method of eigenstrains can be used to accurately predict the form of strain fields surrounding complex defects such as dislocations. The WCA potential can be matched very closely in mechanical properties to the LJ solid by the application of pressure, and the so-obtained solid is likewise well approximated by linear elastic methods.

The equivalence of complex strain fields calculated with the method of eigenstrains and the sampled strain configurations inside simulated colloidal materials opens the door to using linear elastic methods to predict and design complex strain states within colloidal materials. Unlike in atomic materials, inclusions with designed shape can be easily introduced to colloidal crystals. Results shown here indicate that linear elastic strain methods can be used to understand emergent interaction between defects in colloidal crystals. So long the effects of pressure on the limits of the linear approximation is considered, the method of eigenstrains and other linear elastic methods can be powerful additions to the colloidal community's toolkit.

CHAPTER 4

Designing Active Particles for Colloidal Microstructure Manipulation via Strain Field Alchemy

This chapter and its figures are adapted from Ref [80], a publication in *Soft Matter* authored in 2019 by Bryan VanSaders and Sharon C. Glotzer.

4.1 Controlling Colloidal Crystal Microstructure

Rational design of colloidal crystals has focused primarily on crystal structure, with many excellent examples in the literature exploring the connection between particle interaction potentials (isotropic, anisotropic, DNA-based, hard shape, etc.) and equilibrium crystal structures [124, 125, 2, 91, 8, 93, 126, 12, 94, 127, 22, 95, 24, 23]. Far sparser are studies exploring the connection between these design parameters and material properties. The optical response of colloidal crystals [98, 99, 100, 101] has received the most attention, but mechanical and acoustical properties are also of interest [102, 103, 104, 105]. Rarer still are studies concerning the design of kinetically trapped defect states in colloidal materials. Such states are generally known as defect 'microstructure' in the metallurgical research community, and include phenomena such as dislocation networks and grain boundary interfaces. In metals, defect microstructure plays a critically important role in determining mechanical properties such as ultimate tensile strength and

creep [52]. Defect microstructure can also strongly influence other materials properties—such as conductivity—across orders of magnitude [128].

In photonic colloidal crystals, defects can create transmissive breaks in a photonic band-gap. These localized non-evanescent modes can be exploited to create device components such as wave guides and resonator cavities [55, 129, 130]. Connected regions of defects, such as those used in wave guides, can be thought of as a type of defect microstructure, with profound consequences for the optical band properties of the metamaterial. If the defects responsible for such properties could be reconfigured, then colloidal materials with tunable or dynamic properties are in principle possible.

Methods of microstructure control can be broadly grouped into two categories: microstructure formation during a phase transition, and microstructure formation without a phase transition. The first group encompasses many methods of control including Ostwald ripening [131], precipitation from solid solution [132], spinodal decomposition [133], and epitaxial growth [134]. Generally these methods employ a competition of mechanisms with different kinetics or enforced boundary conditions that modify the free-energy of a system to achieve the desired microstructure as the final solid phase is forming from the precursor phase (either fluid or a different solid). The second group of methods relies upon the application of non-thermal forces to drive microstructure evolution. Strain hardening in metals is a prototypical example of such a process [52], where forces are applied that drive microstructure evolution while the material is held at temperatures too low to permit escape from the metastable states formed. The use of high shear rates or high-energy bombardment with radiation has been explored to control microstructure in what are termed 'driven alloys' [135, 136, 137].

Despite the enormous wealth of materials science knowledge available (and numerous reports on colloidal defect behavior [138, 139, 140, 97, 69, 70, 141]), microstructure engineering in colloidal systems is only lightly explored. Van Blaaderen et al. [142] and more recently Dasgupta et al. [143] have explored the effect of surface templating on colloidal growth by sedimentation. By templating a surface with the periodicity of non-close-packed planes stacking faults can be sup-

pressed as the crystal grows. The impact of large impurities on 2D colloidal crystal growth has also been explored [140, 144]. Large impurity particles locally stabilize fluid-like configurations, and as a result are often incorporated into (and pin the motion of) grain boundaries during crystallization. These methods, where a defect microstructure is assembled from a fluid state, would fall under the first category of microstructure control.

Other work has exploited the large length scales of colloidal crystals to exert control over defects at the single particle level, falling within the second category of methods of microstructure control. The application of local forces on 2D crystals with optical traps has yielded demonstrations of direct control over individual dislocations and their reactions [73], the topology of grain boundaries [145], and the misorientation angle of a grain boundary loop [74]. Notable limitations of the optical force technique are the difficulty of applying it to 3D systems and the need to locate and image each defect to be manipulated. Besides optical forces, it has also been shown that local forces exerted by active particles can drive microstructure changes. Van der Meer et al. have shown for hard-sphere systems in two [75] and three dimensions [76] that the addition of active particles to systems with grain boundaries can result in accelerated kinetics of polycrystalline annealing, resulting in single crystals on short timescales.

Such active particles are but one example of a microscopic 'tool' – a specialized applicator of force designed to achieve target microstructures. In general, tools are specifically designed to enact certain transformations on their working material. Figure 4.1 schematically illustrates how control of dislocations permits control over the internal structure of a crystal through directed local plastic deformations. We explore how a 'tool-particle' can be designed for manipulation of defects (in this case dislocations) by changing its shape. Given that modern particle synthesis techniques are capable of producing a wide variety of shapes [146, 147, 148], we seek a general method of designing the shape of the particle-as-tool for maximum interaction with specific types of dislocations.

Our study uses the linear elastic formalism to understand the interaction between a self-propelled interstitial colloidal particle and dislocation microstructures in a crystal where spherical particles
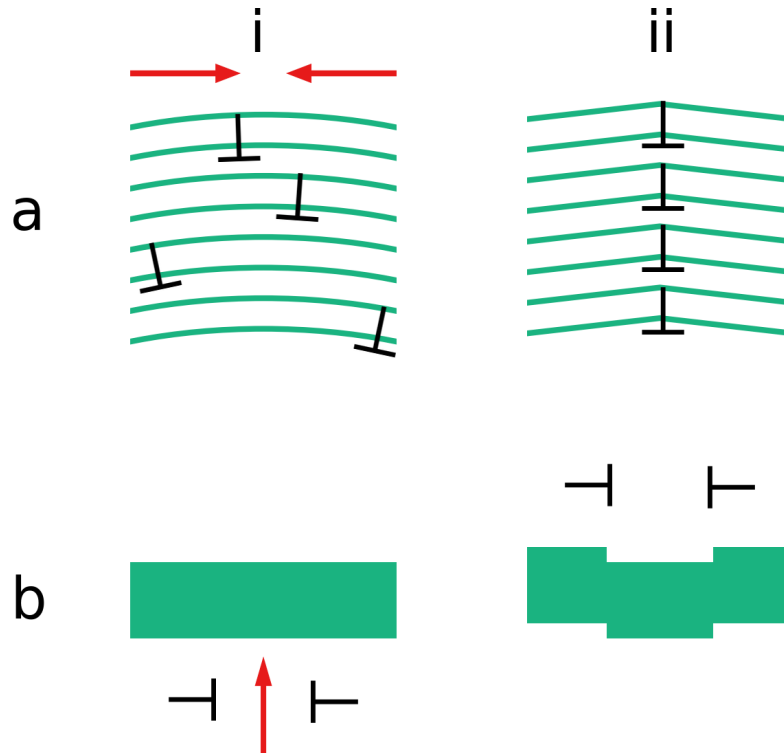
Figure 4.1: Examples of how direct control over dislocations can reconfigure crystalline materials. **ai-ii** Bending localization (or grain boundary formation) **ai** dislocations ($\perp$) are initially distributed randomly, resulting in low, evenly distributed curvature. Forces are applied to dislocations (red arrows). **aii** Dislocations are concentrated, resulting in high local curvature. **bi-ii** Coherent boundary roughening by passage of dislocation dipoles. **bi** Force (red arrow) is applied to a dislocation dipole to drive it towards a coherent grain (green). **bii** After passage through the coherent grain, the dipole has roughened the boundaries with a local shift of one Burgers vector.

interact via steeply repulsive isotropic potentials (i.e. nearly hard spheres). The interaction between interstitial and dislocation is estimated and designed by sampling the linear elastic strain fields of both objects. Our work seeks to provide a means to re-configure microstructure after crystallization has already occurred, which allows for the possibility of reconfigurable and responsive colloidal materials with functional defects.

In section 5.2 we describe the model system and methods employed in this study which are standard or introduced elsewhere. In later sections we apply these methods and introduce new methods created for this study to design interstitial tool particles capable of internally restructuring a colloidal crystal. This study utilizes several forms of simulation and characterization which feed

into the final result. Figure 4.2 shows a schematic view of the flow of information and use of different simulation methods.
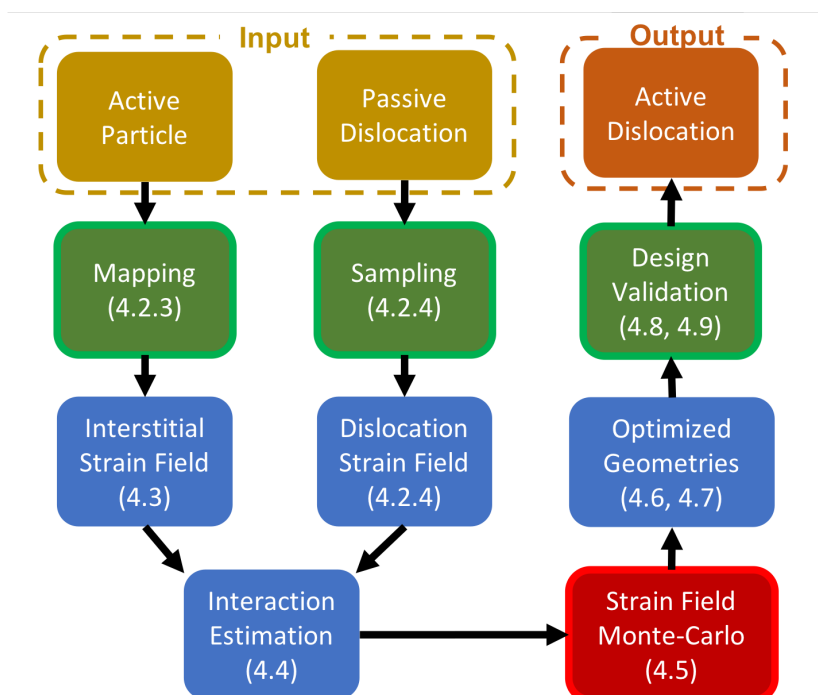
Figure 4.2: Schematic flow of information in this study. Green boxes indicate that molecular dynamics methods are used in that step. The red box indicates our newly developed strain alchemy algorithm. Boxes are labeled with matching sections when appropriate.

4.2 Model and Methods

To optimize the interaction between an interstitial and a dislocation as a function of interstitial geometry, the strength of the interaction must be measured for each trial geometry. This presents a difficult sampling problem, as thermalized strain fields must be sampled over long time scales and dislocations require large simulation sizes due to their long-range interactions. To address this difficulty, we propose a technique we term 'strain alchemy'. In a typical alchemical simulation [95], the free energy of a system is minimized by allowing some design parameter of the particle interaction to fluctuate as a thermodynamic quantity over the course of the simulation. This procedure results in near-optimal interaction parameters for the target state. Such a tactic involves

making trial changes to an interaction potential, and then sampling system configurations with a molecular dynamics (MD) or Monte-Carlo (MC) simulation [95].

Instead of directly proposing new interstitial shapes, we develop a method in which the strain field produced by the interstitial is allowed to fluctuate. Provided the magnitude of this strain field remains low enough, then linear elastic methods can be used to calculate the free energy of interaction of this field with another – such as that produced by a dislocation. The optimal strain field is then translated into an optimal particle shape. By approximating the objects of interest as strain fields we avoid extensive MD or MC sampling for each trial move. In this study, we develop this strain alchemy algorithm and apply it to the optimization of interstitial-edge dislocation and interstitial-loop dislocation interactions. In the the remainder of this section, we outline the model system and standard simulation techniques employed. Application of these techniques and development of new methods is covered in subsequent sections.

4.2.1 Interstitial Sites

A face-centered cubic (FCC) crystal of hard spheres at contact contains obstruction-free channels that lie in the $\{111\}$ family of planes along the $\langle 1\bar{1}0 \rangle$ family of directions. These are advantageous sites for interacting with gliding dislocations, as these planes and directions comprise the low-energy slip system for this crystal structure. Fig. 4.3a-b shows a rendering of the interstitial space present in the cubic close-packed crystal.

At finite pressures and temperatures, these channels locally fluctuate in width as particles undergo thermal motion. Lower pressures also lead to an expansion of the structure, increasing the available free space. If a rod of radius equal to the channel radius for hard spheres at contact is inserted into a nearly-hard-sphere crystal at finite pressure and temperature, local strain fields produced around it are negligible in magnitude. Small increases of rod diameter above this minimum will lead to small local strain values. This perturbative relationship between geometry and local strain field magnitude is advantageous for particle design, as it permits the use of linear elastic approximations. Furthermore, the channel geometry limits the height of hopping barriers during
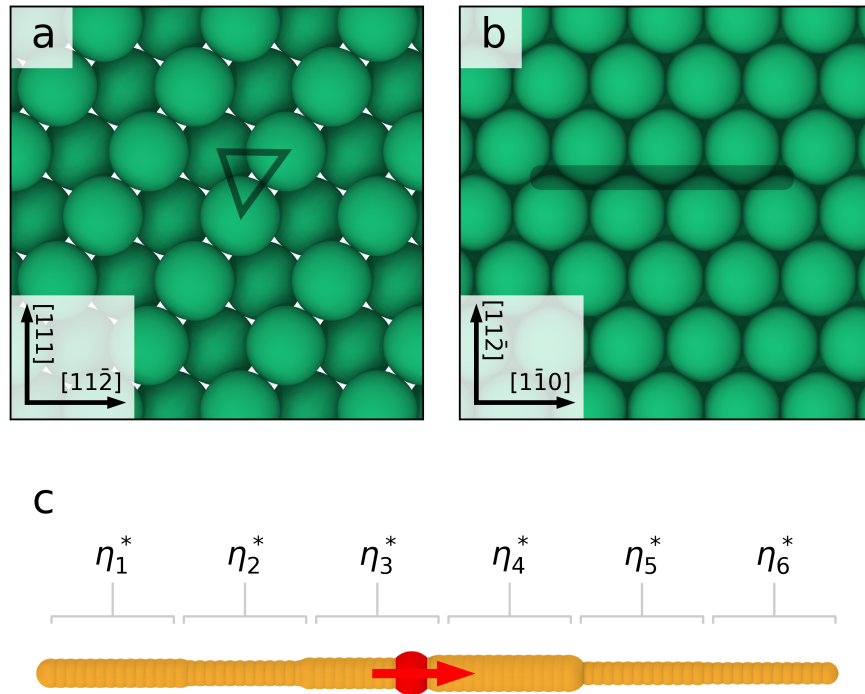
Figure 4.3: **a** A close-packed hard-sphere crystal showing obstruction-free channels aligned with the $\langle 1\bar{1}0 \rangle$ family of directions. The triangle highlights the columns of nearest-neighbor particles for the indicated channel. **b** In the here-depicted (111) plane of densely packed spheres, these channels correspond to troughs with triangular cross section, indicated by the shaded rectangle. **c** The probe particle model. Rigid-body segments (yellow) with repulsive interactions are rendered at the zero-energy isosurface. The center particle of the rigid body (red) coincides with the particle's center of mass. The mass, center of mass, and moment of inertia of the probe are calculated as though it is comprised of overlapping spheres of the same density as the lattice particles. A force (red arrow) is applied along the probe axis. The probe shown is one example of a sequence of segment diameters.

interstitial motion. For a spherical interstitial sitting in tetrahedral or octahedral sites in FCC, motion between sites must be accompanied by local lattice strains that (temporarily) far exceed the linear elastic regime. By working within the channels, the maximum strain induced during particle motion can be limited to the maximum strain produced by the particle at rest, and so particle mobility is treatable within the linear elastic framework.

4.2.2 The Interstitial Particle

In this study our interstitial probe particle of interest is a segmented rod. We wish to impart to this probe enough degrees of freedom to optimize its interaction with a dislocation's strain field. Therefore, the probe is split into segments, each $a/\sqrt{2}$ long (where a is the lattice constant of the host crystal). This is the smallest meaningful distance at which the local strain of the host lattice can be measured, and yields 'internal' degrees of freedom for the probe equal to one value (the strain magnitude η^*) for each segment. These segments are allowed to change independently during optimization. Beyond internal degrees of freedom, the probe's position relative to the dislocation core can also be changed: it can be placed in any of the channels present in the $\{111\}$ family plane parallel to the $\langle 1\bar{1}0 \rangle$ family of directions (indicated in Fig. 4.3b). Fig. 4.3c shows a schematic of the rod geometry used in MD simulations (See section 4.2.4 for MD methods).

4.2.3 The Method of Eigenstrains

To predict the strain field surrounding an interstitial we employ the method of eigenstrains [90]. Each segment of the interstitial probe will be represented by a single strain value. These strains can be called 'non-elastic' because they arise from displacements of particles by the interstitial, not by a stress field. Adopting Mura's terminology, we refer to these strains as 'eigenstrains'. The total strain (ϵ_{ij}) in the system is taken to be the sum of the non-elastic eigenstrain (η^*_{ij}) and the elastic strain (η_{ij}). For a continuum material at rest, the relation $\epsilon_{ij} = \frac{1}{2}\left(\frac{\partial u_i}{\partial x_j} + \frac{\partial u_j}{\partial x_i}\right)$ holds (where $\vec{u}$ is the displacement vector and $\vec{x}$ is the position vector). This relationship between strains and displacements is known as 'compatibility'. Such a relationship allows the elastic deformation η_{ij} to be found for arbitrary eigenstrains. In this work we employ an implementation of the Fourier transform method of computing total strain distributions from eigenstrains based on the equations presented by Mura [90] and validated against analytic solutions for inclusions derived by Chiu [114]. The elastic strain field found in this way can be directly connected to the deformation free energy of the material in the small strain limit [85].

When considering a rod-like interstitial at rest in the $\langle 1\bar{1}0 \rangle$ aligned channels of the FCC struc-

49

ture (section 4.2.1), an increase in interstitial diameter does not produce a purely dilatory displacement of nearest neighbors. This is because (unlike for tetrahedral or octahedral interstitial sites) all neighbors of the $\langle 1\bar{1}0 \rangle$ channels are not equidistant from the channel center. The correct relation between probe diameter and channel neighbor displacements (i.e. eigenstrain) was found semi-analytically. An eigenstrain matrix was found (algebraically) which displaced the nearest neighbors of the close-packed channel sufficient to clear enough space to fit a probe of given diameter. A corrective scaling factor was required to match the eigenstrain sampled from simulations of uniform diameter probes to this derived eigenstrain matrix. The scaling factor is needed because the derived eigenstrains where found from the close-packed FCC crystal geometry, and the simulations are conducted at finite pressures and temperatures.

4.2.4 Molecular Dynamics Methods

All MD simulations reported here are performed with `HOOMD-blue` [112, 113]. In simulations of dislocations, all lattice particles interact via the shifted-Weeks-Chandler-Andersen potential[111] (SWCA), whereby the origin is shifted to the surface of the particle. The value of σ used in this potential was set to 0.07, and the potential was shifted in radius so that the minimum (located at $\sigma 2^{1/6}$ in the unshifted case) is at a distance of $2^{1/6}$. In this work we will refer to the diameter of the host particles as D, which is equal to $2^{1/6}$. Simulations were carried out in the NPT ensemble via equations derived by Martyna et al. [84]. System thermal energy was held at $kT = 0.1$, pressure at $P = 2$, and particle mass was fixed at $m = 10$ (in simulation units). This choice of parameters yields a crystal with an acceptably large range of linear elastic behavior [79]. The elastic modulus tensor was sampled via fluctuations of the system box parameters and stress tensor [88].

Stain-field representations of line and loop dislocations were sampled from MD simulations. Dislocation line arrays were created by subtraction of a half plane of particles in a simulation box spanning 60 unit cell lengths in the x direction (aligned with crystal direction $[1\bar{1}0]$), 24 unit cell lengths in the y direction (aligned with crystal direction $[11\bar{2}]$), and 20 unit cell lengths in the z direction (aligned with crystal direction $[111]$). Particles within a rectangle spanning one Burgers

vector in the x direction, the full box width in the y direction, and half the box height in the z direction were deleted from an initially perfect crystalline domain. The crystal in between the top and bottom of the deleted rectangle was then stretched in the x direction, so that the gap was closed. Fig. 4.4ai-ci shows this process for the preparation of arrays of line dislocations.

Upon MD simulation, this initial configuration rapidly equilibrated into two partial dislocation pairs, with glide planes separated by one half of the height of the simulation domain. Box boundary conditions are all periodic, and the final particle count was 346,992. Per-particle strain fields were collected from 100 decorrelated samples, and a voxelized representation was created by binning. Bins form an isotropic grid with orthogonal distance $a/\sqrt{2}$ between bin centers. The final line-dislocation strain tensor has size $139 \times 32 \times 56 \times 3 \times 3$.
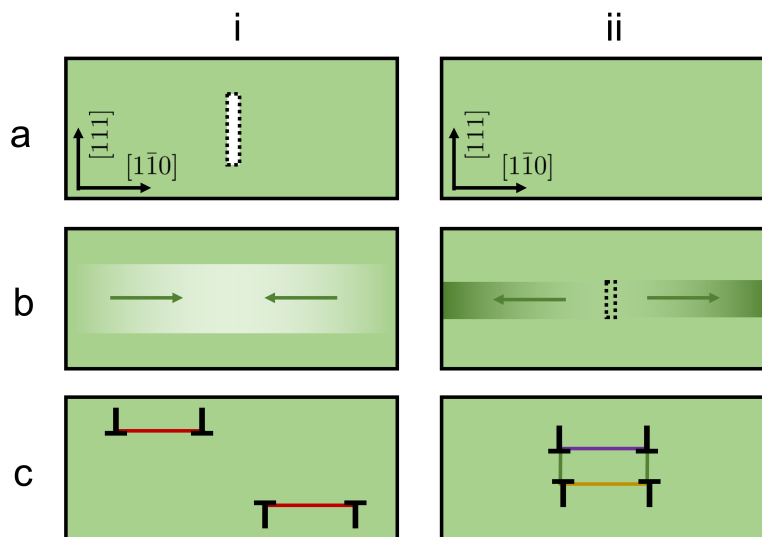
Figure 4.4: Schematic of how line dislocation arrays (column **i**) and dislocation loops (column **ii**) are prepared for MD simulation. **ai** An initially perfect crystal domain (green), has a rectangular section deleted from it (dashed box). The deleted volume is as wide as the box, half as tall as the box, and one Burgers vector in thickness. **bi** Regions of the crystal within the central half of the simulation box are stretched (linearly) so as to fill in the deleted section (indicated here by a color gradient). **ci** Once MD simulation has begun, the distorted crystal rapidly relaxes into a pair of partial dislocations (indicated by ⊥), connected by stacking faults (red lines). **aii** An initially perfect crystal domain (green). **bii** Regions of the crystal bounded by the loop glide cylinder are compressed (linearly) so as to open up a space (dashed box) into which an additional plane of particles is added. **cii** Once MD simulation has begun, the distorted crystal rapidly relaxes into a dislocation loop (indicated by ⊥), connected by Shockley partials (green), Hirth (purple), and stair-rod dislocations (purple).

Due to the compact size of the dislocation loop, we used a smaller simulated domain without strong loop-loop interactions across the periodic boundary conditions. The simulation contained a crystal domain of the same orientation as used for line dislocations but containing $30 \times 20 \times 16$ unit cell lengths in the x, y, and z box directions (corresponding to $[1\bar{1}0]$, $[11\bar{2}]$, $[111]$ crystal directions, respectively). The extrinsic loop was created by the addition of a parallelogram of particles 1 plane thick in the x direction and 3 particles wide and tall. To make room for the extra particles, a section of the initially perfect crystalline domain bounded by the glide tube of the dislocation loop was compressed along the x direction, which opened up a gap in the center of the simulation domain. The extra half plane of particles was then inserted into this gap. Fig. 4.4aii-cii shows this process for the preparation of dislocation loops.

Upon MD simulation, this initial configuration rapidly equilibrated into a dislocation loop. The total lattice particle number after loop formation was 115,209. The strain field surrounding a loop was sampled in the same manner as the line dislocation, yielding a loop dislocation strain tensor of size $69 \times 40 \times 45 \times 3 \times 3$.

In all cases the segmented probe is simulated as a collection of isotropic repulsive potentials (interacting via the same SWCA potential as the lattice particles). To produce variations in segment diameter, the radial shifting of the SWCA potential is varied accordingly. Relative positions are maintained and torques handled during MD integration by rigid-body simulation [149].

4.3   Interstitial Particle Strain Field Mapping

Since we use the strain field produced by the interstitial to estimate interaction energies and probe mobilities, it is important that the analytically predicted field is sufficiently accurate. Fig. 4.5 shows a slice through the center of the strain field surrounding a probe of constant radius. The MD sampled field (4.5a) and analytically predicted field (4.5b) show good agreement in distribution and magnitude for regions not in direct contact with the interstitial. In these plots, one pixel corresponds to a region of crystal $a/\sqrt{2}$ per side.
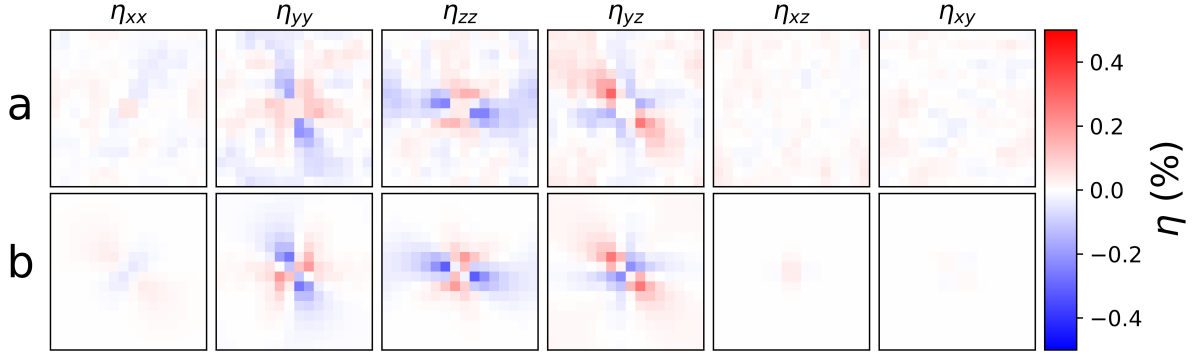
Figure 4.5: Comparison of sampled **a** and predicted **b** strain fields for a segmented rod interstitial. A single slice of the strain field is shown through the midpoint of the probe, with the long axis normal to the image plane. The sampled and predicted field show good agreement overall with only minor differences for regions in closest contact with the interstitial.

As segment radius is increased, eventually significant differences in strain magnitude arise between the predicted and sampled fields. This is because the methods employed here are only applicable in the small-strain (linear elastic) limit. When the radii of probe segments are permitted to fluctuate, an upper limit is used to restrict the search to the linear regime. Fig. 4.6 shows the strain free energy density of the sampled and calculated strain fields (E/V) vs. segment diameter (D_{seg}) for the complete particle geometry to strain field mapping.

The analytically calculated eigenstrain solution free energy remains quadratic for all starting vales of D_{seg}. The sampled strain free energy curve diverges from the quadratic prediction for large segment diameters. The strains produced by large diameter segments are too large to be treated accurately by the linear elastic approximations central to the methods used here. For this reason we restrict ourselves to exploring segmented rod particles with diameters less than $0.20D$. This caps the maximum relative prediction error (show in Fig. 4.6 inset) at 50% (in practice, high-fitness geometries we found to have lower diameters).
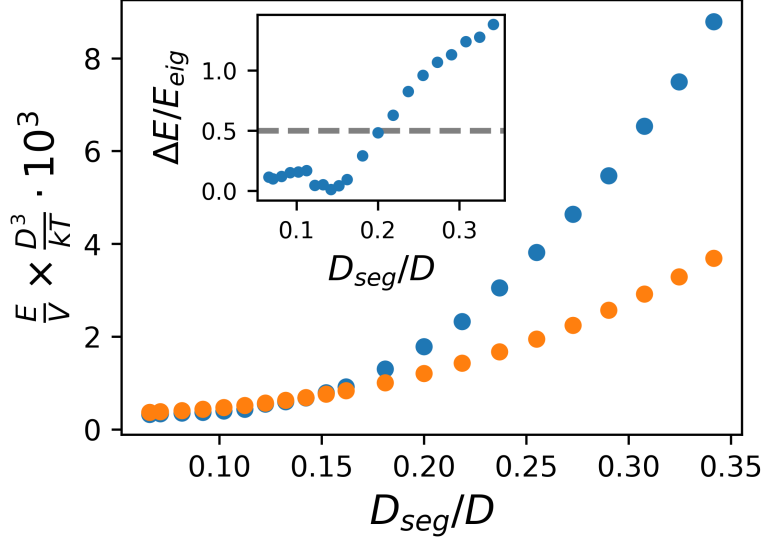
Figure 4.6: The strain free-energy density of a region around the probe interstitial versus segment diameter. The sampled values (in blue), diverge from the value predicted by the method of eigenstrains (in orange color) for segment diameters above $\sim 0.15D$. The inset shows relative error of the prediction, with a guide line at 50%. All curves have error bars (found via bootstrapping) that are smaller than the data markers.

4.4 Interaction Estimation via Interstitial Mobility Estimation

With the ability to map the strain field of a segmented probe particle to its geometry, the path is clear to use a Monte-Carlo (MC) style optimization scheme to maximize the interaction free-energy between the rod and another strain-field-producing object (such as a dislocation). Within the linear elastic approximation, linear superpositions of fields are also valid fields. Therefore, the strain field of the rod under design can be superimposed with the strain field of a dislocation and the total strain field energy evaluated according to the expression [85]:

$$F_{elastic} = \int_{\vec{r}} \frac{V}{2} \sum_{ijkl} C_{ijkl} \eta_{ij}(\vec{r}) \eta_{kl}(\vec{r}), \qquad (4.1)$$

where $\eta(\vec{r})$ is the strain tensor describing a volume V centered at position $\vec{r}$. Here the tensor field η is the sum of two tensor fields, one representing the probe and one the dislocation. C_{ijkl} is the elastic modulus tensor. By comparison to the strain-field energy of both fields widely separated,

interaction energies as a function of relative position can be determined.

Before optimization, a likely guess as to what kind of strain field maximizes the interaction between a segmented probe and a dislocation is straightforward: larger probe strains will always increase repulsive interaction strength, while fields that result in total cancellation of the dislocation's field will likely maximize attractive interactions. However, we are not concerned here only with the interaction strength, but also the mobility of the probe. In order for an active interstitial to interact with a dislocation, it must have sufficient mobility to move through the defect-free crystal. Upon encountering a dislocation, the desired behavior is to then become bound, unable to escape from the vicinity of the defect. If we assume that particle migration through the crystal is achieved by hopping through a periodic free-energy surface (with the periodicity defined by the geometry of the crystal in the direction of travel), then we seek an interstitial with location-dependent barrier height (d). Far from the dislocation, the barrier (d_{far}) should be as low as possible, while the barrier in the vicinity of the defect (d_{near}) should be as large as possible. Consequently, we seek a particle geometry optimization which takes into account the free-energy barrier that limits probe mobility. We expect both d_{far} and d_{near} to increase with an increase in probe strain, which means that high mobility and strong defect interaction are competing design goals.

It is possible to estimate this barrier height from the strain field that surrounds a segmented probe interstitial (which can be rapidly predicted using the method of eigenstrains). This method of approximation relies on the special geometry of the segmented probe particle: because each segment imposes local strains that are within the linear regime, there will be no high-strain intermediate states as the probe hops from one site to the next. The barrier to probe movement then arises due to the strain free-energy that is dissipated in each hop. As the probe approaches new volumes of the pristine crystal, it imposes strain, which increases the local free energy. Simultaneously, regions from which the rod leaves relax their local strain free energy. This relaxed free-energy is not recaptured by the rod, but instead escapes as heat. Therefore the hopping of an interstitial rod requires that new strain energy be stored in volumes ahead of the particle motion, while previously stored strain free energy is not recovered. This is the source of resistance to mo-

tion. The value of this hopping barrier can be calculated from a given strain field according to Eq. 4.2:

$$d = \sum_{\vec{r}} ||F_2(\vec{r}) - F_1(\vec{r})||$$

$$F_1(\vec{r}) = \frac{V}{2} \sum_{ijkl} C_{ijkl} \left[\eta^D(\vec{r}) + \eta^I(\vec{r})\right]_{ij} \times \left[\eta^D(\vec{r}) + \eta^I(\vec{r})\right]_{kl} \qquad (4.2)$$

$$F_2(\vec{r}) = \frac{V}{2} \sum_{ijkl} C_{ijkl} \left[\eta^D(\vec{r}) + \eta^I(\vec{r} + d\vec{r})\right]_{ij} \times \left[\eta^D(\vec{r}) + \eta^I(\vec{r} + d\vec{r})\right]_{kl}$$

with C_{ijkl} being the crystal's elastic modulus, V is the volume of an element centered at $\vec{r}$, η^D the strain field of the dislocation, and η^R the strain field of the segmented probe interstitial.

4.5   Strain Field Monte-Carlo Algorithm

The optimization of probe-dislocation strain-field-mediated interaction is carried out through a Monte-Carlo style algorithm we developed for this work. The domain of optimization is a voxelized grid, represented by an $n \times m \times o \times 3 \times 3$ tensor, where each point of an $n \times m \times o$ grid (representing the physical dimensions of the optimization area) has a 3×3 local strain tensor. The optimization requires two such tensors: a background tensor, encoding the local strain surrounding a dislocation or other object of interest, and the design tensor, which encodes the values of local strain produced by the probe interstitial. The background tensor's values and size are set by a voxelization procedure used to measure time-averaged local strain in an MD simulation, described elsewhere [79]. The design tensor is used in two forms: the eigenstrain and strain representations. These forms are related through the method of eigenstrains [90]. Changes to the segmented probe interstitial's geometry are represented through changes to the eigenstrain design tensor, which is then converted into the strain representation before evaluation is carried out. Since the conversion from eigenstrain representation to strain representation is the limiting step, and the extent of

the strain field of the segmented rod interstitial is much smaller than the sampling of the dislocation's strain field, the design tensor can have fewer elements (cover a smaller volume) than the background tensor. The steps in choosing a strain configuration and evaluating its fitness are as follows:
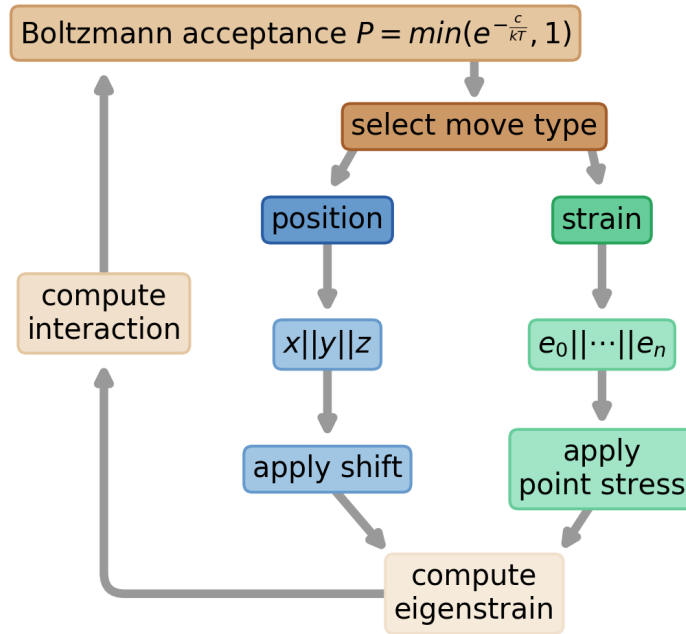
Figure 4.7: Schematic of the strain alchemy MC loop with multiple move types, each having associated parameters from which to select. For positional moves, the Cartesian direction of movement $(x||y||z)$ is chosen. For strain moves a single-segment eigenstrain (e_i) is chosen.

1. Select a segment of the probe and assign a new diameter value to it.

2. Set the elements of the eigenstrain design tensor that correspond to this probe segment to values which describe the displacement caused by this diameter.

3. Compute the strain representation of the design tensor with the method of eigenstrains.

4. Shift (with edge wrapping) the strain design tensor so that the probe origin is near the dislocation core and evaluate the hopping barrier, d_{near}.

5. Shift (with edge wrapping) the strain design tensor so that the probe origin is at a location far from the dislocation core. Compute the estimate of the hopping barrier d_{far}.

6. Calculate the fitness of the design tensor as $f = d_{\text{near}} - d_{\text{far}}$.

7. Accept the new design tensor with probability $e^{(f-f_0)/kT_{\text{alch}}}$, where f_0 is the fitness of the previously accepted design tensor, and kT_{alch} is a thermal energy that can be lowered over the course of the optimization to restrict the magnitude of strain field fluctuations.

8. Repeat until convergence (or until kT_{alch} is reduced to a negligible value).

The values of d_{near} and d_{far} depends strongly on the position of the probe relative to the glide plane. To avoid introducing assumptions concerning which location will produce the fittest solution, changes to the position of the probe can also be included in the MC procedure. For this study positional moves are made less often than strain moves. Fig. 4.7 shows the flow of the MC loop when multiple move types are employed.

4.6   Use Case: Line Dislocations

Using the procedure outlined in section 4.5, the interaction of a segmented probe interstitial and a line dislocation of pure edge character was performed (see section 4.2.4 for details). The eigenstrain representation of the particle is comprised of 6 coupled blocks of 4 voxels each, centered in the design tensor. The number of blocks represents segments of the probe. 6 was chosen as the number of segments to avoid excessively high aspect ratios. Segment radii are permitted to approach 0, effectively shortening the probe if advantageous for optimization. The size of the design tensor was sufficient for strain fields to decay to negligible values at the edges of the domain.

   The initial eigenstrain value (e_i) was set to 0.05 for all probe segments (and an upper constraint of $e_i = 0.15$ was set). The optimization temperature, kT_{alch} was logarithmically decreased from a starting value of 10^{-2} to 10^{-3} over 10^5 iterations. These temperature values were chosen so that the average acceptance likelihood transitions from high to low at the approximate midpoint of the

58

run. At each MC iteration a move was randomly selected. For optimization of line-dislocation probes, strain type moves were chosen with a 90% probability, with the remainder being evenly split between x and z positional moves. Moves in y were not considered, as they would lie parallel with the dislocation line direction.

Fig. 4.8 shows summary information from 100 MC trials preformed on line-dislocation arrays. The final locations that maximize interaction (shown in Fig. 4.8d) are clustered on the leading edge of the dislocation, near the tensile lobe associated with the η_{zz} field. Fig. 4.8c shows histograms of the segment geometries. The distributions are broad, however mean values display a clear trend of high values at the probe ends, and low values at the center. This dog-bone configuration appears to maximize the probe's escape barrier when near a lobe of the dislocation's η_{zz} field. The top six highest fitness solutions are shown in Fig. 4.9a. Aside from the average trends of high diameter ends and low diameter middles, some high-fitness geometries also have a large diameter central segment, resulting in a serrated appearance. This appears to be a further refinement of the average trend.
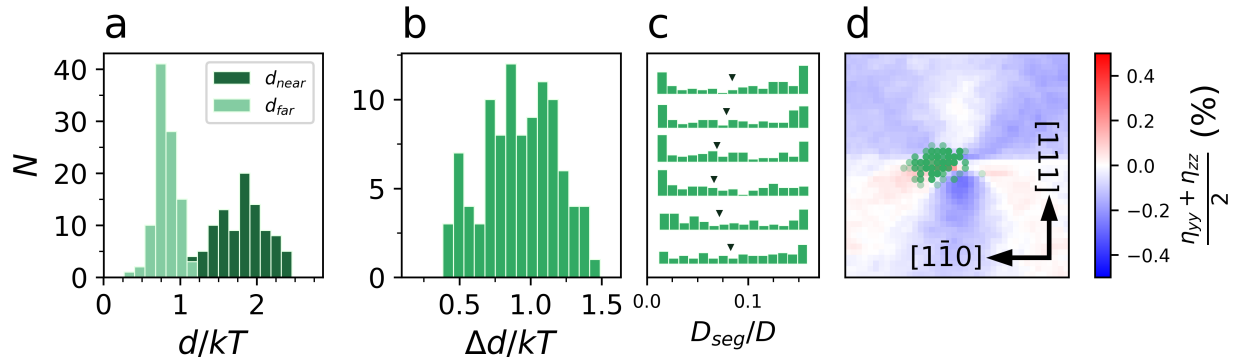
Figure 4.8: The aggregated results of 100 MC solver runs on an edge dislocation. **a** Histogram of the barriers estimated from the eigenstrain procedure. **b** Distribution of solution fitness, as defined by the difference of barriers near and far from the dislocation. **c** Histograms of the diameters of each of the six segments that comprise the probe. The mean of each distribution is indicated with a chevron. **d** Location of final solution position, relative to dislocation core.
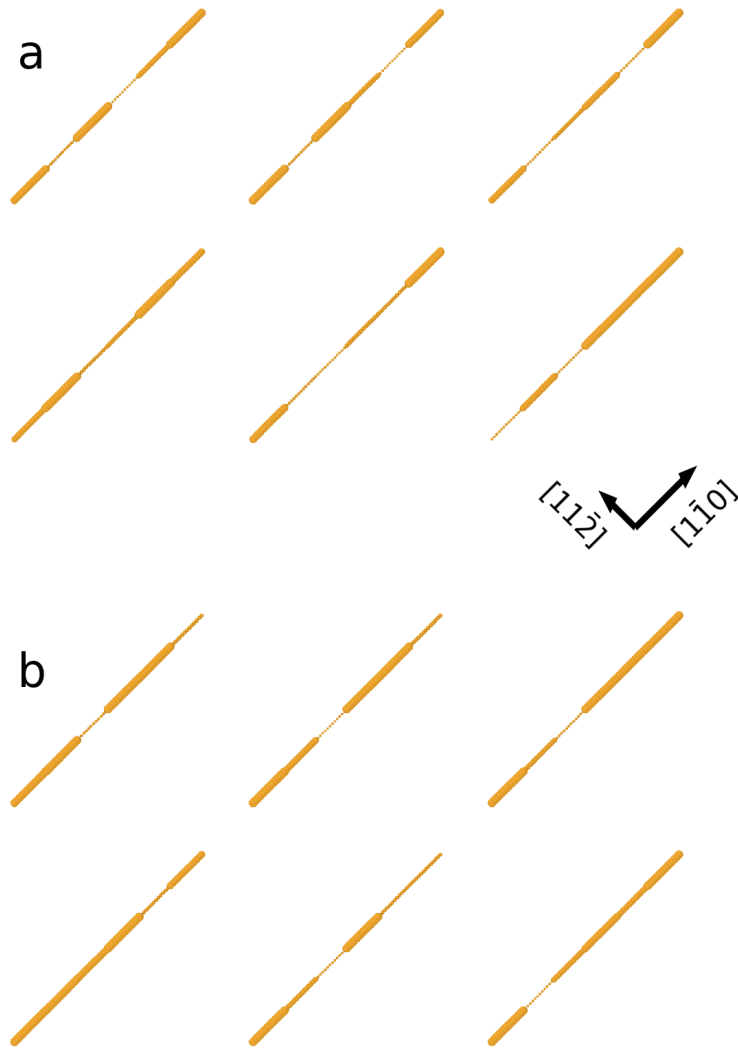
Figure 4.9: Renderings of the top six optimized probes for interacting with an edge dislocation (**a**) and extrinsic dislocation loop (**b**). The surface rendered is the zero-energy isosurface of the SWCA potential. Directions relative to the rod when placed in the host crystal are noted. The average line direction of Shockley partials is parallel to $[11\bar{2}]$.

4.7   Use Case: Dislocation Loops

The same MC procedure (section 4.5) as for line-edge dislocations (section 4.6) was applied to extrinsic dislocation loops (see section 4.2.4 for details). For loop-dislocation probes, x, y, and z

moves are permitted. Strain moves were chosen with 91% probability with the remainder of moves evenly split among x,y, and z. Fig. 4.10 summarizes the results of 100 MC trials on the sampled loop strain data. The higher values of mobility barriers in the neighborhood of the dislocation loop immediately become clear. The strain fields perpendicular to the loop glide axis are higher in magnitude than those surrounding a line-edge dislocation. The line dislocation has negligible strain values in the direction parallel to the line vector; most strain energy is contained in the field parallel to the glide direction. The bending of the dislocation-loop lines produces a more highly strained local environment for the probe to interact with. The locations of maximum interaction are distributed within the area of the loop. There is a preference for the compressive corners of the loop over the tensile corners. The histogram of segment diameters reveals large populations of high and low diameters (and a relative lack of intermediate diameters), with almost no pattern to how these segments are ordered. Fig. 4.9b shows the top six solutions of optimal probe shape, highlighting again that the key feature for optimal interaction is a low-strain segment surrounded by large-strain segments. There seems to be no strong preference for where on the probe the small segment is placed.
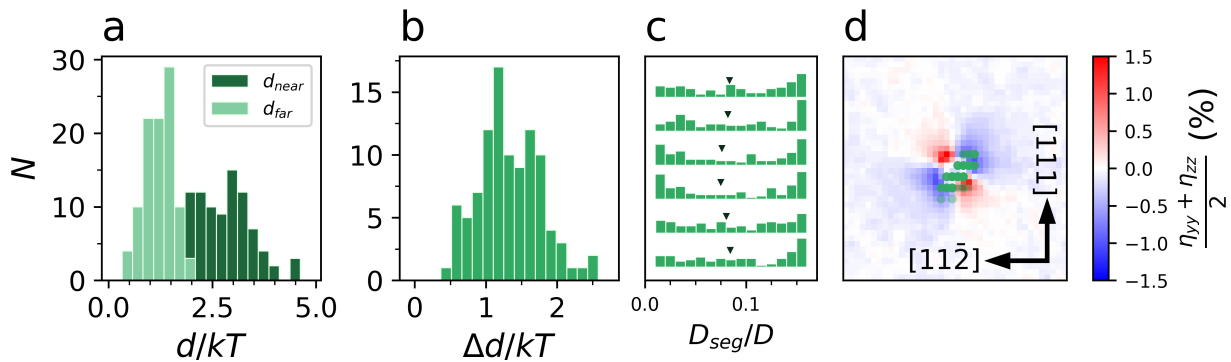
Figure 4.10: The aggregated results of 100 MC solver runs on an extrinsic dislocation loop. **a** Histogram of the barriers estimated from the eigenstrain procedure. **b** Distribution of solution fitness, as defined by the difference of barriers near and far from the dislocation. **c** Histograms of the diameters of each of the six segments that comprise the probe. The mean of each distribution is indicated with a chevron. **d** Location of final solution position, relative to dislocation loop center axis.

4.8 MD Validation of Barrier Estimation

To test the validity of estimating hopping barriers from predicted strain fields (section 4.4), the optimized probes found in sections 4.6 and 4.7 were placed within a defect-free FCC crystal domain and a force was applied that aligned with the rod's axis. Several hydrostatic strains were applied to the simulated crystal in order to test the rod's mobility in different strain environments. Fig. 4.11a shows the average velocity of the rod under different magnitudes of force ($\vec{f}$) for different hydrostatic strain conditions. Curves are fit to the velocity data using the Fokker-Planck equation solution for a periodic 1D potential [150]. Two free parameters—the barrier height (d_{fit}) and the damping constant (γ)—were used for the fit. Barrier heights were compared to those found from the optimization process (d_{eig}). Fig. 4.11b shows the comparison of the estimated and fit barrier height. The fit and predicted values have a constant offset, but are otherwise related linearly with a proportionality constant close to unity. The origin of the offset is unknown, but may be a product of the fluctuating probe orientation and thermal bending of the interstitial channels, which are effects neglected by the estimation method. The value of γ found by fitting is related linearly to the pressure of the crystal (see Fig. 4.11). This trend in γ reveals that strained environments can change the frequency of collisions between the interstitial and the crystal particles, which is an expected result. In optimization of the probe geometry, this γ effect can be neglected, since it is predominantly important at high forces. Additionally, since γ is positively linearly correlated with d, both parameters need not be considered to maximize differences in average particle velocity.

4.9 MD Simulation of Interstitial-Dislocation Interaction

To test the validity of the solutions (sections 4.6 and 4.7) produced by the MC optimizer, MD simulations were performed. The optimized probe particle was placed within the simulated crystal (the same geometry as was created for sampling of the defect strain fields) at the location of maximum interaction found by the optimization, with a force applied to the rod along its long axis. Fig. 4.12a shows the relationship between the distance traveled by the optimized probe, and the
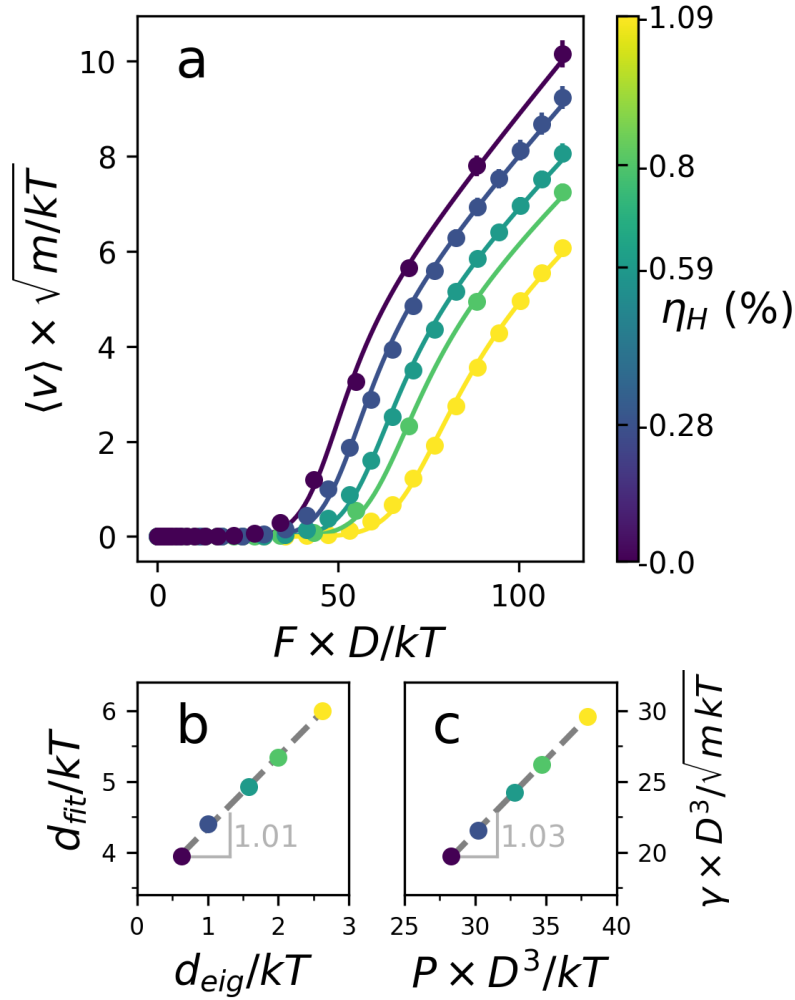
Figure 4.11: **a** Probe interstitial velocity as a function of force for various conditions of hydrostatic strain. Curves are fit as functions of γ and barrier height, d_{fit}. **b** Relationship between the fitted value of d and that predicted by the eigenstrain estimate. **c** Relationship between the fit value of γ and pressure. The quantity $\gamma \cdot D^2$ scales linearly with applied system pressure.

slip between a pair of tagged tracers positioned on either side of the dislocation slip plane. On this plot, a slope of 1 indicates that the dislocation and the optimized probe are traveling together, producing one Burgers vector of slip per full transit of the periodic box by an optimized probe. As the force exerted by the interstitial is increased, the total distance traveled by the dislocation and the probe increases. The inset in Fig. 4.12a shows the velocity of the probe as a function of force. A local velocity maximum near $f \simeq 9.0$ is observed. For $f > 16.8$ the probe becomes completely unbounded from the dislocation. The dislocation array stops moving unidirectionally and

the probe's velocity as a function of force becomes monotonic. Fig. 4.12b-e shows renderings of simulations where the probe particle is interacting with a partial edge dislocation line. Also shown is a slice of the simulation domain before and after the dislocation array was driven to glide across the periodic box several times. The central segment of the crystal can be seen to have slipped past the remainder of the system. This slip increases by one full Burgers vector magnitude for each time that the partial dislocation pair transits the periodic simulation domain in the $[1\bar{1}0]$ crystal direction.

The same study and analysis was also conducted for the dislocation-loop-optimized probe. In this case one of the tagged tracer particles was placed within the glide cylinder of the tube. Fig. 4.13a shows the correlation of optimized probe travel and loop travel as a function of force. As these simulations were run for the same amount of time as the line dislocation tests, it is clear that the mobility of the loop-probe pair is much higher. The striking difference in mobility for loop and line dislocations is not surprising, as loops contain a much shorter length of dislocation line that has to glide. In the simulations shown here, the length of Shockley dislocations present in the loops is $\sim 18a$ (with the total length of all dislocations $\sim 30a$), while line dislocation simulations contained only Shockley partials spanning $\sim 120a$. The escape force for the loop optimized probe is larger than that for the line dislocation, above $f \simeq 29.2$. The probe's velocity (Fig. 4.13a inset) as a function of applied force shows similar features to the line dislocation case, however the local maximum ($f = 16.8$) and minimum ($f = 29.2$) are more distinct. The increased force value of the maximum and minimum is consistent with the higher Δd achieved for the optimization of the loop probe. Fig. 4.13b-e shows images of the simulated loop-active particle system. Fig. 4.13c shows the dislocation lines present in the extrinsic loop, as found with the DXA algorithm [151] implemented in OVITO [117]. The loop structure is comprised of three dislocation types: partial (Shockley) dislocations, forming the two ends of the dissociated dislocation loop tube, as well as stair-rod dislocations and Hirth dislocations at the corners of the loop, with line directions parallel to the glide axis of the loop. Similar to the case of the line dislocation array, multiple transits of the dislocation loop through the simulation cause slip of the regions bounded by the glide cylinder.
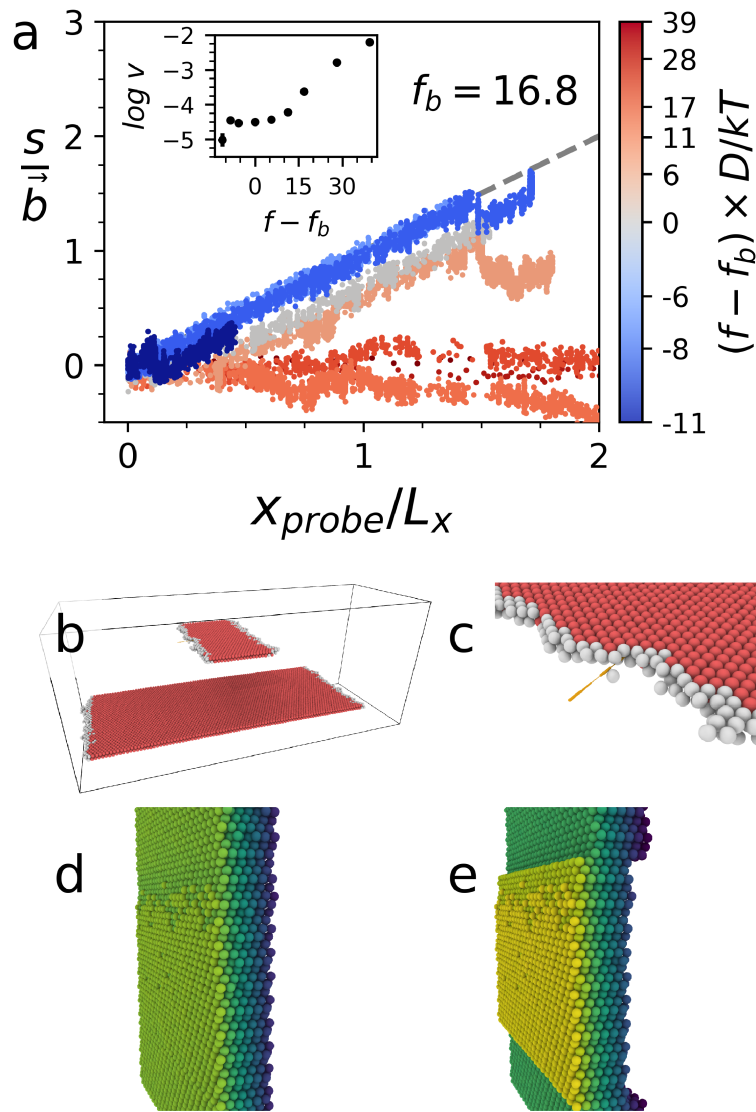
Figure 4.12: **a** Optimized probe distance traveled versus slip of the central region for a simulated edge dislocation array. Particle forces above $f_b = 16.8$ result in small slopes, indicating that the active particle escapes from the vicinity of the dislocation. The inset shows the velocity of the optimized probe as a function of force. There is a local maximum in velocity before the breakaway force. Snapshots of the optimized probe as it interacts with a partial edge dislocation, rendered with OVITO [117]. **b** The dislocation array, shown with all particles having an FCC-like neighbor shell removed. The red particles are members of the stacking faulted layer and the white particles are members of the disordered core. **c** Close-up of the optimized particle as it interacts with one of the partial dislocations. **d** A slab of particles at the start of the simulation, color coded by x position. **e** The same particles after several passages of the dislocation array through the box.
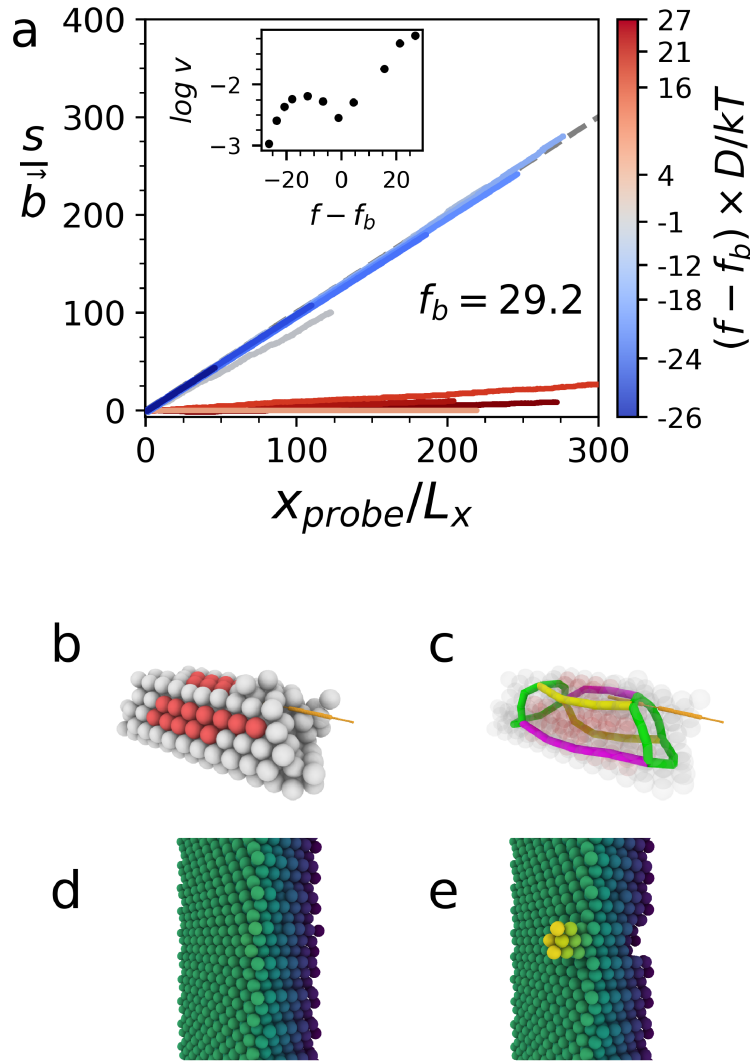
Figure 4.13: **a** Optimized probe distance traveled versus slip of the loop glide cylinder region for a simulated extrinsic dislocation loop. Probe forces above $f_b = 29.2$ result in small slopes, indicating that the active probe escapes from the vicinity of the dislocation. Inset shows the velocity of the probe as a function of force. Snapshots of a segmented rod interstitial particle as it interacts with an extrinsic dislocation loop, rendered with OVITO [117]. **b** Close-up of the dislocation loop structure with optimized probe nearby. Particles with FCC-like environments have been removed for visibility. Red particles are members of stacking faults, and white particles have disturbed neighbor shells. **c** Close-up with particles rendered transparently and dislocation lines highlighted: green lines are partial (Shockley) dislocations ($\vec{b} = \frac{1}{6}\langle 112 \rangle$), purple lines are stair-rod dislocations ($\vec{b} = \frac{1}{6}\langle 110 \rangle$), and yellow lines are Hirth dislocations ($\vec{b} = \frac{1}{3}\langle 001 \rangle$). **d** A slab of particles at the beginning of the simulation, colored by x position. **e** The same particles after several transits of the loop through the box.

66

The straight partial dislocations simulated in this study cross the periodic box boundaries, and so can be thought of as infinite in extent. Therefore, it is best to compare the performance of probes interacting with line and loop dislocations on a per-length basis. In a periodic box containing one probe particle and two straight edge dislocations that have decomposed into four Shockley partials, the breakaway force of the line dislocation optimized probe is $f/l \simeq 16.8/120a = 0.14/a$. If in the loop dislocation case we consider only the Shockley partial length, then the loop dislocation optimized breakaway force per unit length is $f/l \simeq 29.2/18a = 1.62/a$. The large difference in breakaway force on a per unit length basis emphasizes the increased coupling between a curved dislocation and the probe interstitial.

The probe interstitial can only interact via its strain field in a small volume (the volume of non-negligible strains produced by the probe). Ultimately, the small size of the probe results in strain fields that rapidly decrease in magnitude with distance, much like a point source. A bent dislocation, like those in a small loop, can fit more dislocation line length within range of the probe's strain field. In fact, the straight dislocation case can be compared to a very large diameter loop, which on length scales similar to the range of the probe's strain field appears straight. The results presented here show that as the circumference of a dislocation loop is scaled from $\simeq 9a$ to $\simeq 60a$, a greater than ten-fold reduction in optimal probe binding strength per unit length occurs due to the reduction of dislocation curvature. An implication of this result is that dislocation bends or jogs, which have locally high curvature should also be expected to strongly interact with the same probes that strongly interact with small dislocation loops.

4.10   Conclusions

We have shown that there is a robust mapping between the geometry of a repulsive segmented probe particle embedded as an interstitial in an FCC crystal of repulsive spheres and the local strain field that is produced around it. We exploited this predictive connection to allow the use of MC methods to design the nature of the interaction between the interstitial probe and other

strain-field-producing disturbances in the crystal. We have also shown that the mobility of such an interstitial is well-approximated through consideration of the strain field alone, and that by placing constraints on the mobility of the interstitial in different local environments (i.e. near to and far from a dislocation), the interaction between this interstitial and another object can be tuned. A striking feature of this design method is its computational efficiency. The simple Python implementation of the MC solver used here requires approximately one day per solution to run on a single CPU. In contrast, each trial force MD simulation of the line dislocation arrays requires a full week of NVIDIA® Tesla® P100 GPU time. If every trial geometry, position, and force required such a simulation for evaluation, then it would be unfeasible to carry out this scheme.

This work demonstrates a route towards microstructure control in colloidal materials through a designed, active tool particle interstitial that can manipulate internal defects. Currently, the most powerful tool for 3D microstructure creation available to colloidal scientists is templating, whereby the boundary conditions of crystallization are changed to favor the creation of desired defects. Our work complements such efforts by providing a means to re-configure microstructure *after crystallization has already occurred*, which opens the possibility for colloidal crystal mechanical and optical devices. Furthermore, increasing defect mobility by interaction with active interstitial probes is a route to lowering colloidal crystal defect quantity. Active particles designed in this way can be used to 'sweep out' undesired defects and microstructures. This work demonstrates a colloidal microstructure control scheme that exploits the designability of colloidal crystal subunits in a way not achievable with atomic materials.

CHAPTER 5

Pinning Dislocations in Colloidal Crystals with Active Particles that Seek Stacking Faults

This chapter and its figures are adapted from an as-yet-unpublished manuscript (Ref [81]) authored in 2019 by Bryan VanSaders and Sharon C. Glotzer.

5.1   Dynamic Deformation Behavior in Colloidal Materials

Colloidal machines assembled from sub-micron sized subunits provide a possible route to scaled down versions of so-called 'particle robots' [152]. Particle robots that sense and actuate are built from a collection of sub-units that, like colloidal particles, individually have limited functionality. The nascent field of colloidal robotics faces many challenges, including the need for dynamically responsive colloidal materials. Many of the functions we wish to realize are analogs to the capabilities of living cells. Unicellular organisms accomplish functional shape changes by stiffening and softening their cytoskeletal matrix dynamically [44]. A prototypical example is the unicellular predator *Amoeba Proteus*, which grows and reshapes extensions of itself to move and hunt. These changes are enabled by dynamic mechanical property changes and flows within the cell [43]. In mimicry of this functionality, researchers have investigated how the mechanical behavior of sub-μm particle assemblies can be coupled to external fields for controllable functional changes, for example by creating stiffness changing colloidal crystals [102] and magnetic 'microbots' [37, 39, 41].

When considering the deformation of dense arrangements of colloids, we can borrow from the extensive knowledge base concerning the deformation of metals to guide us. Metallurgists have gleaned deep insight into the mechanisms of deformation for materials with crystalline order, particularly the importance of dislocations in plastic deformation [67]. Under shear stress, dislocations migrate and effectively transport material though a crystal, resulting in shape change of the material at state points below the melting transition, and stresses below the ultimate yield strength. In this regard, colloidal crystals have been shown to behave similarly to metals [69, 70, 71, 97, 79]. A classical approach to impeding the motion of dislocations is to introduce impurity particles into the host crystal. Carbon steels are the prototypical example of this tactic; carbon interstitials significantly increase the shear stress required to drive a dislocation to glide when added to iron at concentrations of $< 1\%$.

Such interstitial pinning can be applied to colloidal systems to help control material deformation. Furthermore, colloidal particles and interstitials may have many designable and exotic properties, such as anisotropic shape or self-propulsion (i.e. active matter) [2, 92, 91, 92, 3, 35]. Active matter interstitials allow us to consider scenarios where the solute species is capable of self-propulsion and so travels super-diffusively. If such active interstitials can also be designed to bind strongly to dislocations and prevent their motion, then we could expect a comparatively small number of active interstitials to have a large effect on colloidal crystal plasticity. The migration of passive interstitials to dislocations is controlled entirely by the diffusive properties of the interstitial. As such, long timescales or high temperatures are required for passive solutes to accumulate around dislocations [153, 154, 67, 155]. Active particles could decouple the timescale of diffusion from that of dislocation pinning, as well as open the possibility of a metamaterial with dynamic, controllable plasticity via toggling activity.

In this study we explore the ways in which active anisotropic interstitials can interact with a dense crystalline environment via computer simulation. We show that anisotropic active interstitial particles can have strong, effectively attractive interactions with stacking faults in crystals composed of spheres interacting via isotropic steep repulsive potentials. These active particles ab-

70

sorb onto the stacking faults that link dissociated dislocation pairs, and thereby pin dislocations. We show that interstitial anisotropy and active force magnitude also affect the characteristics of the path explored by the interstitial. With the reduction of dislocation mobility as the primary goal of this study, we frame the design of active interstitials as a competition between the ability of the interstitial to move freely through the crystal bulk (so as to locate stacking fault binding sites) and the affinity of the interstitial to remain tightly bound to these sites. We propose a combined metric that assesses the overall effectiveness of an active interstitial as a dislocation-pinning additive, and test a high-performing interstitial in a dislocation-containing system under bulk shear. We find that for well-designed active interstitials, a number concentration as low as 64 per million host particles is sufficient to introduce significant barriers to dislocation glide and material plasticity.

5.2   Model and Methods

5.3   The Active Interstitial Model

The particles that comprise the host crystal are represented by purely repulsive isotropic pair potentials (the shifted Weeks Chandler Andersen potential [111]). The lowest free energy solid crystalline phase for such particles is face centered cubic (FCC), with hexagonal close packed (HCP) a close second [120]. FCC and HCP can both be constructed by alternating sequences of close-packed planes of particles (Fig. 5.1a-b). Dislocations in FCC crystals can dissociate into pairs of partial dislocations that conserve total Burgers vector [67]. These dissociated pairs are connected by a stacking fault, which is a local change of stacking sequence from FCC to HCP. The proclivity of dislocations to dissociate is controlled by the stacking fault energy, which is the free energy penalty of stacking fault creation [67]. In solids composed of short range repulsive potentials, this free energy penalty is very low, and so dislocations dissociate readily [120].

Stacking faults are low free energy defects for steep repulsive solids because the close-packed FCC and HCP stacking sequence motifs have no density differences. However the topology of the

71

void space in HCP is different than in FCC. Fig. 5.1a-b shows the stacking sequence of FCC and HCP planes, respectively. The HCP crystal has linear, connected voids that are parallel to the dense packed plane normals (the HCP $[0001]$ and FCC $[111]$ crystal directions). In FCC, these voids can only extend for three layers before they are interrupted. Fig. 5.1c shows a stacking fault embedded in an FCC crystal. This stacking fault introduces linear channels that span five stacking planes. In a close-packed crystal of diameter D spheres, this void channel has a length of $(\frac{5\sqrt{6}}{3} - 1)D \approx 3.1\,D$ and minimum open diameter of $(\frac{2}{\sqrt{3}} - 1)D \approx 0.15\,D$.

In this study our interstitial particle is a rod composed of repulsive potentials. Rod-like interstitials fit within void channels of the FCC crystal structure, and are known to have geometry-dependent mobility [80]. When active, the rods have three parameters (Fig. 5.1d) that govern their behavior: end-to-end length (L_r), diameter (D_r), and active force magnitude (f). Here activity is represented by a constant force, directed parallel to the long axis of each interstitial. Fig. 5.1d shows a schematic of the rod geometry used in this study. We considered changes to the rod's diameter, length, and driving force. Forces ranging from $3\,kT/D$ to $45\,kT/D$ were applied to rods with maximum distance between beads $0.5D$ to $3D$, and diameters $0.2D$ to $0.4D$. Total end-to-end rod length (L_r) is equal to distance between the centroids of the end beads plus the bead diameter.

5.3.1   Molecular Dynamics Methods

All molecular dynamics (MD) simulations reported here were performed with `HOOMD-blue` [112, 113]. All particles interact via the shifted-Weeks-Chandler-Andersen potential (SWCA) [111]. The value of σ used in this potential was set to 0.2, and for the host particles the potential was shifted in radius so that the minimum (located at $\sigma 2^{1/6}$ in the unshifted case) is kept at a distance of $2^{1/6}$. This distance is hereafter referred to as D. Simulations were performed in the NPT ensemble as derived by Martyna et al. [84]. System thermal energy was held at $kT = 0.1$, pressure at $P = 2$, and host particle mass was fixed at $m = 10$ (in simulation units).

In all cases discussed, the interstitial was simulated as a collection ($N = 20$) of isotropic repulsive potentials (interacting via the same SWCA potential as the host particles). To produce
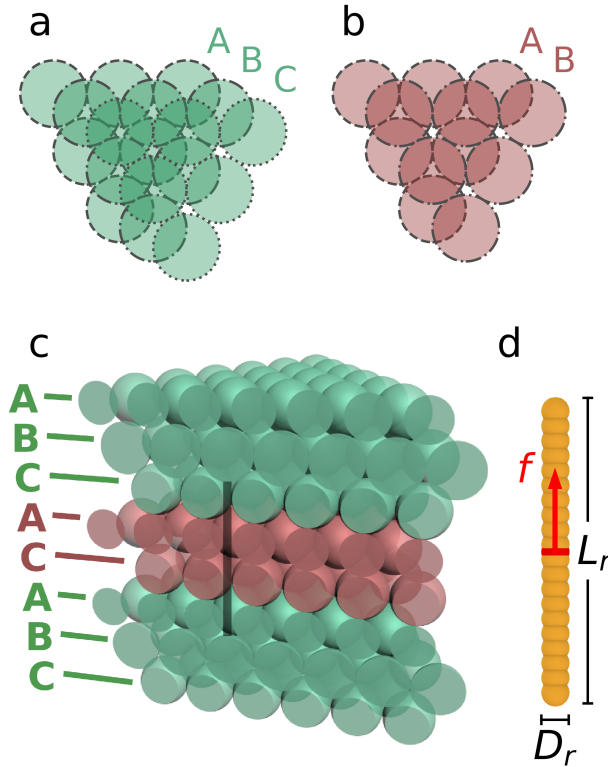
Figure 5.1: **a** Stacking sequence of dense planes in the FCC crystal. **a** Plane stacking sequence for the HCP crystal. **c** Cut-away rendering of a stacking fault with cylindrical void indicated by a shaded rectangle. **d** A rendering of the active interstitial geometry used in this study. The center of mass of the interstitial is indicated with a red line.

rods of different diameter the radial shifting of the SWCA potential was varied. Relative positions were maintained and torques handled during MD integration by rigid-body simulation [149]. The mass and moment of inertia of the interstitial was set so that the mass-density of the volumes enclosed by the zero isoenergy surfaces of the host and interstitial particles are equal.

5.4 Sampling Protocols

5.4.1 Interstitial Binding Protocol

To explore the interaction of active anisotropic particles with void spaces present near stacking faults in a thermalized, non-close packed crystal of SWCA particles, we prepared periodic

simulation domains ($N = 20,480$) with single stacking faults (using a layer shifting pattern of $3 \cdot [ABC] + BC + 3 \cdot [ABC]$). A single rod particle with axial force was added. By observing the position of the active particle relative to the stacking fault, a one-dimensional (the $[111]$ crystal direction) probability density function was sampled. In cases of strong particle-void interaction, a sharp peak in probability density was found near the stacking fault.

5.4.2 Active Walk Protocol

To investigate the mobility of active interstitials, we conducted MD simulations of individual active interstitials in defect-free crystalline domains with periodic boundaries ($N = 18,432$). The volume swept out by the trajectory of an active walk was computed using the open source software `vorlume` contained in the Structural Bioinformatics Library package [156]. The path of the active particle was decorated with spheres as the input to `vorlume`. Sphere centers were placed on the path at separations no larger than one eight of their diameter (interpolated as needed) to approximate a cylindrical swept volume.

5.4.3 Dislocation Interaction with Active Interstitial Protocol

Dislocation line arrays were created by subtraction of a half plane of particles in a periodic simulation box ($N = 502,500$) spanning 60 unit cell lengths in the x direction (aligned with crystal direction $[1\bar{1}0]$), 15 unit cell lengths in the y direction (aligned with crystal direction $[11\bar{2}]$), and 46 unit cell lengths in the z direction (aligned with crystal direction $[111]$). Active particles were introduced with directors perpendicular to dislocation glide planes. After sufficient time to allow the active particles to explore the simulation domain, a shear stress (σ_{xz}) was applied to the crystal, driving the dislocations to glide. System shear strain was computed from the simulation's box matrix [86].

5.5 Effective Interstitial Attraction to Stacking Faults

We find that active interstitials have a geometry-dependent effective attraction to stacking faults. To quantify this emergent attraction, we estimate a probability density function from observations of the interstitial-stacking fault separation (Fig. 5.2a shows an example of such a distribution). From this pair correlation function we obtain a potential of mean force [157], yielding an estimate of the interaction free energy of the interstitial with the stacking fault. Fig. 5.2b shows an example of such a free energy curve. Fig. 5.2c shows the estimated binding free energy well depth (E_B) for all rod geometries and driving forces explored in this study. Negative values of E_B indicate that the interstitial was found near the stacking fault less frequently than elsewhere in the simulation domain. We can also estimate the concentration of interstitials expected to accumulate near a stacking fault. We estimate the concentration enhancement (c_{SF}/c_0) from the probability per volume of observing the rod within a cutoff from the stacking fault (dashed line, Fig. 5.2a and b), normalized by the total volume of the simulation (Fig. 5.2d).

We find that the length of the interstitial is the critical parameter controlling the strength of effective attraction; interstitials with $L_r \approx 2D$ have the deepest free energy binding wells and highest concentration enhancements. Active force magnitude and interstitial diameter have significantly less effect on binding characteristics. Interstitial lengths longer than $2D$ tend not to be effective at binding to stacking fault voids. This is in part due to the slow rotational dynamics of long rods in crowded environments; some long rod geometries failed to align with the voids present near the stacking fault.

5.6 Considering the Path of an Active Interstitial as a Search

Beyond binding, we can ask the question, 'is the active walk of an interstitial an efficient search pattern for the target site (i.e. stacking fault) of interest?' To address this question, we first analyze the statistics of the active interstitial's trajectory through the host crystal in the absence of defects. The question of which form of run-and-tumble active walk is most effective for locating a target has
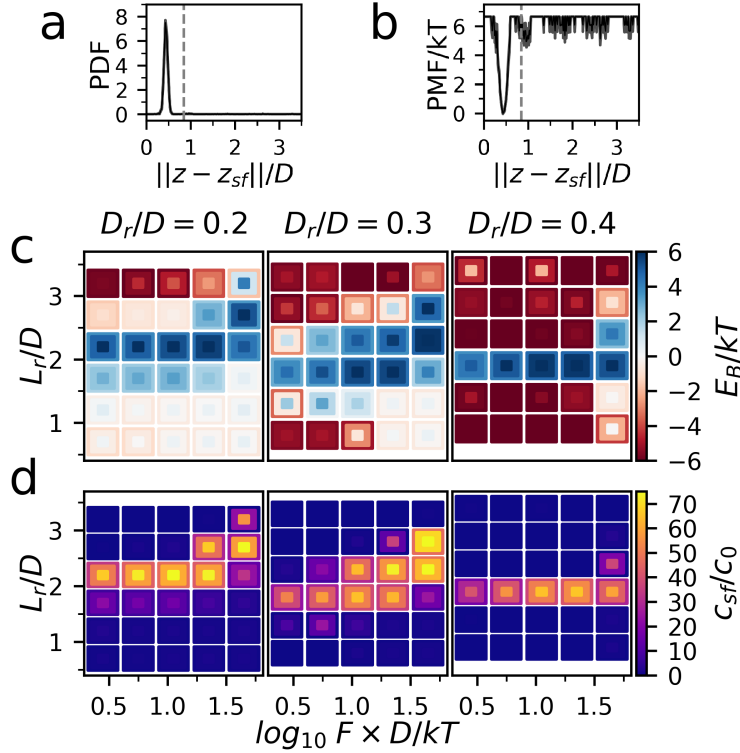
Figure 5.2: **a** A typical probability distribution of the active interstitial's position relative to the stacking fault center. The dashed line indicates the cutoff used to define interstitial-stacking fault contact. **b** Estimate of interaction free energy obtained from sampled probability distribution. **c** Binding free energy well depth for interstitials of various parameters. Each pixel represents both mean value and error: the centermost ring is the mean value of localization, the middle and outer rings are +/- one standard deviation. Force is non-dimensionalized by host particle diameter (D) and system thermal energy (kT). **d** Concentration enhancement for interstitials of different parameters.

been addressed at length, particularly in reference to the search patterns of animals [158, 159, 160, 161], but also in relation to general classes of search problems [162]. Rupprecht et al. analyzed the mean first passage time in a model system and found that the statistics of run lengths affects searching efficiency [163]. They found that the optimal run length depends upon the distribution of targets, with dense target environments favoring a Gaussian distribution and sparse environments favoring long-tail distributions. Furthermore, optimal run length also depends upon the boundary conditions of the domain considered, and the domain size.

The distribution of stacking faults due to dissociated dislocations will depend upon the size of the crystal domain in question, since dislocations have long-range strain field interactions. Gener-
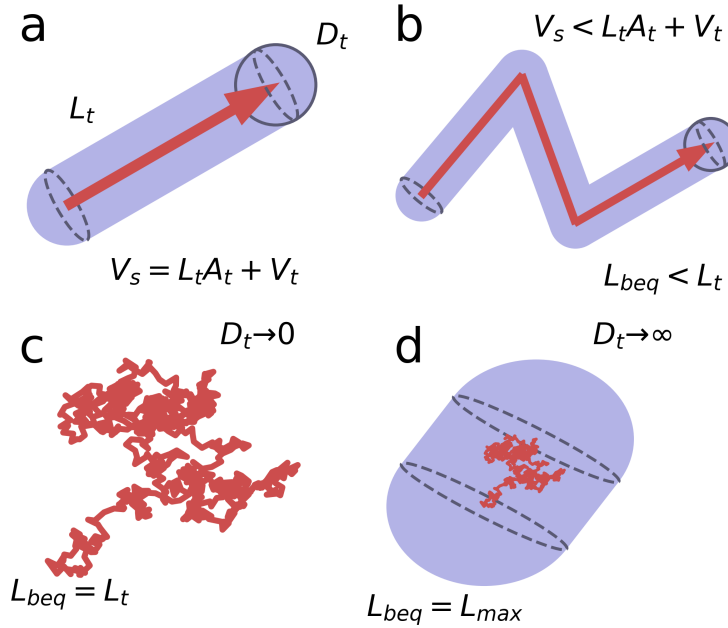
Figure 5.3: **a** The volume (blue) swept out by a ballistic walk (red). **b** The volume swept out by a run-and-tumble walk. **c** A walk with many steps decorated with infinitesimal D_t. **d** A walk with many steps decorated with very large D_t.

ally, experiments of colloidal crystals do not exceed centimeters in scale ($\approx 10^4$ to $\approx 10^5$ sub-μm particles). In dislocation terms, this is a small domain, and so a small number of dislocations should be expected in samples of reasonable quality. We expect, therefore, that active walks with long-tailed distributions of run lengths should be the best performers. When considering experimental systems we usually imagine a colloidal crystal domain with open boundaries, in which case searchers that encounter the boundary will be lost (either by leaving the crystalline domain, or becoming trapped on the boundary). Therefore we desire active walks that have a high probability of encountering a stacking fault before they are lost from the system boundaries. Another way to state this goal is to say we want a space filling walk; a walk that travels long distances slowly but samples large volumes without repetition.

We envision the active walk of an interstitial as a swept volume, where the sweeping diameter (D_t) is twice the walker-target collision distance. In this study we treat the walker as a point object, and consider the effect of target size. Consider a purely ballistic walk (Fig. 5.3a). In such a walk, the swept volume is simply related to the total length of the walk (L_t) and the cross-sectional area

(A_t) and volume (V_t) of sweeping. The total swept volume of the spherical interaction area can be described as $V_s = L_t A_t + V_t$. We refer to a walk described by this equation as 'ballistic'. Were we to calculate the ballistic length of a walk that was not actually ballistic, we would find that this equivalent length (L_{beq}) is less than the total length of the interstitial's trajectory (Fig. 5.3b). The degree to which $L_{beq} \neq L_t$ depends upon the diameter of the walk. For infinitesimal values of walk diameter, $L_{beq} = L_t$ regardless of the number of bends in the walk (Fig. 5.3c); for very large values of D_t, L_{beq} will be equal to the largest distance of the walk (Fig. 5.3d). For simulated walks, we generally find that L_{beq} as a function of D_t begins at a high value, and transitions to a low value at a specific D^* that depends upon the geometry of the walk. Consequently, the quantity $-\partial L_{beq}/\partial D_t$ is singly peaked. The location and height of this peak supplies information about the space-filling properties of the walk geometry. Significantly below D^*, the active walk has few self overlaps, and so the space sampled by the interstitial is almost entirely new. Above D^*, there are significant overlaps between segments, and so much of the space is sampled multiple times. When $D_t = D^*$, the walk is most nearly space-filling. The peak magnitude indicates how nearly space-filling the walk is. A large derivative indicates that large lengths of path are at a distance of D^* from each other. These geometric measures of space filling performance are also functions of time. After a sufficiently long time all walks (of finite-sized searchers) that are not strictly ballistic will become diffusive, since the walker will eventually re-sample previously visited space. We propose that for desirable active walks the peak in $-\partial L_{beq}/\partial D_t$ should be centered on the target size of interest, and the roughness should evolve slowly in time so that the walk remains an efficient space filling search over the timescale of interest. Therefore, when evaluating active walks we consider the time averaged value of $-\partial L_{beq}/\partial D_t$, denoted as $\langle -\partial L_{beq}/\partial D_t \rangle_t$.

5.7 L_{beq} as a Function of Interstitial Parameters

We investigated the space-filling properties of active interstitial walks by analyzing the L_{beq} value of interstitials with various $[f, L_r, D_r]$ parameters. Fig. 5.4 shows three examples of active walks.
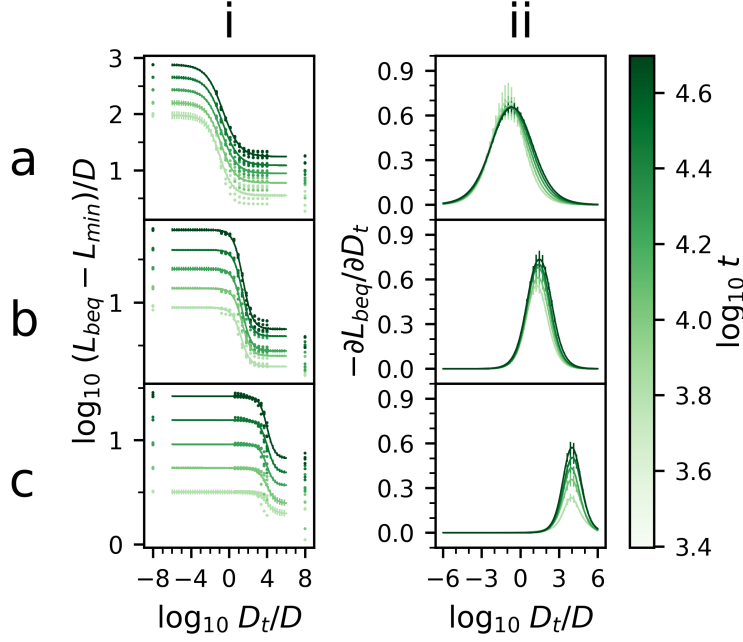
Figure 5.4: L_{beq} (**column i**) and $-\partial L_{beq}/\partial D_t$ (**column ii**) for example active walks. **row a** A diffusive walk. **row b** A rough walk. **row c** A ballistic walk.

Column (i) shows the value of L_{beq} for diffusive (a), rough (b), and ballistic (c) walks. Shown data points are sampled from replicates of each walk. Asymptotic values (Shown here at $\log_{10} D_t/D = -8$ and $+8$) are calculated from the total path length and largest distance in the trajectory point cloud, respectively. We fit the data to a logistic function of the form:

$$\log_{10} L_{beq} = \frac{\log_{10} L_i - \log_{10} L_f}{1 - e^{k(\log_{10} D_t - \log_{10} D^*)}} + \log_{10} L_f \tag{5.1}$$

where L_i is the total path length, L_f is the largest point cloud distance, D^* is the transition target diameter, and k is the steepness of the transition. Fig 5.4 column (ii) shows the value $-\partial L_{beq}/\partial D_t$. We find that the transition from diffusive to ballistic is clearly captured in the location of the L_{beq} transition point. As an active interstitial walk becomes more ballistic, the target diameter for which the walk most nearly fills space increases. Ballistic (diffusive) walks are best for very large (small) target sizes. Rough walks are intermediate between the two.

Fig. 5.5 shows the value $-\langle \partial L_{beq}/\partial D_t \rangle_t$ evaluated at different values of D_t. We find that walks are most capable of filling space for interstitial lengths less than $2D$. This finding is in direct
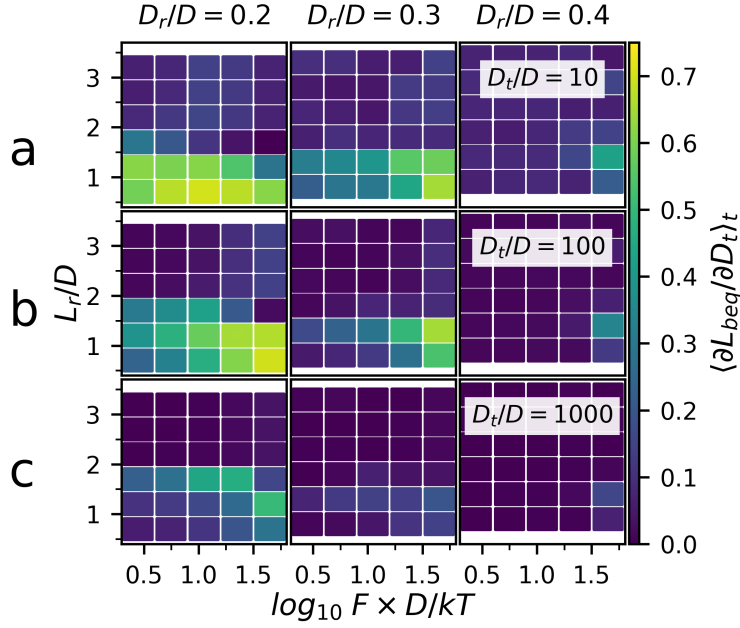
Figure 5.5: Time averaged derivative of L_{beq} evaluated for different values of D_t for all active interstitial parameters. **a** $D_t = 10$. **b** $D_t = 100$. **c** $D_t = 1000$. Error is represented the same as in Fig. 5.2, however these errors are small.

opposition to the trends of strong binding to stacking faults reported in section 5.5, where the largest effective stacking fault-interstitial attractions were found to be for rods of length $2D$. The ability of an active interstitial to search space depends upon a low barrier to reorientation; however, a low barrier to reorientation also permits the interstitial to escape from the void present near the stacking fault. As a result, the binding and mobility of active interstitials must be balanced against each other in a compromise between these two effects.

5.8 Reorientation Probability Controls Walk Roughness

Beyond the path traced by the active interstitial rod during the walk, (Fig. 5.6(i)), we can also investigate the orientation of the active interstitial relative to high-symmetry crystal directions. Fig. 5.6a(i) shows the volume swept out by an active interstitial that migrates diffusively. Points along the walk are colored by the nearest high symmetry crystal direction towards which the interstitial's long axis was pointed. Fig. 5.6a(ii) shows a polar projection of these directors mapped
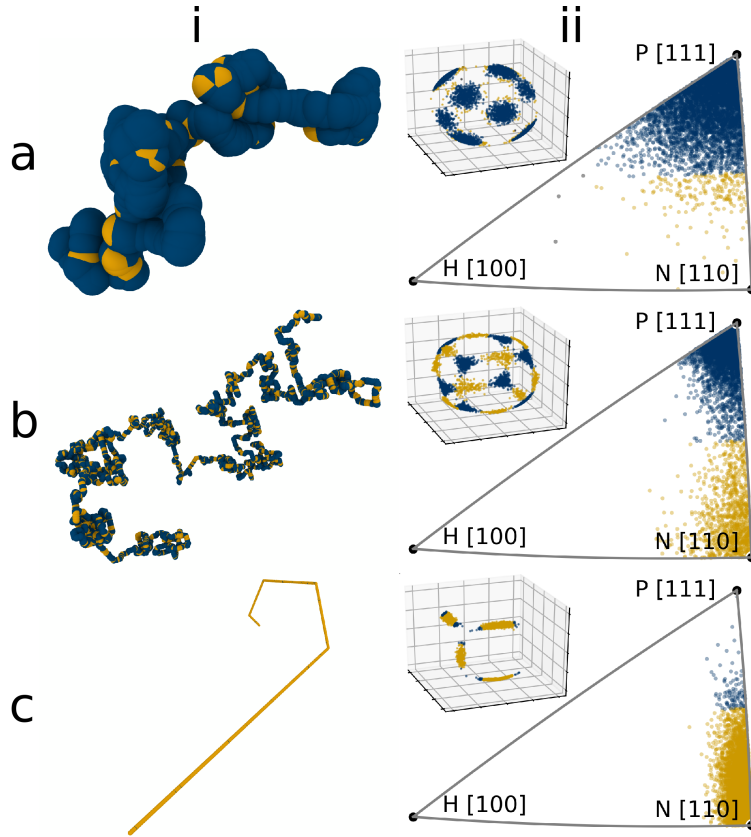
Figure 5.6: **column i** Renderings of volume swept by active walks (using `Ovito` [117]). Points along the walk are colored by the high symmetry crystal direction that the active interstitial's director is most closely pointing towards. **column ii** Directors of the interstitial as it performs the active walk, mapped onto the irreducible symmetry zone of the FCC structure. Insets show the un-reduced cloud of directors. **row a** A diffusive walk. **row b** A rough walk. **row c** A ballistic walk.

onto the irreducible rotational zone of the FCC crystal. The inset shows the un-reduced director cloud. Fig. 5.6c(i)-c(ii) and d(i)-d(ii) show the same information for a 'rough' and ballistic walk, respectively.

We find that diffusive, rough, and ballistic walks all have distinct orientational signatures. Interstitials with diffusive behavior tend to remain aligned with the [111] family of directions (which we denote as $P_{[111]}$). In the close-packed FCC structure, cylindrical voids of length $(\sqrt{6} - 1)D \approx 1.45D$ aligned with $P_{[111]}$ exist. Diffusive interstitials are trapped within these isolated voids, and so are unable to cover significant distances. In contrast, ballistic walks tend to remain aligned with the $N_{[110]}$ family of directions. Close packed sphere FCC crystals have small diameter channels

aligned with these directions that extend indefinitely. Ballistic interstitials have a high barrier to reorientation, and we find that $N_{[110]}$ channels are preferred over $P_{[111]}$ channels, but transitioning between members of the $N_{[110]}$ family is difficult. Rough walks occupy both families of directions. These interstitials are able to explore many orientations because there is a relatively small barrier to switching between the $P_{[111]}$ and $N_{[110]}$ directions.

Ultimately, we find that the ability of a rod-like active interstitial to reorient controls both the binding to stacking fault voids and the mobility characteristics. The ability of the interstitial to rotate can be shown to be primarily dependent upon the end-to-end length of the particle. Fig. 5.7a shows the free energy of interstitials aligned with the $P_{[111]}$ direction in a defect-free crystal, as estimated by the probability of observing that state. There is a clear transition from low to high energy at $L_r \approx 1.5 \, D$. The $P_{[111]}$ family of directions in an FCC crystal coincide with cylindrical voids of length $\sqrt{3}a - D$, with a the lattice constant. For the state point studied here, $a \approx 1.04\sqrt{2}D$, and so these voids have average length $1.55 \, D$. Figure 5.7a shows interstitials of this length have a free energy penalty of $2 - 3 \, kT$ when occupying these voids. Comparing this to Figure 5.2c and d, we can see that strong binding and interstitial concentration occur at lengths slightly larger than this. This suggests that strong confinement in the stacking fault voids, which are of length $5\sqrt{3}a/3 - D \approx 3.25 \, D$, occurs when the P family channels in the bulk are unfavorable enough to be rarely observed, but no so unfavorable as to be totally inaccessible.

By plotting the best fit value of D^* (Fig. 5.7b) for the rod geometries studied here we can see that the length scale of active walk roughness is maximum for rod lengths just longer than the transition from low to high $P_{[111]}$ free energy ($L_r > 1.5 \, D$). The $P_{[111]}$ channels that are present in FCC are wider in average diameter than the $N_{[110]}$ channels ($\sim 0.15 \, D$ and $\sim 0.07 \, D$, respectively). Therefore when the total interstitial length is short enough to fit within the $P_{[111]}$ channels, they are significantly better sites than the $N_{[110]}$ channels. However these channels are of limited length, and so interstitials strongly bound to them tend to become caged. Interstitials significantly longer than the $P_{[111]}$ family voids are trapped entirely in the $N_{[110]}$ family channels, and are therefore able to travel in long ballistic paths but have difficulty reorienting. When interstitial length is matched
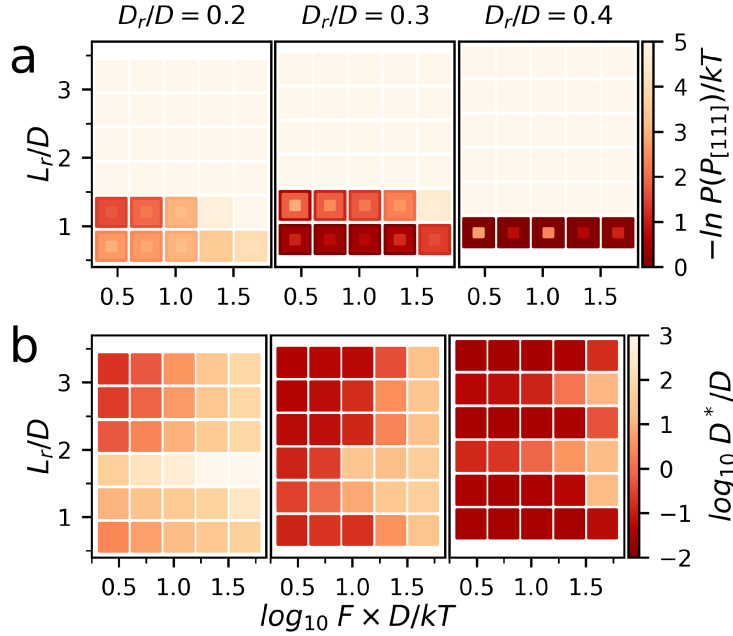
Figure 5.7: **a** Estimate of the free energy of the $P_{[111]}$ state for interstitials in this study. Error is represented as in Fig. 5.2. **b** The best-fit value of the inflection point of the transition from ballistic to diffusive behavior (D^*).

to the $P_{[111]}$ family void length these voids act as transition barriers between $N_{[110]}$ family channels. Adjustments to the length of the interstitial therefore change the energy barrier for reorientation. This barrier sets the statistics of the active walk by controlling the probability of 'tumbling' between $N_{[110]}$ channels. These results suggest that more complex interstitial geometries engineered to control rotational dynamics may be able to outperform the simple rods studied here.

5.9   A Combined Metric to Identify Optimal Interstitial Parameters

If we consider a ballistic interstitial searching for targets of disk-like shape, then such a particle with travel length L_t will possibly encounter up to L_t/L_0 disks, where L_0 is the width of one disk. We estimate this width as twice the distance between the stacking fault center and the interstitial binding well (dashed line, Fig. 5.2a). The ballistic path swept out can be written as $V_s = A_t L_t + V_t$, $L_t = (V_s - V_t)/A_t$ (which is the same expression used for defining L_{beq} when the path is not strictly

ballistic). Therefore, we estimate the total number of target disks that could be encountered as L_{beq}/L_0. Absorbing onto these disks will accrue a free energy benefit of E_B each. Therefore we can say that a particular walk has a free energy 'potential' of $E_t = E_B L_{beq}/L_0$. This expression represents the maximum binding free energy that can be released over the course of a walk; it is a way to assign an energy value to the distance that a walker covers. Since E_B and L_0 are independent of target size, we see that $\partial E_t/\partial D_t = (\partial L_{beq}/\partial D_t)E_B/L_0$. We can combine the negative time average of this metric with the concentration enhancement factor (see section 5.5) to yield a final overall fitness score:

$$S = \frac{E_B}{L_0}\frac{c}{c_0}\langle-\frac{\partial L_{beq}}{\partial D_t}\rangle_t \qquad (5.2)$$

The result of this combined metric, evaluated at different values of D_t, is shown in Fig. 5.8. The best performing active interstitial parameters are those that are on the edge between the strongly binding (or concentrating) shapes and the highly mobile shapes. Especially for large target sizes, a small number of optimal parameter combinations appear.

5.10 Test Case: Pinning Dislocations to Inhibit Shear Deformation

We investigated the effect of stacking-fault attracted active interstitials on dislocation mobility by simulating crystalline domains with a single dislocation dipole under shear. Using a geometry with high combined S value ($f = 11.2\,D/kT$, $L_r = 1.8\,D$, and $D_r = 0.3\,D$), active rods were introduced to the dislocation-containing crystal and allowed to walk. Subsequently, we applied a shear force and monitored the shear strain of the simulation domain. Fig. 5.9 shows the process of dislocation pinning and shear-induced depinning. Initially, dispersed interstitials (Fig. 5.9a(i)) search the simulation box and accumulate on the stacking faults that link the partial edge dislocations (Fig. 5.9b(i)). At sufficient shear stress (σ_{xz}) the dislocation moves past these pinning particles,
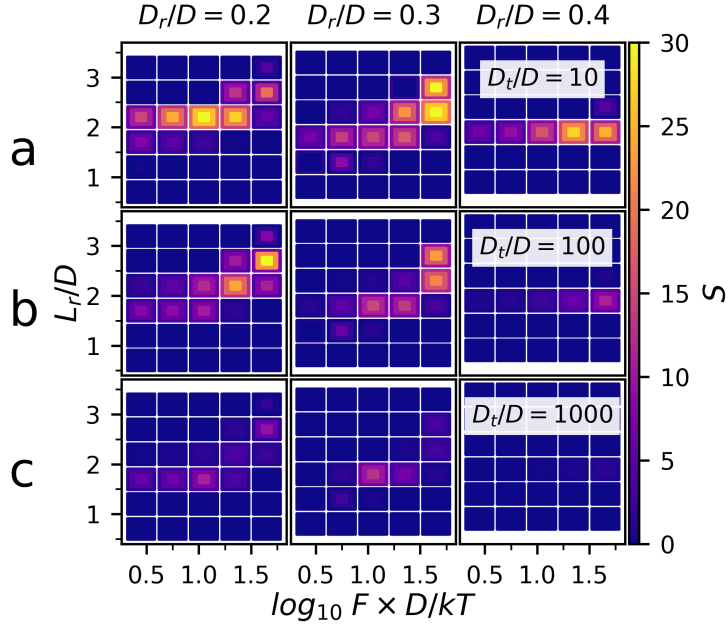
Figure 5.8: Combined metric of interstitial performance (S) for all active interstitial parameters, evaluated at different values of D_t. **a** $D_t = 10$. **b** $D_t = 100$. **c** $D_t = 1000$. Error is represented the same as in Fig. 5.2.

ejecting them (Fig. 5.9c(i)). When mobile, dislocations reach a terminal glide speed that is a function of the active interstitial concentration. Active interstitials with high S values are capable of traveling rapidly enough to re-acquire slow moving dislocations, and so a persistent interstitial drag atmosphere is established (Fig. 5.9d(i)). Fig. 5.9ii shows a histogram of active interstitial positions throughout the pinning and depinning process. We find that active interstitials tend to accumulate into the regions under compressive strain (due to the dislocation array). This is likely due to the larger drag experienced by active interstitials in compressed crystalline environments [80].

By tracking the shear of the simulation box, the shear rate ($\dot{\eta}_{xz}$) can be measured for different values of σ_{xz}. In the case of no active interstitials, the domain deforms at a rate that is best fit by a quadratic function of applied shear stress. The intercept of this fit (Fig 5.10a, darkest curve) is zero to within measurement error. A presumably small initial barrier to dislocation glide exists in such systems; however this value is not resolvable under the conditions used here. We find that the addition of even 32 active interstitials changes this shear rate behavior from quadratic to thresholded linear. We fit the data by curves of functional form:
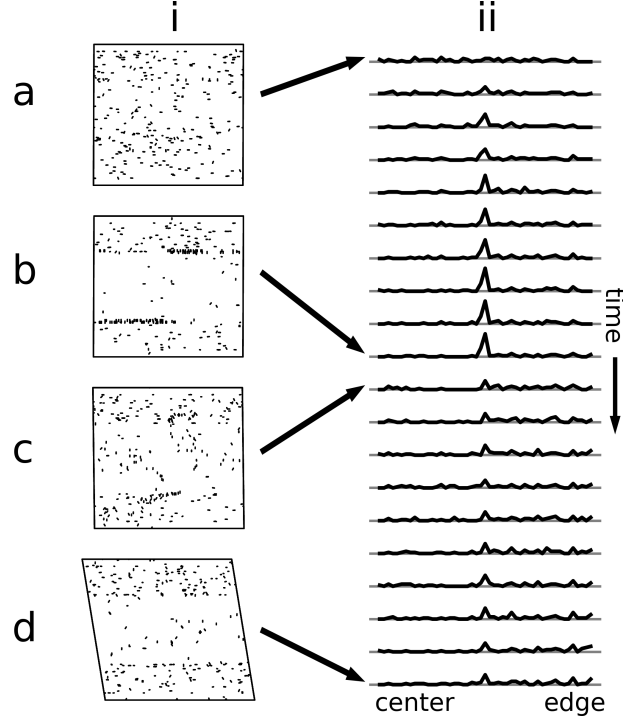
Figure 5.9: Time evolution of an $N = 502,500$ particle system with two dissociated edge dislocations and 256 active interstitials (with parameters $f = 11.2\,D/kT$, $L_r = 1.8\,D$, and $D_r = 0.3\,D$). **column i** snapshots of the active interstitials in the simulation box, looking along the $[11\bar{2}]$ crystal direction. Host particles are not shown. **column ii** Histogram of active interstitial z position over the course of a shearing simulation. This histogram ranges from the box center to box edge. **a** Before interstitials have had time to encounter the partial dislocations. **b** Immediately before dislocation depinning. The interstitials are most concentrated in the glide planes. **c** De-pinning in progress. Clouds of interstitials leaving the glide plane are visible. **d** After several transits of depinned dislocations across the box. There remains a small concentration of active interstitials in the glide plane. Active interstitials have been depleted from the central region (under local tension) and accumulated in the edge regions (under local compression).

$$\dot{\eta}_{xy} = max(0, \kappa|\sigma_{xy} - \sigma_{xy}^d|^{\alpha}) \tag{5.3}$$

where σ_{xy}^d is the shear threshold and κ is the shear rate. As the number of interstitials is further increased, the fit value of σ_{xy}^d shifts to higher shear stress, and α decreases below one. Fig. 5.10b shows the depinning stress as a function of interstitial number. Fig. 5.10c shows the change in shear rate (κ) with shear stress as a function of interstitial number. As more active interstitials are added, they not only increase the threshold of stress needed to de-pin dislocations, but also apply
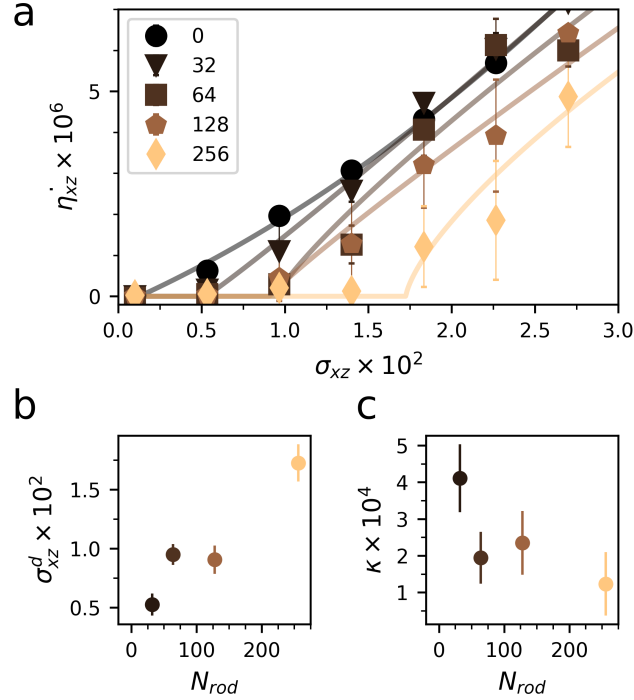
Figure 5.10: Quantitative trends in shearing resistance with active interstitial number. Active interstitials have parameters $f = 11.2\,D/kT$, $L_r = 1.8\,D$, and $D_r = 0.3\,D$. **a** Shear rate as a function of shear stress. **b** The depinning shear stress as a function of interstitial number. **c** The slope of the shear rate vs. shear stress curve as a function of interstitial number.

an additional drag to dislocation motion that persists after depinning. The mechanism for this drag is subsequent re-acquisition of the moving stacking fault by active interstitial particles.

5.11 Active vs. Passive Dislocation Pinning

We have shown that stacking faults in crystals comprised of isotropically repulsive particles contain special voids that are favorable sites for rod-like interstitial particles to bind to. When the stacking fault is associated with a partial dislocation, the migration of the dislocation core must be accompanied by the reconfiguration of this void, and therefore the ejection of the interstitial. This ejection imposes a penalty on the shear force required to drive such dislocations into glide. When these interstitial particles are active, they are capable of rapidly covering large distances in search of stacking faults.

This interaction of active interstitials and dislocations is interesting as an elaboration of the concept of a Cotrell atmosphere [153]. A Cottrell atmosphere is when interstitials collect around a dislocation core, effectively pinning its motion. In atomic systems, interstitials are attracted to the dislocation because of the strain fields of both objects. It is also possible for interstitials to have strong pinning interactions with the cores of dislocations [164, 165].

Atomic dislocation-interstitial interactions have strong shear rate dependence [153, 154, 67, 155] due to fundamental limitations of interstitial mobility. Interstitials that interact strongly with the strained dislocation environment tend to also be slow diffusers, and so cannot quickly concentrate near or follow a moving dislocation. Small interstitials that interact strongly with dislocation cores may be faster diffusers, however the core is a comparatively small region. Therefore the probability of core-interstitial interaction depends heavily on the concentration of the solute species [165].

We find that active, rod-like interstitials avoid these problems by affecting greater decoupling between mobility and attraction to dislocations. The active force allows such interstitials to cover large volumes compared to their passive counterparts. Furthermore active interstitials interact with stacking faults (not the dislocation core), which are extended defects. This significantly improves the chance of interstitial-dislocation interception. Our results show that active interstitials result in damped dislocation dynamics at shear rates much higher and concentrations lower than that at which passive interstitials would be effective.

5.12 Conclusion

We showed that rod-like active interstitials can interfere with dislocation motion at number concentrations as low as 64 particles per million host particles. This interference produces a shear stress threshold that was negligible without interstitials. The physics behind the mechanism of binding and searching are antagonistic, so a compromise must be found for interstitial designs that strongly impact material plasticity. We propose a combined metric to determine active interstitials with de-

sirable properties. We find that the length of the rod-like interstitial is the dominant parameter for

adjusting the rotational transition probability as well as binding preference in FCC crystals.

Engineering Dislocation Pair Creation to Reconfigure Colloidal Matter

This chapter and its figures are adapted from an as-yet-unpublished manuscript (Ref [82]) authored in 2019 by Bryan VanSaders and Sharon C. Glotzer.

6.1 Metamaterial Reconfiguration

With sufficient miniaturization it is possible to create materials which at the human length scale appear continuous, but are in fact composed of discrete subunits that have been engineered. When the subunits are small and relatively simple such materials are often referred to as 'metamaterials'. As an example, the manipulation of optical material properties by engineering the response of so-called 'meta atoms' has seen significant success [99, 166].

When the complexity of the subunit is increased to the point where each 'module' has some combination of independent sensing, actuation, self-propulsion and communication capacity, then the material is described as a modular robot [167]. Many forms of reconfigurable modular robots have been proposed and prototyped. A subset of studies frame the aggregate collection of robotic modules as a new material type. Lattice robots [168, 169, 170], 'programmable matter' [171], the 'slimebot' [172] and the 'particle robot' [152] are examples of this school of thought. While simulations of modular robots have advanced to the point of the material scale [173, 174, 175], practical realization of more than 100 robotic modules remains challenging (with the notable exception of

Rubenstein et al. [176]). The demanding requirements of self-propulsion, communication, and sensing necessitate macro-scale robotic modules with prohibitive complexity and cost.

Metamaterials and programmable matter, while conceptually linked, are separated by several orders of magnitude in their subunit cost and functionality. In the last several decades, chemists have advanced techniques that permit sub-micron particles to perform work locally, increasing the functions available to very small subunits. For the first time, it is feasible to consider a continuum-scale material composed of devices (active particles) that locally perform work in a designed way. Swarms of self-propelled colloids can be controlled with a global field, such as light intensity [36], chemical signaling [177], or a rotating magnetic field [37, 38, 39, 40, 41]. The behavior of such non-equilibrium colloidal swarms relies heavily on emergent phenomena to take the place of integrated communication and control often present in macro-scale robotic swarms.
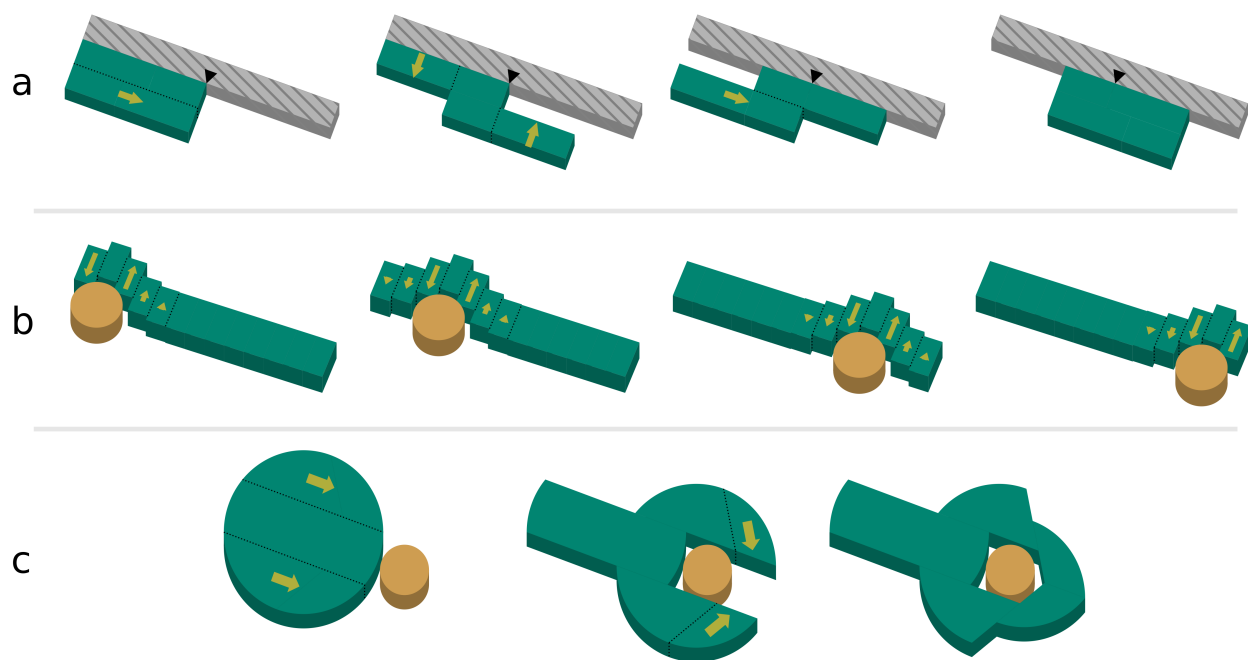
Figure 6.1: Schematic representations of functional operations performed by selective shearing. A crystalline colloidal robot (green) reconfigures itself by shearing along selective planes (dashed lines). Yellow arrows represent planned displacements. **a** Locomotion via shearing for a colloidal robot in contact with a wall (gray, hashed). By shearing on multiple planes the robot is 'rolled' along the wall. **b** Peristaltic transport of an object (yellow cylinder) by a colloidal robot via shearing operations. By sequential activation and reversal of shearing planes, the cargo is transported along the robot. **c** Cargo (brown cylinder) capture via shearing operations.

A fundamental task of a modular robot is to reconfigure its shape. Many tasks of interest rely on shape change: moving cargo, crawling past obstacles, engulfing cargo, etc. When the number of subunits is small and subunit complexity is high, algorithmic planning can achieve near optimal reconfiguration characteristics. For colloidal-scale metamaterials composed of many thousands or millions of individual subunits, with no ability to locally communicate or plan, another approach is needed. Shape change on this scale might be better thought of as a controlled plastic deformation. In systems composed of isotropically interacting subunits (such as spherical colloidal crystals, or atomic metals), plastic deformation is controlled by the production and migration of defects known as dislocations [73, 70]. The creation and control of 2D dislocations via optical fields has been reported in colloidal systems[72, 74].

6.2   Dislocations as Shape Reconfiguration Tools

If it were possible to selectively induce shear along arbitrary slip planes in a crystallite, then a wide range of surface and interior reconfigurations are possible. Fig. 6.1 outlines three cases where the ability to shear along arbitrary planes allows for a useful task to be carried out. Fig 6.1a,b, and c show how bulk locomotion, cargo transport, and cargo capture could be achieved using only shear displacements in a colloidal crystallite robot.

Within a crystalline material, non-elastic shear displacement is the result of the propagation of dislocations. Dislocations are the fundamental unit of shear slip in crystals undergoing plastic (i.e. irreversible) deformation. As a dislocation travels through a material, the regions on either side of the defect's glide plane are translated (slipped) relative to each other by an amount given by the dislocation's Burgers vector. The creation of a dislocation must conserve total Burgers vector (which must remain zero, if starting from a defect-free crystal). Therefore when dislocations are created, they appear in pairs. For a given glide plane in a 2D crystal, such dislocations can be either left or right handed, which we refer to as 'positive' and 'negative'. Positive dislocations are those that define the termination of an additional half plane of particles that extends into the positive

half space of the crystal ('above' the glide plane). Likewise, negative dislocations terminate the half plane that occupies the negative half space ('below' the glide plane). The Burgers vector of these two dislocations is opposite and equal, and if they are brought together they annihilate and a defect-free crystal results.

If a dislocation is migrated to a boundary of a crystal, such as exists at a free surface, then the termination of the half plane it bounds will appear on that surface. This eliminates the dislocation and its elastic deformation, leaving behind only the change to the surface. This change is a step, of height equal to the dislocation's Burgers vector. If dislocation pairs could be created and driven to the surface in a particular (arbitrary) pattern, then in theory any surface reorganization could be accomplished one Burgers vector at a time. This method of surface reshaping requires both a means to produce oriented dislocations as well as a means to direct them towards the free surface to be manipulated. Notably, if both the positive and negative dislocations from the created pair were directed to the same surface, then no permanent change in the crystallite boundary would be achieved because the second dislocation to arrive would reverse the effects of the first. Therefore to use dislocations as operations to sculpt surfaces we must have a means of separating them that is strong enough to overcome the attractive force driving recombination of the pair on the same glide plane.

In this paper we explore how quasi 2D crystallites of colloids can be re-shaped by the production and migration of dislocation defects. We present here a simplistic scheme of dislocation creation based on swelling the size of an anisotropically shaped subset of the crystallite's particles. We simulate a colloidal crystalline monolayer, such as might be prepared by sedimentation of colloidal spheres on a flat surface. A cluster of colloids with variable diameter (achieved via, e.g., heating or solvent swelling) is embedded in this monolayer. We show that global control over a single degree of freedom (the diameter of the particles in the embedded cluster) is sufficient to enact significant reorganization of the crystallite's boundary by the creation and emission of dislocations. These results are also applicable to certain classes of 'lattice robots', which operate at larger length scales [168, 169].

First, our system of study and its simulation protocols are introduced. We show several examples of reconfiguration in finite sized crystallites and bulk domains. We then describe the necessary features of an embedded cluster and the importance of anisotropy in dislocation emission. Finally, we end with a discussion of how this study relates to existing work on reconfiguration schemes for modular robots.
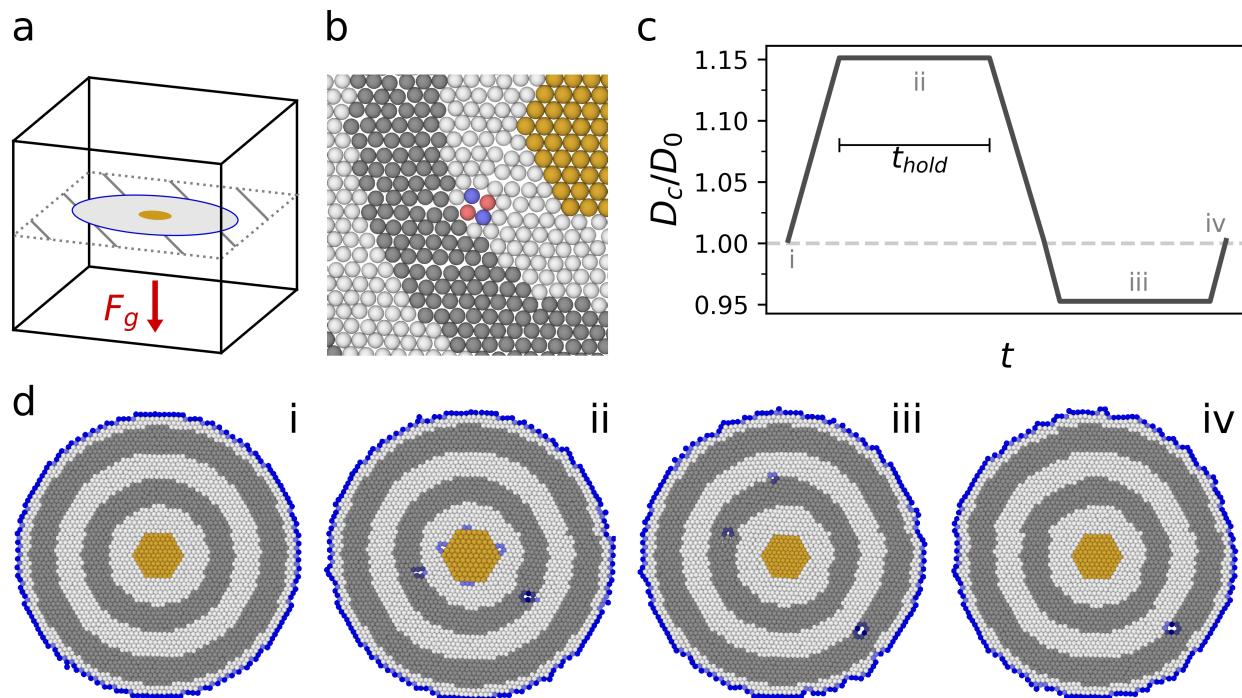
Figure 6.2: **a** Schematic diagram of simulation domain. A downward force (F_g) keeps a cluster of particles (gray oval) pinned to a repulsive plane (hatched). **b** The particle color scheme used throughout this study. Yellow indicates particles with variable diameter. Blue, white, and red colors indicate less than six, six, or greater than six neighbors. Dark gray coloration is added to some particles as an aid to the eye for noticing plastic deformation. All particles which are not yellow have fixed diameters. **c** An example diameter change profile. Beginning at the same diameter as all other particles (D_0), the yellow particles are increased in size via discrete changes at constant intervals then held for a time t_{hold}. The variable particles are then shrunk down past their original size to a minimum value, and again held for the same time t_{hold}. Finally, the particles return to their original diameter and one cycle is complete. Numeral labels refer to sub-panels of part **d**. **d** Snapshots of an example system undergoing one swell/shrink cycle. **i** The initial configuration, with all particles the same diameter. The variable particles held at their maximum diameter **ii**, minimum diameter **iii**, and returned to original diameter **iv**.

6.3   Model and Methods

Fig. 6.2 shows an example of the embedded cluster model used in this study. First, a quasi-2D crystallite is prepared. This crystallite is confined to a plane by a downward force and a repulsive force from a plane supporting it (Fig. 6.2a). This configuration mimics a sedimented colloidal layer (but neglects any effect of surface friction). Embedded clusters comprise a small subset of particles within the cluster held together via harmonic bonds. Bonding eliminates the possibility of cluster reconfigurations occurring upon successive swelling cycles. It also results in a cluster that behaves as a connected body, which may be appropriate for experimental realizations in which a cluster is pre-fabricated as a single object and then embedded into a colloidal monolayer.

All Molecular Dynamics (MD) simulations reported here were performed with HOOMD-blue [112, 113]. All particles interact through a shifted-Lennard-Jones potential (SLJ) [110], where the origin is shifted towards the surface of the particle. The value of σ used in this potential was set to 0.75, and the potential was shifted radially so that the minimum (located at $\sigma 2^{1/6}$ in the unshifted case) is at a distance of $D_0 = 2^{1/6}$. This distance is the minimum-energy isosurface of the pair potential, and is taken to represent the particle's physical surface. The depth of the attractive well was set to $\epsilon = 1$. Simulations were carried out via Langevin integration. System thermal energy was held at $kT/\epsilon = 0.22$, and particle mass was fixed at $m = 1$ (in simulation units). References in the text to energy, mass, time, and length scales will use these values for non-dimensionalization. System temperature and pair potential parameters where chosen so as to produce solid phase crystallites with realistic defect dynamics.

During a swelling or shrinking cycle, a subset of particles change their diameter by changing the radial shift applied to the pair potential in small discrete increments (relative to the average distance between particles). The value of ϵ and σ used in the pair potential is kept constant at all times. Tunable-diameter particles are harmonically bonded to tunable neighbors. The length of this harmonic bond is scaled along with the particle diameters during a simulation.

Throughout this study we employ a consistent color scheme for renders of particles (all renderings are conducted with OVITO [117]) (Fig. 6.2). Particles with tunable diameters are colored

yellow. All other particles are colored by their coordination number (CN). The pair correlation function $g(r)$ is computed for the entire system, and CN is determined by counting neighbors within a cutoff of $\frac{4}{3}D_0$ (approximately halfway between the first and second peaks in $g(r)$). Particles with fewer than six neighbors are colored blue, while those with more than six are colored red. Six-coordinated particles are colored light gray. Lastly, a subset of particles (chosen arbitrarily) are given a dark tint. This coloration creates a pattern on the crystallite which aids the eye in observing plastic deformation.

Fig. 6.2di-iv shows a swell/shrink cycle (Fig. 6.2c) for a hexagonal embedded cluster of particles within a small crystallite. The edges of the hexagon are aligned with glide planes. At maximum embedded particle swelling diameter, positive dislocations have been emitted into the crystallite (low-coordinated blue particles), while negative dislocations remain stuck to the cluster sides. At minimum embedded particle diameter, the negative dislocations also migrate away. After the cycle is complete, some defects remain. Additionally, plastic slip has occurred, as evidenced by changes to the ring coloration pattern on the crystallite.

To specifically target an individual slip plane, a cluster geometry different from that shown in Fig. 6.2 is required. Several forms of anisotropy are needed to produce dislocations on one plane only, and to repeatably bias their emission.

6.4 Shearing as a Unit Operation

The fundamental unit operation for a dislocation-emitting embedded cluster is to produce shear slip across a single adjacent glide plane. Fig. 6.3a shows the state of a crystallite ($N = 23,231$) with one embedded cluster after many swell/shrink cycles. As subsequent pairs of dislocations are produced and migrated to the edge of the crystallite, the domain is sheared in half. This shearing also produces a net torque on the crystallite, which rotates it. The handedness of this torque is opposite to the torque that would result if this crystallite was sheared by the application of surface forces.

A key consideration in the shearing operation is the distance of maximum separation of the dislocation pair. If this distance is smaller than the dimensions of the crystallite, then the dislocations may not reach the boundary. Dislocations that do not reach the boundary remain in the system, and may interfere with subsequent cycles. This can happen either through backwards migration (particularly the negative dislocation, which can be re-attracted to the cluster from long range) or by producing a 'back pressure' that resists additional dislocation pair creation. We find that backwards migration is a larger problem than back-pressure, as in a back-pressure situation subsequent cycles tend to create short-lived dislocation pairs that push the original pair farther away, eventually clearing defects from the vicinity of the cluster over several cycles.

A related failure mode that we observed is for several vacancies to condense around the cluster, rendering subsequent cycles ineffective in generating dislocation pairs. If the minimum diameter of the shrinking phase is too small, then cross slip events occur whereby the negative dislocation decomposes into vacancies that attach to the surface of the cluster. Such attached vacancies tended to 'poison' the cluster, preventing subsequent defect production. We were able to suppress this process by increasing the minimum size of the variable diameter particles. However below this size we observed farther migration of the negative dislocation during t_{hold}. We found that the forces driving dislocation migration away from the cluster also are a function of the cluster geometry (discussed below).

6.5 Combining Multiple Shearing Clusters

Multiple shearing clusters can be combined together to carry out more complex deformation operations in crystallites. Here we show two such kinds of compound operations. In this study, we did not introduce any phase delay between the swelling cycles of the embedded clusters. Such a delay could be exploited to improve the efficiency and stability of multiple-cluster schemes. However, here we show that complex material reconfiguration is possible even without phase delay.
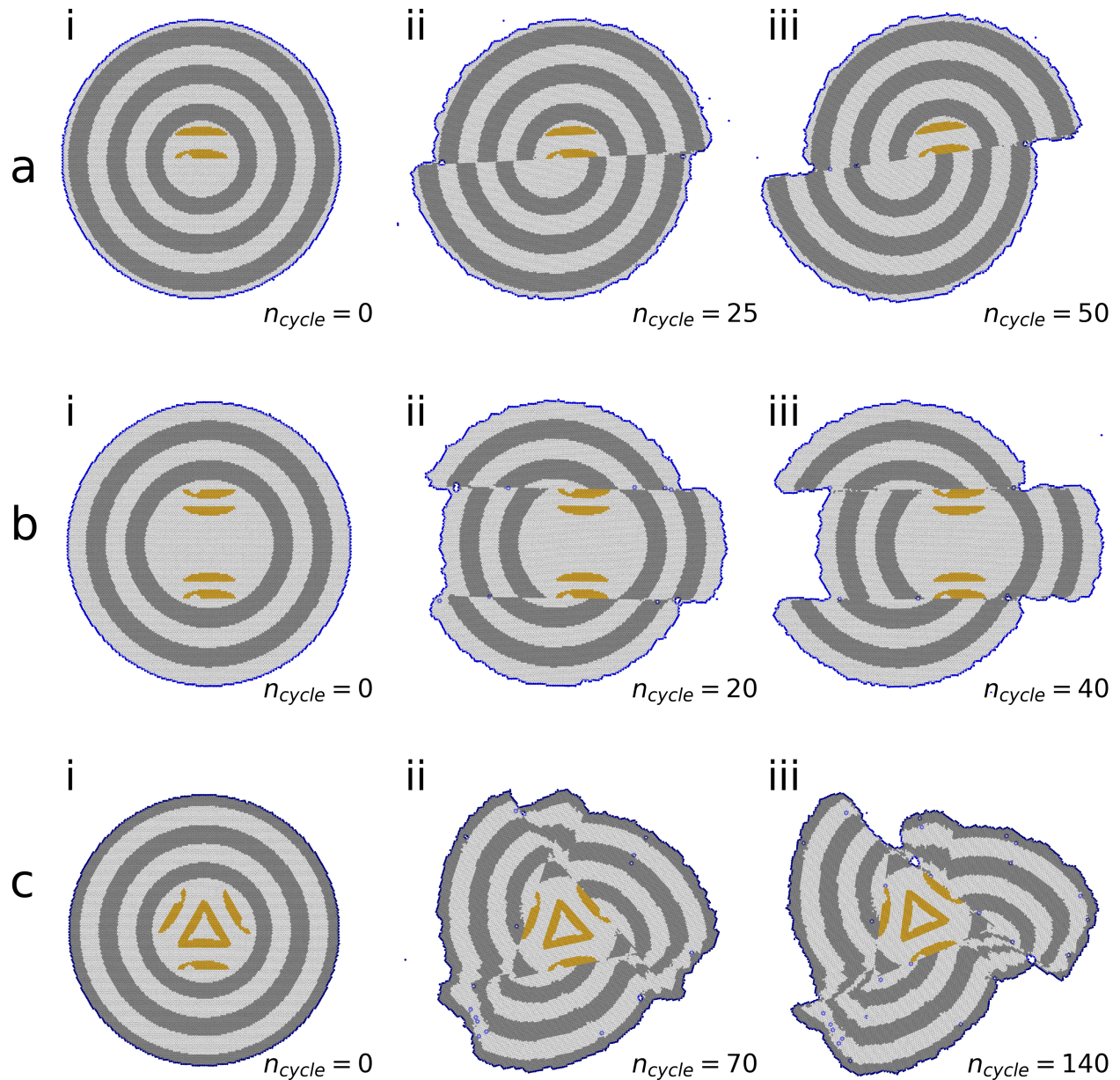
Figure 6.3: Cyclic operation of dislocation-producing clusters embedded in circular crystallites. Dark rings are guides to the eye for tracking plastic deformation. **a** A single embedded cluster, causing shear across one plane. Snapshots at 0 (i), 25 (ii), and 50 (iii) cycles. **b** Two embedded clusters slicing a crystallite. Snapshots at 0 (i), 20 (ii), and 40 (iii) cycles. **c** Three embedded clusters swirling a crystallite. Snapshots at 0 (i), 70 (ii), and 140 (iii) cycles.

Slicing   When two embedded shearing clusters are arranged so that their glide planes are parallel and opposite in sign, then the slab of material contained between those glide planes is slipped relative to the rest of the crystallite. We refer to this kind of operation as 'slicing'. Fig. 6.3b shows a slicing operation in a crystallite ($N = 23,321$) containing two embedded clusters. The even

slip produced by the top and bottom clusters indicates that they are operating in tandem, without cross-interference. If the two clusters are placed closer to each other, then cross-slip events can occur with multiple dislocations recombining. This configuration can be thought of as transporting wave after wave of extra planes to the crystallite edge, which grows a protrusion on one side while excavating a cavity on the other. Unlike in the shearing example above, there is minimal net rotation of the crystallite here, because the forces produced by shear are balanced.
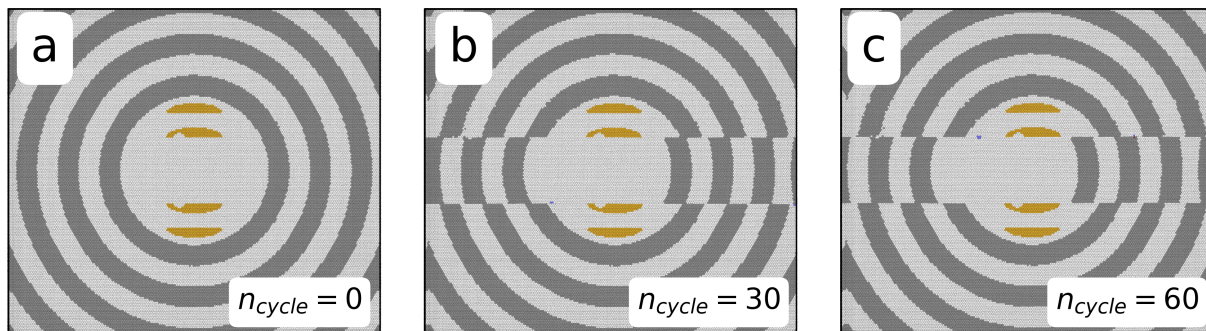
Figure 6.4: Cyclic operation of a pair of clusters embedded in a periodic domain. Clusters 'pass' dislocations to their images, resulting in a slip band. **a** The initial configuration, before any swell/shrink cycles. Dark rings are guides to the eye for tracking plastic deformations. **b** System configuration after 30 cycles. **c** System configuration after 60 cycles.

Swirling When the emission directions of multiple clusters in the same crystallite are arranged in a chiral manner (Fig. 6.3c), then a complex rotation of material in the crystallite can be accomplished. We term this operation a 'swirl'. The effect is to mix and translate sections of the crystallite past each other, resulting in a flower-like shape. Note that there is a net rotation of the crystallite, again in the opposite direction to that which would occur if this process were accomplished with surface forces. The efficiency of this operation is significantly lower than the other operations we have discussed. This is due to the tendency of clusters to suppress the splitting of other cluster's dislocation pairs, resulting in many cycles where only one side of the triangular arrangement succeeded in migrating its dislocation pair to the crystallite boundary. We hypothesize that this kind of interaction could be greatly reduced by introducing a phase offset between the cycles of the three sides of the triangle. Despite this tendency for cross-interference between

clusters, this example demonstrates that the biased pair production of the clusters is robust enough to produce the desired effect with a minimum of control.

6.6   Consecutive Clusters as Repeaters

In a small crystallite, the crystal surface acts as a sink for both positive and negative dislocations, capturing them and thereby permitting future cycles to release new dislocation pairs into un-distorted crystal regions.

Fig. 6.4 shows a slicing configuration of clusters embedded in a periodic crystalline domain ($N = 40,000$). In this case, dislocations traverse the periodic boundaries of the box and recombine on the opposite side of the cluster they were created on. This can also be thought of as clusters passing dislocations to their periodic images in adjacent periodic domains. The example shows that multiple clusters on the same glide plane act as 'repeaters', absorbing their neighbors' dislocations. A line of repeaters therefore should be able to transport dislocations over very long ranges. Note that because the line of repeaters is made of periodic images, there is no phase delay between the cycles of adjacent clusters. Much like the swirl demonstration above, we expect that introducing a phase delay could improve the operational robustness of a line of repeaters.

6.7   Design Heuristics for High-Performing Cluster Geometries

We now take a closer look at the geometry of clusters well suited to inducing shear displacement over many cycles. Good cluster performance depends on several metrics. First, the dislocations must be produced only on one glide plane. Once produced, the dislocation pair must be separated as far as possible, so that the dislocations can reach a surface or other recombination site. Lastly, the dislocation pair must be created and separated with the same polarity, i.e. the positive and negative dislocations should leave in the same direction on each cycle. We now examine the connection between cluster shape and performance through each of these three metrics.

6.8 Thresholds of Defect Creation

To study the onset of dislocation creation due to swelling or shrinking of an embedded cluster, simulations were performed with a rectangular cluster. The rectangular shape was chosen for simplicity of analysis. Expansion of the cluster sides due to isotropic swelling of the constituent particles produces shear stress that eventually results in the creation of a dislocation pair. For high-aspect ratio shapes, we can focus on the effect of length extension, $\Delta l/D_0$. Clusters were equilibrated, then shrunk or swelled to states that resulted in a prescribed change Δl of the longer dimension of the rectangular cluster. The local environment of particles was taken as the Voronoi polygon. Dislocation in 2D can be identified by a pair of 5 and 7-sided polygons in the Voronoi diagram of a crystal. For particles with six Voronoi neighbors a local affine strain can be calculated using the Voronoi polygon vertices [79]. Shown in fig. 6.5 are snapshots of the Voronoi diagrams for cluster expansions at interesting points. The expansion threshold for defect creation was found to be $\Delta l/D_0 \approx 2$, and $\Delta l/D_0 \approx 1.4$ for contraction. Fig. 6.6 shows defect number and strain field magnitude data for rectangular clusters subjected to isotropic particle swelling or shrinking.

Fig. 6.6a shows the number of defects ($N_{defects}$) observed for different states of cluster extension or contraction. A clear threshold in defect creation can be seen at an extension of $\Delta l/D_0 \approx 2$ and a contraction of $\Delta l/D_0 \approx -1.5$. For extension, only five (C_5) and seven (C_7) coordinated defects are created, which is consistent with the core of a dislocation. For contractions, other coordinations (C_4,C_8) are also found. The dislocation dipole that is emitted from a shrinking rectangle cluster represents a missing partial plane of particles. These types of dislocation dipoles (vacancy, or intrinsic, dipoles) are unstable in this system, and often decompose into immobile vacancy clusters, which is why more variety of defect coordinations are observed for cluster contraction. In contrast, during cluster swelling the emitted dislocations represent the extra plane of particles that must be ejected to make space. Such interstitial (or extrinsic) type dislocation dipoles are more likely to leave the vicinity of the expanding cluster, leaving behind a bound pair of complementary negative dislocations on the cluster surface.

Fig. 6.6b shows the value of the largest affine shear strain (η_{xy}) found around the rectangular
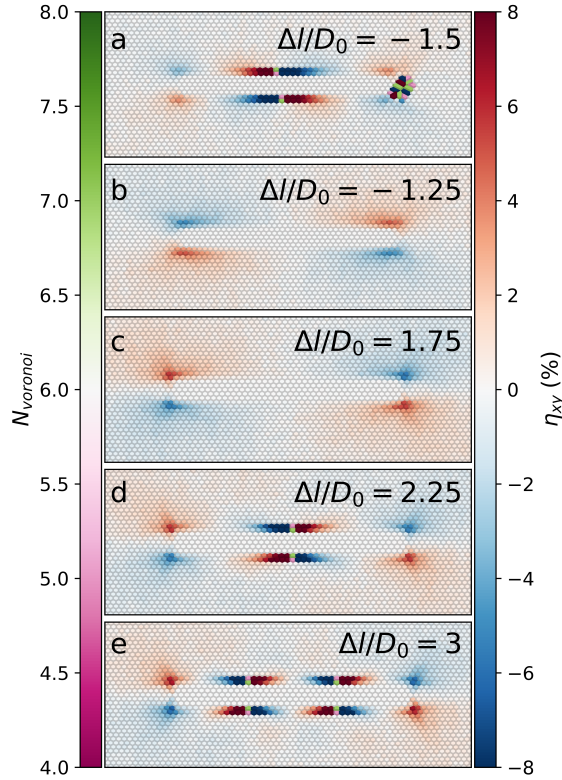
Figure 6.5: Voronoi diagrams for high aspect ratio rectangular embedded clusters at various strain states. 6-sided polygons are colored by the magnitude of the affine strain they represent. Polygons with other numbers of sides are colored by their side number. **a** Length change of $-1.5D_0$. Vacancy-type dislocation pairs are typically unstable, and decompose into a vacancy cluster as seen here. **b** Length change of $-1.25D_0$. Sub-threshold for vacancy-type pair creation. **c** Length change of $1.75D_0$. Sub-threshold for interstitial-type pair creation. **d** Length change of $2.25D_0$. One interstitial-type dislocation pair has been produced and driven off, leaving behind two bound dislocations. **e** Length change of $3D_0$. Two interstitial-type dislocation pair have been produced and driven off, leaving behind four bound dislocations.

cluster for various extensions and contractions. For extensions below the threshold, maximum shear strain scales in a mildly super-linear fashion. At the threshold extension, maximum shear values dramatically increase. For extensions, this increase is to the value of affine strain calculated near the core of a dislocation. For contractions, very large strain magnitudes are found due to the presence of highly distorted vacancy cluster environments. The behavior of the strain magnitudes below the yielding point indicates the cause of the extension/contraction asymmetry. For the pair potential used here, tension and compression have different material stiffnesses resulting from the fundamental asymmetry of the pair potential bonding well. Such strain asymmetry can be

manipulated through changing either the shape of the pair potential or the statepoint of the material [79].
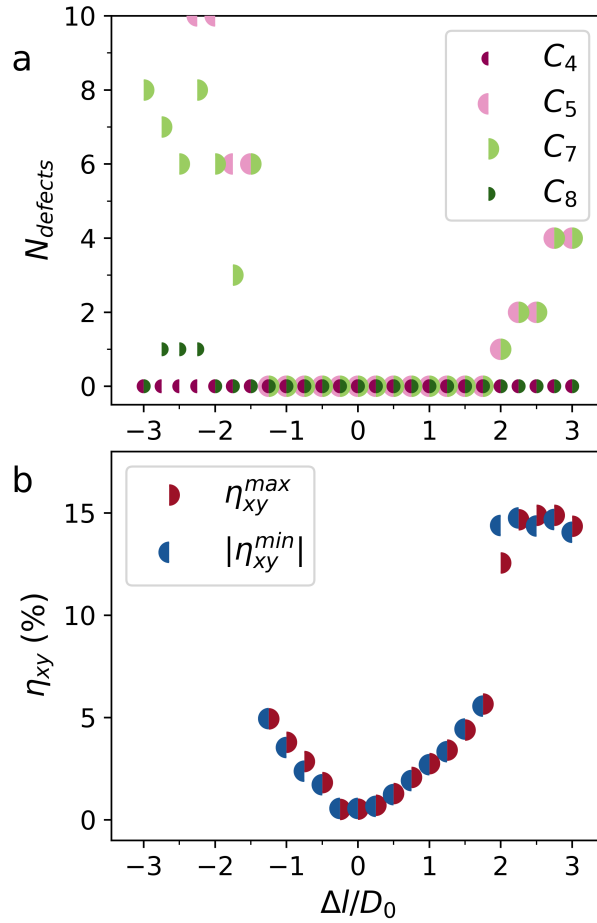
Figure 6.6: Extension and shear thresholds for creation of defects. **a** The number of 4,5,7, and 8-coordinated particles (C_4,C_5,C_7 and C_8), as found from the Voronoi diagram of the crystal. **b** Maximum affine shear strain magnitudes for a rectangular cluster. The creation of dislocation defects coincides with shear strains of $\approx \pm 5\%$.

6.9 Controlling Dislocation Emission

To avoid the creation of extraneous dislocations, we desire an embedded cluster geometry that produces a single dislocation pair on one glide plane with high repeatability. When the boundary of an embedded cluster is aligned with a slip plane in the crystal, dislocations tend to be created along that boundary provided that the extension due to particle swelling is sufficiently large. Therefore

to minimize the alignment of all but one cluster edge with slip planes, we use a half-ellipse shaped cluster. The single flat edge of the cluster is aligned with a slip plane which we denote as (00). Other planes exist within the same low-energy slip system; for symmetric half-ellipses there are two other equivalent planes which we refer to as (01) and $(0\bar{1})$.

We quantify the propensity of shear strain on a slip plane to produce a dislocation, using the negative autoconvolution of the shear field sampled around a cluster at swelling values below the defect creation threshold. For a shear field with perfect inversion symmetry on a slip plane, the maximum of the negative auto-convolution will be:

$$A_{max} = max(\eta_{xy}(x) * -\eta_{xy}(x)) = \sum_x \eta_{xy}^2(x) \tag{6.1}$$

which is proportional to the shear energy density integrated along that slip plane (in the linear elastic limit). We find that the negative autoconvolution of shear strain is a good indicator of slip planes with a high propensity to form dislocations. In fig. 6.7 the strain patterns (sampled from simulation) of a cluster are shown when aligned with two sets of slip planes, referred to here as (00) and (01). Slip planes with large negative autoconvolution maxima (A_{max}) indicate potential planes where dislocations can be produced. In order to minimize the number of spurious dislocation emissions the primary maxima, present on the flat side of the half-ellipse, should be significantly larger than other maxima. The top of the half-ellipse is a likely site for secondary emission, but the rounded sides can also emit dislocations onto other glide planes.

We use A_{max} to identify which slip planes are likely to create dislocations as the shear strain threshold is approached. Fig. 6.8a shows A_{max} with respect to the position of the half-ellipse cluster. The two families of slip planes are shown. The (00) family contains the largest peak, at the flat bottom edge of the ellipse, with a secondary peak at the top of the rounded cluster. The rounding of the cluster suppresses dislocation emission from the top surface. Also shown is A_{max} for the (01) slip planes. This slip plane generally has a smaller propensity for dislocation emission than the designed (00) plane. However, as the ratio of length l to width w of the half-ellipse cluster is changed, the difference between the primary (00) peak and the (01) peak decreases relative to
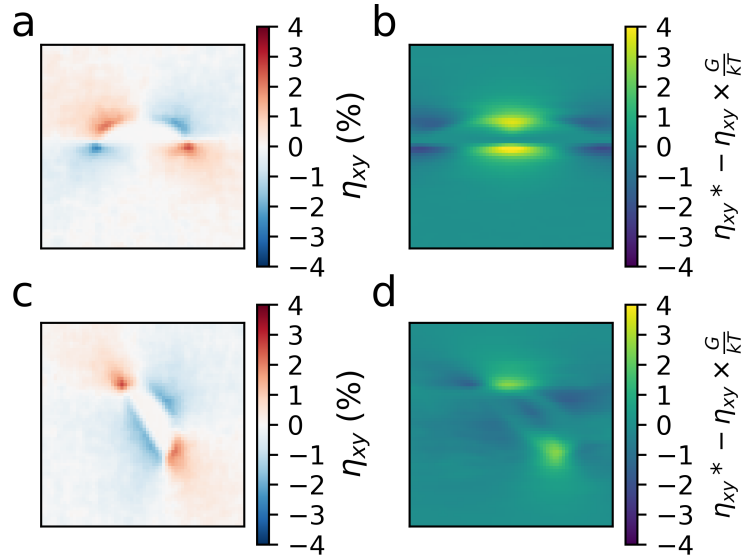
Figure 6.7: Sampled strain fields and negative shear strain autoconvolutions for a single half-ellipse. Autoconvolutions are shown normalized by the shear modulus (G) of the crystallite and thermal energy (kT). **a** Shear strain aligned with the (00) slip plane. **b** Negative autoconvolution of shear strain aligned with the (00) slip plane. Large maxima are observed at the top and bottom sides. **c** Shear strain aligned with the (01) slip plane. **d** Negative autoconvolution of shear strain aligned with the (01) slip plane. The maxima present near the rounded edge of the cluster indicates a potential site for spurious dislocation creation on this family of slip planes.

the (00) maximum (Fig. 6.8b). This means that wide half-ellipses are prone to spurious emission of dislocations into the (01) slip planes. To ensure that single dislocations are produced with high repeatability, narrow half-ellipse clusters with small w/l ratios should be used.

6.10 Dislocation Driving Forces

After dislocations are created by the swelling of a cluster, they are driven to leave the vicinity of the cluster by the strain fields present around it. During swelling (shrinking), the positive (negative) dislocation is driven away from the embedded cluster. If the pair of dislocations are allowed to recombine, then no net slip will result. Therefore it is important that the dislocation pair be as widely separated as possible. The forces that primarily motivate the motion of dislocations come from shear strain interactions. If we consider a family of half-ellipses (as in Fig. 6.8), then we can sample the shear strain magnitudes at points along the slip plane aligned with the flat edge of the
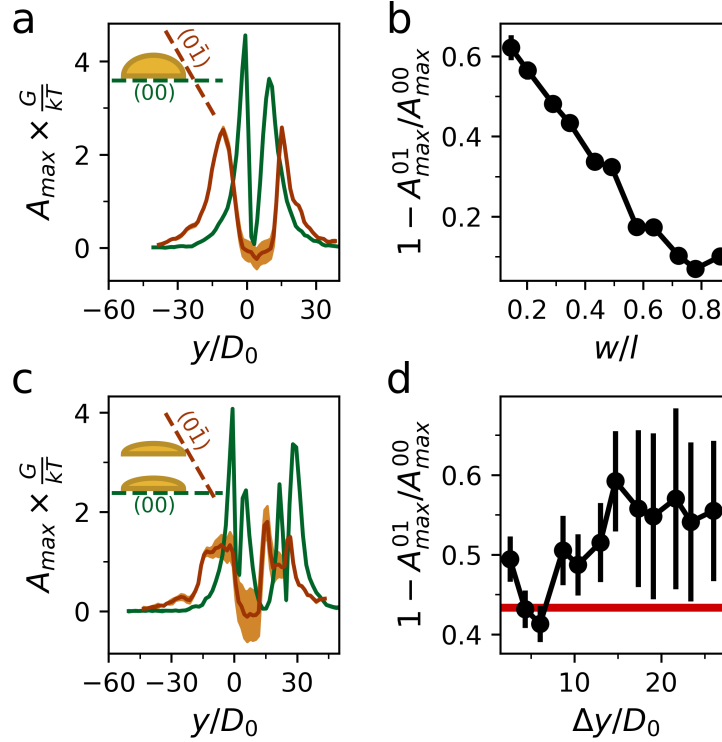
Figure 6.8: Negative shear auto-convolution as a measure of the likelihood of dislocation emission. **a** Maxima of the negative shear auto-convolution, converted to energy units using the linear shear modulus (G). The value for (00) (green) and (01) (brown) family planes are shown. Uncertainty is represented with shaded bounding curves for both lines. **b** The relative difference of peak negative shear auto-convolution between slip families as the width of the half-ellipse is increased. **c** Maxima of the negative shear auto-convolution for a cluster of the same area as (a), but split into two thinner half-ellipses. **d** The relative difference of negative shear auto-convolution between slip families for two half-ellipses with different vertical separations. The red line indicates the difference for a single cluster of the same area (from (b)).

cluster. Fig. 6.9a shows these shear values at various distances from the edge of the cluster. As the width of the embedded cluster is increased the shear strain along the primary slip plane reaches farther. Therefore, wider clusters (and thus larger) are better at forcing dislocations to glide away.

6.11 Double Half-Ellipse Clusters

By examining the trends of embedded clusters with a half-ellipse shape we have concluded that clusters with larger areas (i.e. lower aspect ratios) are more effective at sweeping dislocations from their vicinity. However low-aspect ratio clusters are more likely to produce extraneous dislocations
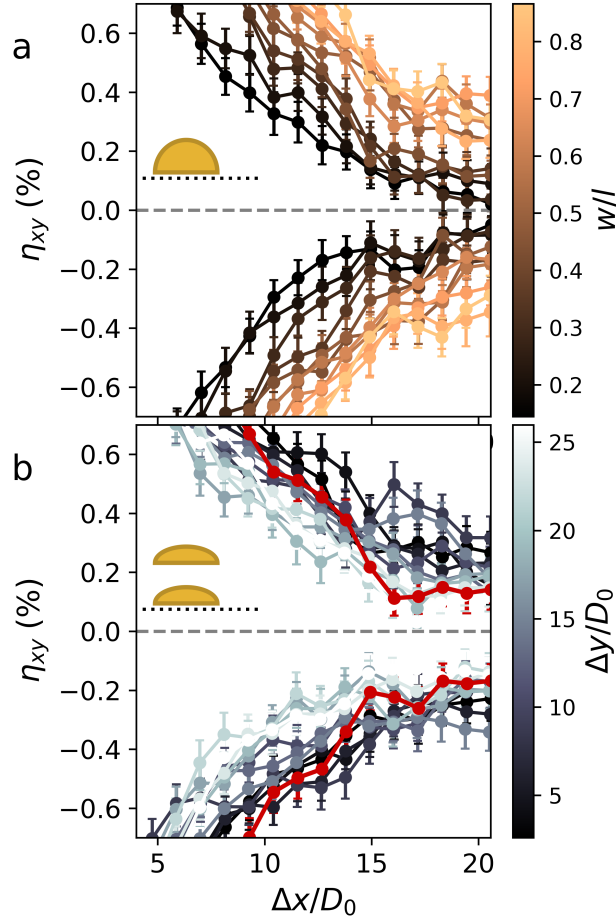
Figure 6.9: Shear strain on the primary glide plane of embedded clusters. **a** Shear strain for half-ellipses of various aspect ratios. **b** Shear strain for double half-ellipses. The red line is the shear strain from (a) for a single half-ellipse with the same area.

on other slip planes. To balance the advantages of large and small half-ellipse clusters, we propose a double-half ellipse cluster shape. In this geometry two half-ellipses, separated by a vertical offset, function as a single dislocation-producing unit. This geometry has several advantages over the single half-ellipse cluster.

First, double-half ellipse clusters have a reduced tendency to emit extraneous dislocations than single half-ellipses of the same total area. Fig. 6.10 shows the strain field and shear autoconvolution data for a cluster geometry with the same area as in Fig. 6.7, split into two clusters. The double half-ellipse cluster geometry greatly suppresses the likelihood of dislocation creation on the (01) slip plane, as it lacks any continuous sides that are aligned with those planes. Additionally, for the

(00) plane the maxima that are inbetween the two half-ellipses are suppressed by the proximity of the other cluster.
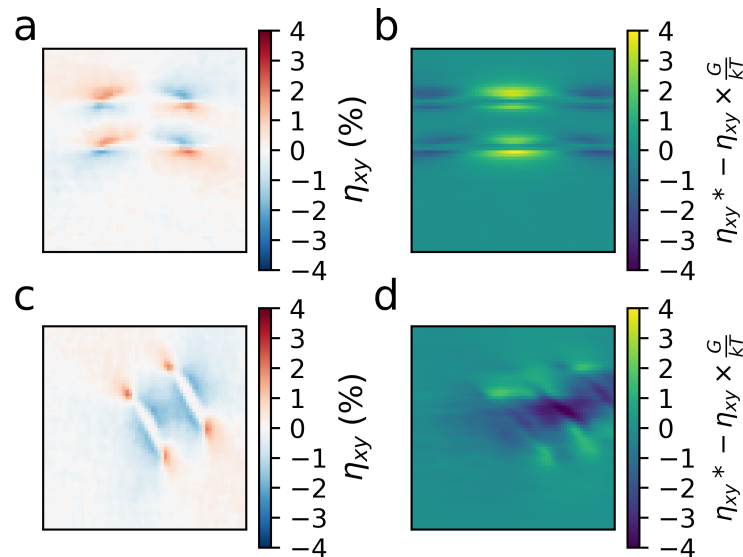
Figure 6.10: Sampled strain fields and negative shear strain autoconvolutions for a double half-ellipse cluster. Autoconvolutions are shown normalized by the shear modulus (G) of the crystallite and thermal energy (kT). **a** Shear strain aligned with the (00) slip plane. **b** Negative autoconvolution of shear strain aligned with the (00) slip plane. Large maxima are observed at the top and bottom of both half-ellipses. **c** Shear strain aligned with the (01) slip plane. **d** Negative autoconvolution of shear strain aligned with the (01) slip plane. The double half-ellipse cluster suppresses dislocation emission on this family of glide planes.

Fig. 6.8c shows A_{max} for the (00) and (01) family of slip planes. Fig. 6.8d shows the relative difference between A_{max} for the (00) family and the (01) family as a function of the vertical separation between the half-ellipses. The red horizontal line indicates the relative difference for a single half-ellipse of the same area. For small separations, the relative likelihood of extraneous emission is similar to that of a single half-ellipse with the same total area. However for larger separations, the relative difference between maxima in the (00) family and (01) family is increased above the case of a single half-ellipse.

Second, the driving shear strain that pushes dislocations away from the embedded cluster is increased at long range for the double half-ellipse cluster geometry as compared to the single ellipse. Fig. 6.9b shows the shear strain present on the primary slip plane as a function of distance to the cluster edge for double half-ellipses. The red curve is the shear strain (from Fig. 6.9a) of a

single half-ellipse with the same total area. For large vertical separations ($\Delta y/D_0 > 20$) the shear strain at long ranges is similar to or less than that from a single half-ellipse. However for small and moderate separations ($\Delta y/D_0 < 20$) the shear strains, especially at long range, are larger in magnitude for the double half-ellipse geometry than the single half-ellipse. This is a larger effect for positive strains, another result of the tension-compression asymmetry present due to the nature of the particle pair potential. The increased shear strain magnitude at long range is a result of the additional flat edge of the second 'booster' half-ellipse. This feature produces more shear strain than the relatively flat sides of a wide single half-ellipse.

6.12   Biasing Dislocation Emission

By investigating the thresholds for dislocation creation as well as the distribution of shear strain around the embedded cluster, we have arrived at a cluster design that produces and drives dislocations reliably on one slip plane. To enact cumulative change to the crystallite's surface, dislocations of opposite handedness must be consistently emitted in opposite directions. One way to accomplish this biasing is to make a notch in the cluster edge that defines the primary slip plane. This breaks the reflection symmetry of the cluster, and results in biased dislocation emission. Fig. 6.11 shows the slip accumulated in crystallites ($N = 13,051$) containing embedded single half-ellipse clusters. As the notch in their primary slip plane is shifted from the center of the cluster, dislocations are more likely to be emitted directionally depending on their handedness, resulting in cumulative slip.

The notch causes two related effects that are responsible for biased emission. First, when the notch is close to a corner it reduces the likelihood of dislocation pair creation at that corner. For the primary slip plane, this means that the dislocation pair is first created at the corner farthest from the notch. The positive dislocation is then swept from the vicinity of the cluster by compressive strain fields.

Second, we find that the notch also tends to attract the negative dislocation during the shrinking

109

phase of the cycle. This often results in the negative dislocation leaving the cluster from the notched side, and thereby splitting the dislocation pair apart. The attraction of the negative dislocation to the notched side of the cluster as it returns from its maximum swelling diameter is a less consistent effect than that of the notch on the location of initial pair creation. As such, this attraction can limit the efficiency of dislocation pair splitting. This symmetry-breaking effect was found to be insensitive to the shape of the notch.
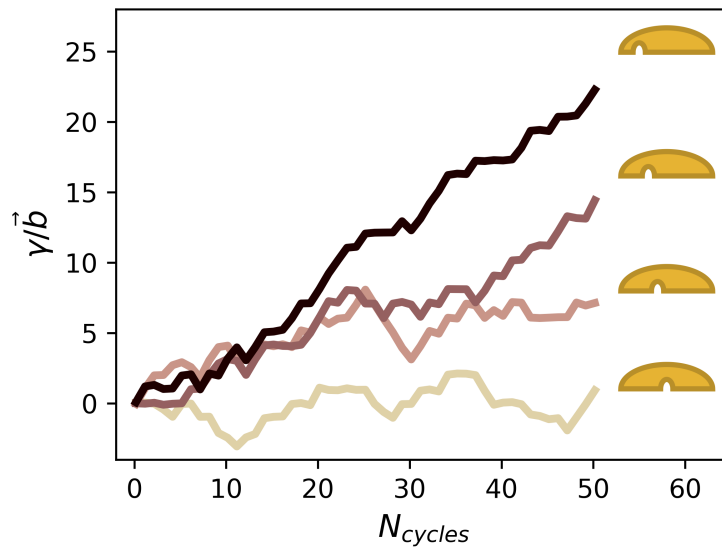
Figure 6.11: Biasing of dislocation emission. Cumulative slip over 50 cycles for clusters with different degrees of notch asymmetry. Greater asymmetry of the edge that defines the primary slip plane leads to greater robustness of dislocation pair splitting.

6.13   High-Performing Clusters

Fig. 6.12 shows the geometry of the highest performing cluster we found in this study. This cluster can be broken down into the key design features described above. The primary slip plane is defined by the bottom-most flat edge of the cluster. During the swelling phase, a dislocation pair is first produced at Fig. 6.12a. Rounded edges (Fig. 6.12b) suppress the emission of dislocations onto other glide planes. A notch in the bottom flat edge (Fig. 6.12c) ensures that dislocations are reliably separated by the sign of their Burgers vector. Lastly a second half-ellipse 'booster'

cluster (Fig. 6.12d) positioned above the first half-ellipse provides additional shear strain that assists in driving dislocations away from the cluster after they have been produced. The lower flat edge of the booster cluster is prevented from emitting its own dislocation due to the suppressing effects of the strain field of the bottom half-ellipse. We employ embedded clusters composed of double half-ellipses with $l = 30D_0$ and $w = 6\sqrt{3}D_0/2$. The swelling and shrinking diameters ($\eta_p D_0$ and $\eta_n D_0$, respectively) of constituent particles are chosen to produce a length extension of $\Delta l_p = l(\eta_p - 1) = 2.0$ and $\Delta l_n = l(\eta_n - 1) = -1.2$. Because the important quantity is total cluster length extension as the variable-size particles swell, the required per-particle expansion or contraction required is set by the total length of the cluster. Clusters composed of small numbers of particles will require large per-particle expansions, while clusters composed of large numbers of particles will require only small per-particle diameter changes.
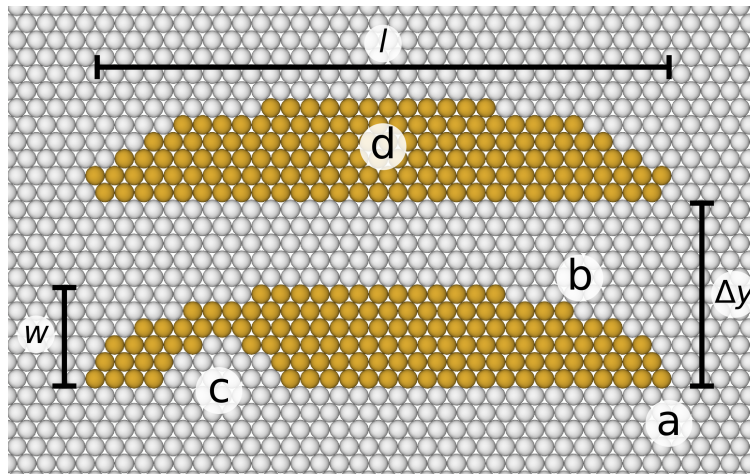
Figure 6.12: The important features of a variable-diameter cluster that biases the emission and propagation of defects. Half-ellipse shaped sub-components are l long and w wide. **a** The 'cutting' edge of the cluster. A flat edge aligned with a slip plane is needed to produce shear strains that will create a pair of dislocations. **b** Rounded corners. Corners other than the primary slip edge should be blunted to avoid spawning additional dislocation pairs. **c** The biasing notch. This notch guides the negative dislocation of the pair to leave the vicinity of the cluster in the opposite direction as the positive dislocation. **d** Secondary booster. The addition of another cluster with similar features at a Δy offset to the cutting cluster drastically increases the maximum range which the dislocation pair can be split. The sharp edges of this half-ellipse cluster add additional shear strains that drive dislocation motion.

Fig. 6.13 shows several important steps in the swell/shrink cycle of the high performance clus-

ter geometry described above. In this figure, the Voronoi cells around each particle are shown as polygons. Non-six coordinated particles are colored by their Voronoi cell vertex number. Fig. 6.13a shows a time during cluster swelling immediately after dislocation pair creation. We see that the pair was created at the leading edge. Stresses at the trailing edge also produce particles with disturbed coordination shells, but this dislocation pair quickly recombines. Fig 6.13b shows a time during the maximum diameter hold. During this time the negative dislocation remains trapped near the cluster, while the positive dislocation migrates away to escape the compressed environment near the cutting edge. Fig. 6.13c shows a time during the minimum diameter hold part of the cycle. During this hold, the negative dislocation is repelled by the tensile environment around the cluster. If the positive dislocation had not migrated far enough away from the cluster during the maximum diameter holding phase, then it could be attracted back during this part of the cycle. Due to the intrinsic tension-compression asymmetry of the SLJ pair potential, driving the negative dislocation to migrate is the limiting step. Driving the positive dislocation is comparatively easy.

6.14   Discussion

Reversibility of Operation   In this study, particles of tunable diameter are bonded together into clusters, and so considered as permanent, though flexible, units. The direction of dislocation emission biasing is entirely set by the geometry of the cluster, in particular by the placement of the notch (Fig. 6.12c). To have a cluster that can reverse its direction of biased dislocation emission, it would be necessary to have a cluster in which the notch can be changed in situ. This might be possible by using a multiplexing scheme where there are three types of particles that can be independently swelled and deswelled. One type would comprise the majority of a cluster with two notches. The other two types would fill these notches. By activating the main body of the cluster and only one of the notches, the direction of operation of the cluster could be selected.

The Role of Temperature   Temperature plays an important role in the process of splitting a dislocation pair via elastic forces. The influence of temperature comes into play several ways.
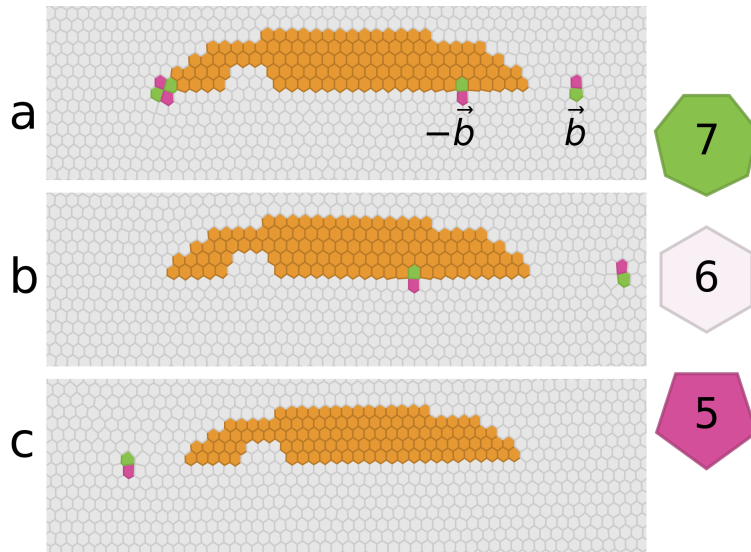
Figure 6.13: Important points in the swell/shrink cycle of a notched half-ellipse cluster. Voronoi cells surrounding each particle are shown colored by their voronoi coordination, C (or yellow, if representing a tunable-diameter particle). **a** The initial split of the dislocation pair has just occurred during the swelling phase. Another dislocation pair can be seen at the left edge of the embedded cluster, however this pair quickly recombines. **b** During the large diameter holding phase, the negative dislocation remains trapped on the cluster surface while the positive dislocation is repulsed by the compressed environment of the swollen cluster. **c** As the cluster shrinks to its original diameter and below, the negative dislocation is drawn towards the notch end and then repelled from the tensile strains present around the shrunken cluster.

First, as the embedded cluster changes size, it imposes long range distortions to the crystal that drive the motion of dislocations. The magnitude of thermal fluctuations in the strain field set the range at which the cluster's strain field is effective at motivating dislocation motion. At low (high) temperatures, the influence of the cluster is strong (weak) relative to thermal fluctuations far from the cluster. However, at lower temperatures dislocations and vacancies are less mobile. Therefore they will not be able to naturally diffuse and heal out, meaning that an escalating pile-up of damage due to cluster cycling is more common. The temperature used in this study represents a compromise between the beneficial and adverse effects of low temperature. We expect that in addition to temperature, the depth and steepness of the interaction potential can be tuned to achieve similar effects. It is likely that particle interactions that produce much better dislocation mobility characteristics are possible (i.e. a pair potential with a more symmetric attractive well).

Swellable Particles in Vitro   In theory, many polymer-based nanoparticles could be swollen by changing their solvent environment. The surrounding bath's composition would be changed over the course of one cycle in order to create cyclic particle expansion. Therefore, the time required for each cycle would depend upon the maximum rate that the solvent's composition could be changed (without introducing bulk flows that destroy the colloidal crystallite). Highly swellable particles such as produced by coating with DNA surface ligands [42] suggest the possibility to engineer particle response both in terms of solvent concentration and species. While chemical swelling may be rate limited by mass transport in the solvent, it lends itself readily to sensing applications in a biological or microfluidic environment. Additionally, a class of hydrogels based on poly(N-isopropylacrylamide) (poly(NIPAM)) open the possibility for thermally-swellable particles [178]. Combination chemical and thermal responsive size-changing nanoparticles have also been demonstrated [179].

Dislocations as 'Metamodules'   When a reconfigurable robot is composed of densely packed subunits (modules), the motion of modules to enable ensemble reshaping must occur entirely on the surface, as there is no room for modules to move through the bulk. As the number of modules in a robot is increased, the surface area grows much slower than the volume. Therefore for large numbers of modules this surface restriction is a potential limitation that could cap the reconfiguration rate [175]. Designs like the Crystalline Robot [168] and the Telecube [169] aimed to address this issue by making modules capable of expansion or contraction. In a manner analogous to a dislocation, modules contract in sequence, transporting mass through the bulk of the robot array. This mode of operation shares similarities to a family of crystalline defects that include dislocation loops and crowdions. In a crowdion, a linear chain of N crystal lattice sites have $N + 1$ (interstitial type) or $N - 1$ (vacancy type) particles occupying them [180]. Unlike more common interstitials and vacancies, the extra or missing particle is not localized to a single site, but instead effectively spread out over many sites with fractional occupancy. Ensembles of cubes simulated with thermal agitation have been shown to display vacancy-type crowdions as an emergent behavior [181, 182].

This suggests that stochastic versions of cube-type lattice robots might display crowdion-type mass transport without careful algorithmic control of neighbor bonding and only mild module compressibility. Similarly, dislocation loops are arrangements of crystal lattice planes where $N+1$ or $N-1$ planes occupy the space of N planes in a distributed manner.

Bulk reconfiguration has also been proposed in incompressible lattice robots. Clearly, insufficient room exists to efficiently transport modules through a space-filling or dense-packed bulk, so authors have proposed porous assembly types that alleviate this issue [183, 184, 185, 175]. This shifts the focus of reconfiguration planning away from individual modules to groups of modules (referred to as 'metamodules'), which maintain an open structure. The concept of a metamodule that maintains a sufficiently low density to permit transport can be directly compared to a dislocation. Dislocations are emergent phenomena that exactly perform the task that metamodules are designed for. Bulk material shape change results in 'on-the-fly' dislocation creation to transport mass and enable plastic deformation. De Rosa et al. proposed a similar concept in the form of open holes that are shepherded around the interior of a lattice robot. These holes perform the dual function of transporting (negative) mass through the bulk and providing a low density environment to allow for reconfiguration. From the behavior of crystalline materials under deforming stresses, we know that such holes are not the lowest free-energy motif that accomplishes these goals; instead, nature has selected dislocations as its metamodule of choice.

The ability of lattice robots to employ dislocations as on-demand emergent metamodules will depend upon the connection type present between neighbors. Many proposed crystalline robots have rigid connections between neighbors that are toggled according to algorithmic planning. This process of latching onto a new neighbor represents a significant fraction of the difficulty of creating functional prototypes. Others have shown that near-isotropic bonding between neighbors is also a feasible strategy for robot design without a well defined crystal structure [172, 152]. However, we show here that isotropic subunit interactions coupled with a crystalline arrangement unlock the potential of using dislocations as emergent metamodules. Lattice robots with stiff, angle-dependent interactions are equivalent to covalently or ionically bonded materials. Dislocations are typically

not important to the deformation of these materials, with fracture instead being the primary mode of shape change. For robotics applications, particularly during reconfiguration, the ensemble is desired to behave more like a ductile metal. The potential power of our work lies in the scalability of employing dislocations. Since dislocations are emergent, stable structures with high mobility, no control need be exerted to maintain them as they migrate. In our scheme, only the collective action of a small number of subunits together is sufficient to create and move dislocations, thereby reshaping the larger domain.

6.15   Conclusion

In this study we discussed a simulated 2D colloidal system in which clusters of tunable-diameter particles are embedded. By cyclic swelling and shrinking of the particles in these clusters, dislocations are created and motivated to glide. Through design of the cluster shape, dislocation emission and migration can be strongly biased. Biased dislocation emitters fundamentally exert a shear slip effect, and by arranging multiple emitters in different configurations, different compound operations can be accomplished. This work presents an alternative mechanism for colloidal crystallite reconfiguration. We also explored how dislocations fulfill for colloids the role sought by 'meta modules' in lattice robotics research, and suggest that dislocations should be considered as a fundamental unit of reconfiguration in those systems as well.

CHAPTER 7

Conclusion and Outlook

7.1 Summary

This dissertation has been an exploration of how local forces can be exerted within a crystalline colloidal material to take control over the dynamics of defects. In a broad sense, all changes of shape or arrangement of material within a crystalline domain must be accompanied by the presence of defects. Under the conditions in which they are stable, the crystalline state pins all particles to lattice sites, and imposes barriers and penalties to deviations from that order. Any reorganization must come with a breakdown of that order, at least locally. From this point of view the study of defect dynamics is fundamental to the study of any crystalline material that we wish to reorganize. Studying defects in colloidal systems with activity brings together two worlds of study that are often not in contact; the young and growing out-of-equilibrium colloidal suspensions community and the mature metallurgical community. The chapters of this dissertation represent a coherent effort to understand how active matter could be used to modify the properties or shape of colloidal crystals.

In Chapter 3, we begin this effort by investigating the mechanical properties of crystals which are formed from particles which repel each other. There we show how materials that interact repulsively and those that interact attractively are comparable and even interchangeable, to some degree. The mechanical behavior of the solid in the continuum limit does not care if the free energy of deformation arises from enthalpic attraction or confinement by pressure. The difference we

found for repulsive potentials was that the asymmetry between the cohesive influence of confining pressure and repulsive interaction could result in large tension-compression asymmetries. Such effects limit the applicability of the linear elastic framework, however the same difficulties arise for attractive interactions with particularly asymmetric potential wells. Our final result was to show that the linearity of a repulsive solid increases as the confining pressure is reduced towards the melting point. These results equip us with essential information for understanding elasticity in colloidal systems; when operating sufficiently close to the melting point of the solid, all the useful tools of linear elastic theory can be leveraged to understand and predict driving forces.

In Chapter 4 we take the information gleaned from Chapter 3 and use it to analyze the interaction of an interstitial particle and a dislocation. This chapter introduces the concept of *strain field alchemy*, in which we treat the shape of an object as a fluctuating quantity that can be optimized to maximize strain-field-mediated forces. By allowing the strain field interaction of our interstitial to guide the selection of its shape, we arrive quickly at geometries that can be demonstrated to drive dislocations to glide in MD simulations. This chapter shows that active particles can be tailored to take specific control of dislocations. If a dislocation is a knife that reshapes the interior of a crystal, then we show here that a handle can be fashioned in the form of an active particle.

In Chapter 5 we turn away from linear elastic theory and examine the interactions between the channels of free volume that exist near a stacking fault and a rod-like active interstitial. We find that the radius, length, and active force magnitude of the interstitial control the rotational diffusion properties and hence the path it traces out in a crystal. The geometry of this path determines the likelihood of an active particle encountering a stacking fault. This work shows that active interstitials have advantages over traditional passive hardening additives. They can be designed not only to bind strongly to dislocations, but also to search large distances to find them. As a result, even very small additions of such particles can have large effects on the mechanical properties of the solid. In many ways, this study complements much that was missing from Chapter 4. Here the rotational diffusion of active rods embedded in a crystal is considered, as well as an attraction mediated by free volume (which is beyond the reach of linear elasticity). Furthermore, the goal is

not to drive dislocations to glide, but rather to trap them and so improve resistance to shear from an external force.

Finally, in Chapter 6 we show how in a 2D attractive colloidal crystallite dislocations can be used to sequentially reshape the exterior surface. We outline a scheme to produce dislocations in a biased way using an embedded cluster of particles that can shrink or swell their diameters. The geometry of the variable-size cluster is found to be critical to achieving reliable biased emission of dislocations. This biased dislocation emission can be exploited to induce a variety of shape changes in colloidal crystallites. This study is in some sense the culmination of the efforts in this dissertation, as it most plainly demonstrates the guiding vision behind these studies. Indeed, Chapters 4 and 5 might more easily be understood in retrospect as investigations seeking to bring the achievements of this chapter into 3D colloidal crystals.

Taken together, the works in this dissertation seek to establish the potential of studying the interaction of active matter with crystalline defects in a colloidal setting. We justify these works primarily through two applications; the creation of small-scale robotic devices (which would be required to adapt their shape in order to adapt their functionality) and the manipulation of optically relevant colloidal crystals in a dynamic fashion. It is my hope that the work collected here can serve as a stepping stone towards those applications.

7.2   Future Outlook

As with all research, there are many questions remaining to be addressed and expanded upon, and I hope to see others take them up. In this section I will mention some of the experimental and theoretical extensions that are possible to the work that has been presented here.

7.2.1   Experimental Studies

The work contained in this dissertation is entirely computational. While colloidal dislocations have been observed [69, 70], their interaction with active matter has not been experimentally investi-

gated. The interaction of active particles with colloidal defects is in general challenging to realize. Dietrich et al. [77] explored active particles behaving as interstitials in 2D films of colloidal particles trapped on liquid-liquid interfaces. Recently Ramananarivo et al. [78] have experimentally produced results which follow predictions made by van der Meer et al. in 2016 [75], in which active particles accelerate the annealing of a 2D colloidal polycrystal. These studies do not explore the nature of the interaction between defects and active matter, instead focusing on bulk observable quantities (diffusion rates and annealing rates). As the systems considered in the chapters of this work involve more complex active particles, as well as observations in 3D crystals, greater experimental challenges can be expected.

The realization of Chapter 6 experimentally is in my opinion the most feasible in the short term, as it involves relatively modest requirements for particle activity, which can be supplied by thermal or chemical swelling. Furthermore, the essential results of biased dislocation creation and emission can be tested using optical force microscopy similar to that carried out by Irvine et al. [73], in which multiple colloidal particles were optically manipulated to produce or move dislocations. The results of Chapter 6 may suggest a means to increase the efficacy of such optical defect control.

As for the 3D work presented here, the study in Chapter 5 lends itself more readily to experimental realization because the end result is a modification of bulk plasticity as a result of activity. Individual dislocations can be imaged [69, 70, 71], which may open the possibility of directly observing the interaction of an interstitial and dislocation as studied in Chapter 4. However more likely for 3D studies would be the observation of a bulk property change due to dislocation-coupled activity.

Another possibility for experimental realization lies in scaling up the meta-atoms of my studies to the macroscopic scale. As outlined in Chapter 6, as the size of the active meta-atoms are increased we cross into the territory of swarm robotics [168, 169, 183, 184, 185, 175]. While the increased scale eases certain experimental difficulties, a key concern is the breakdown of linear elastic behavior as the apparent hardness of the meta-atomic interactions becomes stiffer (as

suggested in Chapter 3). My results suggest that sufficient agitation would be required to create an effective temperature of the granular or larger system, which could return it to the strain field fluctuation scale that has been studied in the works of this dissertation.

7.2.2 Further Computational and Theoretical Studies

The work presented in Chapter 4 concerning strain field alchemy suggests several follow up studies. We have shown here an example of a particularly relevant interaction type, that of a dislocation with an active interstitial. However the concept should also apply to studies of the interaction of active interstitials with each other, or indeed any other strain field-producing object embedded in a crystal, provided that the linear elastic limits are respected. The linear elastic limit presents the other obvious opportunity for further work; there are strong, super-elastic interactions that occur in the cores of dislocations [164]. I expect that the interaction between an active interstitial and the core of a colloidal dislocation could provide significantly higher binding strengths than the elastic interaction alone, if optimized. Predicting, or even sampling the change in core binding strength with interstitial geometry presents a challenging but potentially fruitful problem.

In Chapter 5 active interstitials were found to have strong binding preferences for the particular topology of the void space present near stacking faults. Notably absent from that study was consideration of other shapes beyond simple rods. Segmented rods, disks, or bead-chain interstitials may present opportunities for further improvement of binding strength or tuning of mobility. Also interesting is to consider how void topology can be exploited in other, more complex crystal structures.

Lastly, the embedded dislocation emitters of Chapter 6 suggest a few directions for further study. In particular, the mobility of dislocations and the strain fields induced by the cluster places a limit on how far a dislocation dipole can be separated. To de-couple the creation of the pair from its separation, it may be possible to exploit the tactics used in Chapter 4 (i.e., bind an active particle to a dislocations to increase its mobility). Beyond this, the collective dynamics of large numbers of such dislocation emitters acting in tandem, or with specific phase relationships between them

could be explored. Lastly, the dislocation emitter concept could be demonstrated in 3D. Expanding from 2D to 3D permits for the exploration of dislocation loops, such as shown in Chapter 4.

Ultimately, many opportunities await, and it is my sincere hope that others will take up these or similar studies to advance the art.

APPENDIX A

Sampling of Elastic Moduli from Stress and Strain Fluctuations

Gusev, Zehnder, and Suter propose a modification to the PR method that improves convergence to acceptable rates [88]. Consider a system described by the Hamiltonian

$$H = \sum_a \frac{p_a^2}{2m_a} + U(r_{ab}), \tag{A.1}$$

where p_a and m_a are the momentum and mass of a particle a, and $U(r_{ab})$ is the potential energy depending only on pairwise distances. When the six independent components of the symmetric strain tensor are considered as coordinates, the following identity holds:

$$\langle \eta_{ik} \frac{\partial H}{\partial \eta_{lm}} \rangle = k_B T \delta_{il} \delta_{km}. \tag{A.2}$$

The homogeneous strain that describes the change in a vector is written as

$$r^2 - r^{'2} = 2\eta_{ik} x_i' x_k', \tag{A.3}$$

where $\mathbf{r} = \begin{pmatrix} x_1 & x_2 & x_3 \end{pmatrix}$ is the initial vector, and $\mathbf{r}' = \begin{pmatrix} x_1' & x_2' & x_3' \end{pmatrix}$ is the final vector. Using the box matrix, the change in coordinates can be represented as $x_i' = \langle h \rangle_{ik} h_{kl}^{-1} x_l$. Differentiating and combining equations, it is found that

$$\langle \eta_{ik} \sum_{a>b} \frac{\partial U}{\partial r_{ab}} \frac{\langle h \rangle_{lp} h_{ps}^{-1} x_s \langle h \rangle_{mt} h_{tw}^{-1} + x_w}{r_{ab}} \rangle = \frac{1}{2} k_B T \left(\delta_{il} \delta_{km} + \delta_{im} \delta_{kl} \right). \tag{A.4}$$

Here, the kinetic contribution has been dropped since we have enforced that $\langle \eta_{ik} \rangle = 0$. The found expression can be used to modify the initial form of the fluctuation formula so that

$$C_{iklm} = \langle \eta_{ik} \sigma_{nj} \rangle \langle \eta_{nj} \eta_{lm} \rangle^{-1}, \tag{A.5}$$

where σ_{ik} are components of the microscopic stress tensor

$$\sigma_{nj} = \frac{1}{V} \left(\sum_{a>b} \frac{\partial U}{\partial r_{ab}} \frac{(x_{ab})_n (x_{ab})_j}{r_{ab}} \right). \tag{A.6}$$

Due to the ensemble averaging, the momentum terms in the microscopic stress tensor cancel out and have not been included here. This modification of the PR method enjoys improved convergence because the stresses and strains in a system are correlated. The PR method requires that the product $\langle \eta_{ik} \eta_{lm} \rangle$ be fully converged. By exploiting the correlation implied by Hooke's law,

$$\sigma_{ik} = C_{iklm} \eta_{lm}, \tag{A.7}$$

this convergence requirement is relaxed and accurate elastic modulus tensors can be found more quickly. In practice, the tensor found by this method approaches the symmetry properties of the idealized tensor, that is, its Voigt symmetry [87] and crystal symmetry. A rough measure of convergence employed here is to enforce Voigt symmetry on the resulting C_{iklm} and report the fractional magnitude change that this results in. Small changes are unavoidable, given that this is a sampling process, while large changes are an indicator of an improperly sampled system.

APPENDIX B

Mura's Method of Eigenstrains

The calculation of spatially varying strains is challenging because of the continuity equations that must be obeyed. Analytic solutions for particular geometries derived in the literature follow the general approach of a Green's function method, analogous to the same method as employed in studies of electrostatics [89]. Green's functions have been obtained explicitly only for isotropic and transversely isotropic solids. This means that when considering a real anisotropic material, Green's method is complex. We also seek a method that lends itself well to numerical evaluation and can handle geometries that are as close to arbitrary as possible. For these purposes, the best solution is the method of 'eigenstrains' as outlined by Mura [90].

The method of eigenstrains is a procedure developed to understand the strain fields that arise as the result of an inclusion in a crystal. The term itself was coined by Toshio Mura to refer to strains that are introduced in a continuum without the action of external forces, *i.e.*, in a stress-free manner. In various contexts, Mura's eigenstrains have been called elastic polarization, residual stress, or stress-free transformations. In general terms, the method of solving for eigenstrains yields a way to suppose that a state of strain exists within a domain, and then determine the resulting equilibrated strain distribution that would arise. The problem amounts fundamentally to enforcing that the compatibility equations of strain are satisfied. The derivations given here follow Mura's work [90].

Total strain (η_{ij}) in a domain can be regarded as the sum of elastic strain (e_{ij}) and eigenstrains (η_{ij}^*):

$$\eta_{ij} = e_{ij} + \eta_{ij}^*. \tag{B.1}$$

The total strain must be compatible

$$\eta_{ij} = \frac{1}{2}\left(u_{i,j} + u_{j,i}\right), \tag{B.2}$$

where $u_{i,j} = \partial u_i / \partial x_j$. The elastic stress is related to the elastic strain *via*

$$\sigma_{ij} = C_{ijkl}e_{kl} = C_{ijkl}\left(\eta_{kl} - \eta_{kl}^*\right) = C_{ijkl}\left(u_{k,l} - \eta_{kl}^*\right). \tag{B.3}$$

During these calculations, the material domain is assumed to be free from any external force or surface constraint. These conditions are written as

$$\sigma_{ij,j} = 0, \tag{B.4}$$

$$\sigma_{ij}n_j = 0, \tag{B.5}$$

where n_j is the unit normal vector of the boundary of the domain. Using these constraints and the compatibility requirement together, the fundamental equations to be solved are

$$C_{ijkl}u_{k,lj} = C_{ijkl}\eta_{kl,j}^* \tag{B.6}$$

and

$$C_{ijkl}u_{k,l}n_j = C_{ijkl}\eta_{kl}^*n_j. \tag{B.7}$$

In cases considered here, the domain is assumed infinite in extent, so eq. B.5 is replaced with the condition $\sigma_{ij}(x) \to 0$ as $x \to \infty$. The fundamental compatibility is given *via* eq. B.2. However, more commonly referred to are the equations derived therefrom by eliminating u_i. This leaves

$$\epsilon_{pki}\epsilon_{qlj}\eta_{ij,kl} = 0. \tag{B.8}$$

Here, ϵ_{pki} refers to the permutation matrix, whereas $\eta_{ij,kl}$ denotes the derivatives of the strain matrix. If working in an infinitely extended domain, then the fundamental equations are simplified to only eq. B.6. We then consider $\eta_{ij}^*(x)$ to be given in the form of a single sine wave of amplitude $\bar{\eta}_{ij}^*(\xi)$, where ξ is the wave vector corresponding to the given period of the distribution. The eigenstrain is expressed as

$$\eta_{ij}^*(x) = \bar{\eta}_{ij}^*(\xi)e^{i\xi \cdot x}, \tag{B.9}$$

where $i = \sqrt{-1}$ and $\xi \cdot x = \sum_k \xi_k x_k$. The solution to the fundamental equation can also be expressed as a single wave of the same period:

$$u_i(x) = \bar{u}_i(\xi)e^{i\xi \cdot x}. \tag{B.10}$$

Combining these expressions with eq. B.6 yields

$$C_{ijkl}\bar{u}_k\xi_l\xi_j = -iC_{ijkl}\bar{\eta}_{kl}^*\xi_j. \tag{B.11}$$

The derivation $(i\xi \cdot x)_{,l} = i\xi_l$ has been used. Using the notation

$$K_{ik}(\xi) = C_{ijkl}\xi_j\xi_l, \tag{B.12}$$

$$X_i = -iC_{ijkl}\bar{\eta}_{kl}^*\xi_j, \tag{B.13}$$

the three equations implied by eq. B.11 can be expressed as

$$K_{11}\bar{u}_1 + K_{12}\bar{u}_2 + K_{13}\bar{u}_3 = X_1, \tag{B.14}$$

$$K_{21}\bar{u}_1 + K_{22}\bar{u}_2 + K_{23}\bar{u}_3 = X_2, \tag{B.15}$$

$$K_{31}\bar{u}_1 + K_{32}\bar{u}_2 + K_{33}\bar{u}_3 = X_3, \tag{B.16}$$

$$\tag{B.17}$$

and $\bar{u}_i$ is obtained as

$$\bar{u}_i(\xi) = X_j N_{ij}(\xi)/D(\xi), \tag{B.18}$$

where N_{ij} are co-factors of the matrix

$$\mathbf{K}(\xi) = \begin{pmatrix} K_{11} & K_{12} & K_{13} \\ K_{21} & K_{22} & K_{23} \\ K_{31} & K_{32} & K_{33} \end{pmatrix}, \tag{B.19}$$

and $D(\xi)$ is the determinant of $\mathbf{K}(\xi)$. Due to the Voigt symmetry of C_{ijkl}, it follows that

$$K_{ki} = C_{kjil}\xi_j\xi_l = C_{klij}\xi_l\xi_j = C_{ijkl}\xi_l\xi_j = K_{ik}, \tag{B.20}$$

$$N_{ij} = N_{ji}. \tag{B.21}$$

Explicitly, $D(\xi)$ and $N_{ij}(\xi)$ are:

$$D(\xi) = \epsilon_{mnl}K_{m1}K_{n2}K_{l3}, \tag{B.22}$$

$$N_{ij}(\xi) = \frac{1}{2}\epsilon_{ikl}\epsilon_{jmn}K_{km}K_{ln} \tag{B.23}$$

$$= K_{im}K_{mj} - K_{mm}K_{ij} + (\epsilon_{mn1}K_{m2}K_{n3} + \epsilon_{mn2}K_{m3}K_{n1} + \epsilon_{mn3}K_{m1}K_{n2})\,\delta_{ij}. \tag{B.24}$$

By substituting eq. B.18 into eq. B.10, the solution for u_i is obtained:

$$u_i(x) = -iC_{jlmn}\bar{\eta}^*_{mn}(\xi)\xi_l N_{ij}(\xi)D^{-1}(\xi)e^{i\xi \cdot x}. \tag{B.25}$$

The corresponding strain is found as

$$\eta_{ij}(x) = \frac{1}{2}C_{klmn}\bar{\eta}^*_{mn}(\xi)\xi_l \left(\xi_j N_{ik}(\xi) + \xi_i N_{jk}(\xi)\right)D^{-1}(\xi)e^{i\xi \cdot x}. \tag{B.26}$$

If we restrict ourselves to the linear regime of elasticity, then a superposition of solutions would also be a valid solution. Therefore we can solve for arbitrary distributions of eigenstrain by expressing it as a series of waves:

$$\bar{\eta}^*_{ij}(x) = \sum \bar{\eta}^*_{ij}(\xi)e^{i\xi \cdot x}. \tag{B.27}$$

The final solution of strain is likewise

$$\eta_{ij}(x) = \frac{1}{2}\sum C_{klmn}\bar{\eta}^*_{mn}(\xi)\xi_l \left(\xi_j N_{ik}(\xi) + \xi_i N_{jk}(\xi)\right)D^{-1}(\xi)e^{i\xi \cdot x}, \tag{B.28}$$

where summations are taken over ξ.

This process can actually be implemented succinctly in the Python programming language using functionality from the NumPy package. Below, I have reproduced a function which calculates the strain distribution from a given eigenstrain distribution, an elastic modulus tensor, and a list of k-points.

```python
import numpy as np


# Make a list of k-points over which the eigenstrain will be calculated.
# This function is kept separate, since the list can be pre-computed and
# saved for multiple iterations of eigenstrain calculation.
# inputs:
# size - a 3-tuple, the (x,y,z) size of the simulation domain.
# vox_dist - the real space distance between voxel centers
```

```python
# output:
# gamma - a size[0]*size[1]*size[2] by 3 array of Fourier space points.


def build_gamma(size, vox_dist):
    # The Fourier space points.
    # For speed, these could be pre-computed and passed in
    gX, gY, gZ = np.meshgrid(np.fft.fftfreq(int(size[0]),d=vox_dist),
                             np.fft.fftfreq(int(size[1]),d=vox_dist),
                             np.fft.fftfreq(int(size[2]),d=vox_dist))


    # Due to row/column convention, axes of
    # the returned array should be swapped
    gX = np.swapaxes(gX,0,1)
    gY = np.swapaxes(gY,0,1)
    gZ = np.swapaxes(gZ,0,1)
    gamma = np.append(np.append(gX.flatten().reshape((-1,1)),
                gY.flatten().reshape((-1,1)), axis=1),
                gZ.flatten().reshape((-1,1)), axis=1)


    return gamma



# Computes strain from eigenstrain
# inputs:
# eigenstrain - a tensor of shape (x,y,z,3,3), where x/y/z are the
# number of voxels in each physical dimension.
# Each voxel has a 3 by 3 eigenstrain matrix associated with it.
# gamma - an array of shape (x*y*z,3) with the Fourier space
# coordinates of the voxels.
# Cijkl -- an array of shape (3,3,3,3). The elastic modulus tensor
# for the material

def compute_strain(eigenstrain, gamma, Cijkl):

    resx = eigenstrain.shape[0]
    resy = eigenstrain.shape[1]
    resz = eigenstrain.shape[2]
    eps = make_permutation() # the standard permutation tensor
    kstrain = np.fft.fftn(eigenstrain, axes=[0,1,2])
    K = np.einsum('ijkl,nj,nl->nik',Cijkl,gamma,gamma)
    D = np.tile(np.einsum('mnl,im,in,il->i',
```

```python
                    eps,K[:,:,0],
                    K[:,:,1],
                    K[:,:,2]).reshape((K.shape[0],1,1,1)), (1,3,3,3))
N = 0.5*np.einsum('klm,nop,ilo,imp->ikn', eps,eps,K,K)
Nik = (np.einsum('mi,mjk->mijk',gamma,N) + np.einsum('mi,mjk->mjik',gamma,N))/D
Nik[np.logical_not(np.isfinite(Nik))] = 0
part_a = np.einsum('ijlm,klm->kij',Cijkl,kstrain.reshape((-1,3,3)))
part_b = np.einsum('kij,kj->ki',part_a, gamma)
part_c = np.einsum('mk,mijk->mij',part_b, Nik)
real_strains = np.real(np.fft.ifftn(part_c.reshape((resx,resy,resz,3,3)), axes=[0,1,2]))


return real_strains
```

APPENDIX C

Measuring Strain Fields in Particle Simulations

From a particle simulation, local strain is found by examining the neighbors of a given particle. In this way, single particles become the smallest unit of strain in the system, and every particle can be given a strain tensor describing its neighbor shell's deformation away from equilibrium. A least-squares fitting procedure is generally employed on the neighbor shell vectors to find a linear transform matrix to describe it.

Least-squares strain fitting requires a reference configuration [186]. If N_i is the number of neighbors of atom i and it remains unchanged through the distortion, then a matrix representing the separation of all neighbors from particle i can be defined as

$$d_{ji} = x_j - x_i \tag{C.1}$$

for all $j \in N_i$. Neighbors are often chosen to be all particles within a cutoff radius, frequently chosen to be between the first and second coordination shell, or else as the N_i nearest particles. In this work the first twelve nearest neighbors are chosen, which is commonly taken as the complete first neighbor shell in face centered crystals (FCC). Similar to above, the old separation in the reference state is

$$d_{ji}^0 = x_j^0 - x_i^0. \tag{C.2}$$

The strain describing this transformation will be an affine matrix J_i that best maps these sepa-

ration matrices

$$\{d_{ji^0}\} \rightarrow \{d_{ji}\}, \forall j \in N_i. \tag{C.3}$$

This can be expressed as

$$\sum_{j \in N_i} |\, d_{ji}^0 J_i - d_{ji}\,|^2 = \sum_{j \in N_i} \left(d_{ji}^0 J_i - d_{ji} \right) \left(d_{ji}^0 J_i - d_{ji} \right)^\top \tag{C.4}$$

$$= \sum_{j \in N_i} \mathrm{Tr} \left(\left(d_{ji}^0 J_i - d_{ji} \right)^\top \left(d_{ji}^0 J_i - d_{ji} \right) \right) \tag{C.5}$$

$$= \mathrm{Tr} \sum_{j \in N_i} \left(J_i^\top d_{ji}^{0\top} - d_{ji}^\top \right) \left(d_{ji}^0 J_i - d_{ji} \right). \tag{C.6}$$

By performing a matrix variation $\delta J_i^\top$ in the above expression:

$$0 = \mathrm{Tr} \sum_{j \in N_i} \delta J_i^\top d_{ji}^{0\top} \left(d_{ji}^0 J_i - d_{ji} \right) \tag{C.7}$$

$$= \mathrm{Tr}\, \delta J_i^\top \sum_{j \in N_i} d_{ji}^{0\top} \left(d_{ji}^0 J_i - d_{ji} \right). \tag{C.8}$$

This requires that the matrix

$$\sum_{j \in N_i} d_{ji}^{0\top} \left(d_{ji}^0 J_i - d_{ji} \right) \tag{C.9}$$

is zero for all $\delta J_i^\top$. So there must be:

$$\left(\sum_{j \in N_i} d_{ji}^{0\top} d_{ji}^0 \right) J_i = \sum_{j \in N_i} d_{ji}^{0\top} d_{ji}. \tag{C.10}$$

We can define

$$V_i = \sum_{j \in N_i} d_{ji}^{0\top} d_{ji}^0, \qquad W_i = \sum_{j \in N_i} d_{ji}^{0\top} d_{ji}. \tag{C.11}$$

Then the affine transformation is simply defined as

$$J_i = V_i^{-1} W_i \tag{C.12}$$

and the Lagrangian strain is found as

$$\eta_i = \frac{1}{2} \left(J_i J_i^\top - \mathcal{I} \right). \tag{C.13}$$

BIBLIOGRAPHY

[1] Brian Vincent. Introduction to Colloidal Dispersions. In *Colloid Science*, pages 1–13. John Wiley & Sons, Ltd, 2009.

[2] Sharon C. Glotzer and Michael J. Solomon. Anisotropy of building blocks and their assembly into complex structures. *Nature Materials*, 6(8):557, August 2007.

[3] Michael A. Boles, Michael Engel, and Dmitri V. Talapin. Self-Assembly of Colloidal Nanocrystals: From Intricate Structures to Functional Materials. *Chemical Reviews*, 116(18):11220–11289, September 2016.

[4] S. Alexander, P. M. Chaikin, P. Grant, G. J. Morales, P. Pincus, and D. Hone. Charge renormalization, osmotic pressure, and bulk modulus of colloidal crystals: Theory. *The Journal of Chemical Physics*, 80(11):5776–5781, June 1984.

[5] Z. W. Salsburg and W. W. Wood. Equation of State of Classical Hard Spheres at High Density. *The Journal of Chemical Physics*, 37(4):798–804, August 1962.

[6] Bo Li, Di Zhou, and Yilong Han. Assembly and phase transitions of colloidal crystals. *Nature Reviews Materials*, 1(2):15011, February 2016.

[7] Nikhil R. Jana. Shape Effect in Nanoparticle Self-Assembly. *Angewandte Chemie International Edition*, 43(12):1536–1540, 2004.

[8] Amir Haji-Akbari, Michael Engel, Aaron S. Keys, Xiaoyu Zheng, Rolfe G. Petschek, Peter Palffy-Muhoray, and Sharon C. Glotzer. Disordered, quasicrystalline and crystalline phases of densely packed tetrahedra. *Nature*, 462(7274):773–777, December 2009.

[9] Umang Agarwal and Fernando A. Escobedo. Mesophase behaviour of polyhedral particles. *Nature Materials*, 10(3):230–235, March 2011.

[10] Pablo F. Damasceno, Michael Engel, and Sharon C. Glotzer. Crystalline Assemblies and Densest Packings of a Family of Truncated Tetrahedra and the Role of Directional Entropic Forces. *ACS Nano*, 6(1):609–614, January 2012.

[11] Janne-Mieke Meijer, Fabian Hagemans, Laura Rossi, Dmytro V. Byelov, Sonja I.R. Castillo, Anatoly Snigirev, Irina Snigireva, Albert P. Philipse, and Andrei V. Petukhov. Self-Assembly of Colloidal Cubes via Vertical Deposition. *Langmuir*, 28(20):7631–7638, May 2012.

[12] Pablo F. Damasceno, Michael Engel, and Sharon C. Glotzer. Predictive Self-Assembly of Polyhedra into Complex Structures. *Science*, 337(6093):453–457, July 2012.

[13] Nikos Tasios, Anjan Prasad Gantapara, and Marjolein Dijkstra. Glassy dynamics of convex polyhedra. *The Journal of Chemical Physics*, 141(22):224502, December 2014.

[14] Daan Frenkel. Order through entropy. *Nature Materials*, 14:9–12, December 2014.

[15] A. T. Cadotte, J. Dshemuchadse, P. F. Damasceno, R. S. Newman, and S. C. Glotzer. Self-assembly of a space-tessellating structure in the binary system of hard tetrahedra and octahedra. *Soft Matter*, 12(34):7073–7078, August 2016.

[16] Sangmin Lee, Erin G. Teich, Michael Engel, and Sharon C. Glotzer. Entropic colloidal crystallization pathways via fluidfluid transitions and multidimensional prenucleation motifs. *Proceedings of the National Academy of Sciences*, 116(30):14843–14851, July 2019.

[17] Kyoungweon Park, Hilmar Koerner, and Richard A. Vaia. Depletion-Induced Shape and Size Selection of Gold Nanoparticles. *Nano Letters*, 10(4):1433–1439, April 2010.

[18] S. Sacanna, W. T. M. Irvine, P. M. Chaikin, and D. J. Pine. Lock and key colloids. *Nature*, 464(7288):575–578, March 2010.

[19] Greg van Anders, N. Khalid Ahmed, Ross Smith, Michael Engel, and Sharon C. Glotzer. Entropically Patchy Particles: Engineering Valence through Shape Entropy. *ACS Nano*, 8(1):931–940, January 2014.

[20] Andrew S. Karas, Jens Glaser, and Sharon C. Glotzer. Using depletion to control colloidal crystal assemblies of hard cuboctahedra. *Soft Matter*, 12(23):5199–5204, June 2016.

[21] Evelyn Auyeung, Ting I. N. G. Li, Andrew J. Senesi, Abrin L. Schmucker, Bridget C. Pals, Monica Olvera de la Cruz, and Chad A. Mirkin. DNA-mediated nanoparticle crystallization into Wulff polyhedra. *Nature*, 505(7481):73–77, January 2014.

[22] Yu Wang, Yufeng Wang, Xiaolong Zheng, tienne Ducrot, Jeremy S. Yodh, Marcus Weck, and David J. Pine. Crystallization of DNA-coated colloids. *Nature Communications*, 6:7253, June 2015.

[23] Haixin Lin, Sangmin Lee, Lin Sun, Matthew Spellings, Michael Engel, Sharon C. Glotzer, and Chad A. Mirkin. Clathrate colloidal crystals. *Science*, 355(6328):931–935, March 2017.

[24] tienne Ducrot, Mingxin He, Gi-Ra Yi, and David J. Pine. Colloidal alloys with preassembled clusters and spheres. *Nature Materials*, 16(6):652, June 2017.

[25] T. Gong and D. W. M. Marr. Electrically Switchable Colloidal Ordering in Confined Geometries. *Langmuir*, 17(8):2301–2304, April 2001.

[26] Simon O. Lumsdon, Eric W. Kaler, and Orlin D. Velev. Two-Dimensional Crystallization of Microspheres by a Coplanar AC Electric Field. *Langmuir*, 20(6):2108–2116, March 2004.

[27] Tara D. Edwards and Michael A. Bevan. Controlling Colloidal Particles with Electric Fields. *Langmuir*, 30(36):10793–10803, September 2014.

[28] Jrme J. Crassous, Adriana M. Mihut, Erik Wernersson, Patrick Pfleiderer, Jan Vermant, Per Linse, and Peter Schurtenberger. Field-induced assembly of colloidal ellipsoids into well-defined microtubules. *Nature Communications*, 5:5516, November 2014.

[29] Marek Grzelczak, Jan Vermant, Eric M. Furst, and Luis M. Liz-Marzn. Directed Self-Assembly of Nanoparticles. *ACS Nano*, 4(7):3591–3605, July 2010.

[30] R. S. Kshetrimayum. A brief intro to metamaterials. *IEEE Potentials*, 23(5):44–46, December 2005.

[31] Wenshan Cai and Vladimir M Shalaev. *Optical metamaterials*, volume 10. Springer, 2010.

[32] Xin Ren, Raj Das, Phuong Tran, Tuan Duc Ngo, and Yi Min Xie. Auxetic metamaterials and structures: a review. *Smart Materials and Structures*, 27(2):023001, January 2018.

[33] Ming-Hui Lu, Liang Feng, and Yan-Feng Chen. Phononic crystals and acoustic metamaterials. *Materials Today*, 12(12):34–42, December 2009.

[34] Wei Cheng, Jianjun Wang, Ulrich Jonas, George Fytas, and Nikolaos Stefanou. Observation and tuning of hypersonic bandgaps in colloidal crystals. *Nature Materials*, 5(10):830–836, October 2006.

[35] M. C. Marchetti, J. F. Joanny, S. Ramaswamy, T. B. Liverpool, J. Prost, Madan Rao, and R. Aditi Simha. Hydrodynamics of soft active matter. *Reviews of Modern Physics*, 85(3):1143–1189, July 2013.

[36] Jeremie Palacci, Stefano Sacanna, Asher Preska Steinberg, David J. Pine, and Paul M. Chaikin. Living Crystals of Light-Activated Colloidal Surfers. *Science*, 339(6122):936–940, February 2013.

[37] Jiangfan Yu, Ben Wang, Xingzhou Du, Qianqian Wang, and Li Zhang. Ultra-extensible ribbon-like magnetic microswarm. *Nature Communications*, 9(1):3260, August 2018.

[38] Ben Wang, Kai Fung Chan, Jiangfan Yu, Qianqian Wang, Lidong Yang, Philip Wai Yan Chiu, and Li Zhang. Reconfigurable Swarms of Ferromagnetic Colloids for Enhanced Local Hyperthermia. *Advanced Functional Materials*, 28(25):1705701, 2018.

[39] Berk Yigit, Yunus Alapan, and Metin Sitti. Programmable Collective Behavior in Dynamically Self-Assembled Mobile Microrobotic Swarms. *Advanced Science*, 6(6):1801837, 2019.

[40] Helena Massana-Cid, Fanlong Meng, Daiki Matsunaga, Ramin Golestanian, and Pietro Tierno. Tunable self-healing of magnetically propelling colloidal carpets. *Nature Communications*, 10(1):2444, June 2019.

[41] Hui Xie, Mengmeng Sun, Xinjian Fan, Zhihua Lin, Weinan Chen, Lei Wang, Lixin Dong, and Qiang He. Reconfigurable magnetic microrobot swarm: Multimode transformation, locomotion, and manipulation. *Science Robotics*, 4(28):eaav8006, March 2019.

[42] Jarad A. Mason, Christine R. Laramy, Cheng-Tsung Lai, Matthew N. OBrien, Qing-Yuan Lin, Vinayak P. Dravid, George C. Schatz, and Chad A. Mirkin. Contraction and Expansion of Stimuli-Responsive DNA Bonds in Flexible Colloidal Crystals. *Journal of the American Chemical Society*, 138(28):8722–8725, July 2016.

[43] Salman S. Rogers, Thomas A. Waigh, and Jian R. Lu. Intracellular Microrheology of Motile Amoeba proteus. *Biophysical Journal*, 94(8):3313–3322, April 2008.

[44] Daniel A. Fletcher and R. Dyche Mullins. Cell mechanics and the cytoskeleton. *Nature*, 463(7280):485, January 2010.

[45] Tim Sanchez, Daniel T. N. Chen, Stephen J. DeCamp, Michael Heymann, and Zvonimir Dogic. Spontaneous motion in hierarchically assembled active matter. *Nature*, 491(7424):431–434, November 2012.

[46] Andrea Al and Nader Engheta. Achieving transparency with plasmonic and metamaterial coatings. *Physical Review E*, 72(1):016623, July 2005.

[47] Jason Valentine, Jensen Li, Thomas Zentgraf, Guy Bartal, and Xiang Zhang. An optical cloak made of dielectrics. *Nature Materials*, 8(7):568–571, July 2009.

[48] J. B. Pendry. Negative Refraction Makes a Perfect Lens. *Physical Review Letters*, 85(18):3966–3969, October 2000.

[49] Jie Yao, Zhaowei Liu, Yongmin Liu, Yuan Wang, Cheng Sun, Guy Bartal, Angelica M. Stacy, and Xiang Zhang. Optical Negative Refraction in Bulk Metamaterials of Nanowires. *Science*, 321(5891):930–930, August 2008.

[50] Panmiao Liu, Ling Bai, Jianjun Yang, Hongcheng Gu, Qifeng Zhong, Zhuoying Xie, and Zhongze Gu. Self-assembled colloidal arrays for structural color. *Nanoscale Advances*, 1(5):1672–1685, May 2019.

[51] E. Yablonovitch. Photonic band-gap crystals. *Journal of Physics: Condensed Matter*, 5(16):2443–2460, April 1993.

[52] Thomas H. Courtney. *Mechanical Behavior of Materials: Second Edition*. Waveland Press, December 2005.

[53] I. Andonegui, I. Calvo, and A. J. Garcia-Adeva. Towards silicon all-optical nanophotonic circuitry. In *2014 16th International Conference on Transparent Optical Networks (ICTON)*, pages 1–4, July 2014.

[54] Stephanie A. Rinne, Florencio Garca-Santamara, and Paul V. Braun. Embedded cavities and waveguides in three-dimensional silicon photonic crystals. *Nature Photonics*, 2(1):52–56, January 2008.

[55] Susumu Noda, Alongkarn Chutinan, and Masahiro Imada. Trapping and emission of photons by a single defect in a photonic bandgap structure. *Nature*, 407(6804):608–610, October 2000.

[56] Larry A. Coldren, Scott W. Corzine, and Milan L. Mashanovitch. *Diode Lasers and Photonic Integrated Circuits*. John Wiley & Sons, March 2012. Google-Books-ID: D6Ub126rtPoC.

[57] Ya-nan Zhang, Yong Zhao, and Ri-qing Lv. A review for optical sensors based on photonic crystal cavities. *Sensors and Actuators A: Physical*, 233:374–389, September 2015.

[58] Arthur R. McGurn. Photonic crystal circuits: Localized modes and waveguide couplers. *Physical Review B*, 65(7):075406, January 2002.

[59] Vito Volterra. Sur l'quilibre des corps lastiques multiplement connexes. *Annales scientifiques de l'cole normale suprieure*, 24:401–517, 1907.

[60] A. E. H. Love. *A Treatise on the Mathematical Theory of Elasticity*. Cambridge University Press, January 2013. Google-Books-ID: JFTbrz0Fs5UC.

[61] J Frenkel. The theory of the elastic limit and the solidity of crystal bodies. *Z Phys*, 37:572–609, 1926.

[62] E. Orowan. Zur Kristallplastizität. I. *Zeitschrift für Physik*, 89(9-10):605–613, September 1934.

[63] Taylor Geoffrey Ingram. The mechanism of plastic deformation of crystals. Part I.Theoretical. *Proceedings of the Royal Society of London. Series A, Containing Papers of a Mathematical and Physical Character*, 145(855):362–387, July 1934.

[64] M. Polanyi. ber eine Art Gitterstrung, die einen Kristall plastisch machen knnte. *Zeitschrift fr Physik*, 89(9):660–664, September 1934.

[65] J. M. Burgers. Physics. Some considerations on the fields of stress connected with dislocations in a regular crystal lattice. I. In F. T. M. Nieuwstadt and J. A. Steketee, editors, *Selected Papers of J. M. Burgers*, pages 335–389. Springer Netherlands, Dordrecht, 1995.

[66] J. Friedel. Chapter i - definition and examples. In J. Friedel, editor, *Dislocations*, International Series of Monographs on Solid State Physics, pages 3 – 16aa. Pergamon, 1964.

[67] John Hirth and Lothe, Jens. *Theory of Dislocations*. Wiley Interscience, New York, 2nd edition, 1982.

[68] Christopher A. Schuh. Nanoindentation studies of materials. *Materials Today*, 9(5):32–40, May 2006.

[69] Peter Schall, Itai Cohen, David A. Weitz, and Frans Spaepen. Visualization of Dislocation Dynamics in Colloidal Crystals. *Science*, 305(5692):1944–1948, September 2004.

[70] Peter Schall, Itai Cohen, David A. Weitz, and Frans Spaepen. Visualizing dislocation nucleation by indenting colloidal crystals. *Nature*, 440(7082):319–323, March 2006.

[71] Neil Y. C. Lin, Matthew Bierbaum, Peter Schall, James P. Sethna, and Itai Cohen. Measuring nonlinear stresses generated by defects in 3d colloidal crystals. *Nature Materials*, 15(11):1172–1176, November 2016.

[72] William T. M. Irvine, Vincenzo Vitelli, and Paul M. Chaikin. Pleats in crystals on curved surfaces. *Nature*, 468(7326):947, December 2010.

[73] William T. M. Irvine, Andrew D. Hollingsworth, David G. Grier, and Paul M. Chaikin. Dislocation reactions, grain boundaries, and irreversibility in two-dimensional lattices using topological tweezers. *Proceedings of the National Academy of Sciences*, 110(39):15544–15548, September 2013.

[74] Franois A. Lavergne, Arran Curran, Dirk G. A. L. Aarts, and Roel P. A. Dullens. Dislocation-controlled formation and kinetics of grain boundary loops in two-dimensional crystals. *Proceedings of the National Academy of Sciences*, 115(27):6922–6927, July 2018.

[75] B. van der Meer, L. Filion, and M. Dijkstra. Fabricating large two-dimensional single colloidal crystals by doping with active particles. *Soft Matter*, 12(14):3406–3411, March 2016.

[76] B. van der Meer, M. Dijkstra, and L. Filion. Removing grain boundaries from three-dimensional colloidal crystals using active dopants. *Soft Matter*, 12(25):5630–5635, June 2016.

[77] Kilian Dietrich, Giovanni Volpe, Muhammad Nasruddin Sulaiman, Damian Renggli, Ivo Buttinoni, and Lucio Isa. Active Atoms and Interstitials in Two-Dimensional Colloidal Crystals. *Physical Review Letters*, 120(26):268004, June 2018.

[78] Sophie Ramananarivo, Etienne Ducrot, and Jeremie Palacci. Activity-controlled annealing of colloidal monolayers. *Nature Communications*, 10(1):1–8, July 2019.

[79] Bryan VanSaders, Julia Dshemuchadse, and Sharon C. Glotzer. Strain fields in repulsive colloidal crystals. *Physical Review Materials*, 2(6):063604, June 2018.

[80] Bryan VanSaders and Sharon C. Glotzer. Designing active particles for colloidal microstructure manipulation via strain field alchemy. *Soft Matter*, July 2019.

[81] Bryan VanSaders and Sharon C. Glotzer. Pinning colloidal dislocations with active particles that seek stacking faults. *In preparation*.

[82] Bryan VanSaders and Sharon C. Glotzer. Engineering dislocation pair creation to reconfigure colloidal matter. *In preparation*.

[83] Daan Frenkel and Berend Smit. *Understanding Molecular Simulation*. Elsevier, 2002.

[84] Glenn J. Martyna, Mark E. Tuckerman, Douglas J. Tobias, and Michael L. Klein. Explicit reversible integrators for extended systems dynamics. *Molecular Physics*, 87(5):1117–1157, April 1996.

[85] Duane C. Wallace. *Thermodynamics of Crystals*. Wiley, New York, 1972.

[86] M. Parrinello and A. Rahman. Strain fluctuations and elastic constants. *The Journal of Chemical Physics*, 76(5):2662–2666, 1982.

[87] Woldemar Voigt. *Lehrbuch der kristallphysik (mit ausschluss der kristalloptik)*. Leipzig, Berlin, B.G. Teubner, 1910.

[88] Andrei A. Gusev, Marcel M. Zehnder, and Ulrich W. Suter. Fluctuation formula for elastic constants. *Phys. Rev. B*, 54:1–4, Jul 1996.

[89] Ivar Fredholm. Sur les équations de l'équilibre d'un corps solide élastique. *Acta Mathematica*, 23(1):1–42, December 1900.

[90] Toshio Mura. General theory of eigenstrains. In *Micromechanics of defects in solids*, number 3 in Mechanics of Elastic and Inelastic Solids, pages 1–73. Springer Netherlands, 1987.

[91] Dmytro Nykypanchuk, Mathew M. Maye, Daniel van der Lelie, and Oleg Gang. DNA-guided crystallization of colloidal nanoparticles. *Nature*, 451(7178):549, January 2008.

[92] Stefano Sacanna and David J. Pine. Shape-anisotropic colloids: Building blocks for complex assemblies. *Current Opinion in Colloid & Interface Science*, 16(2):96–105, April 2011.

[93] Qian Chen, Sung Chul Bae, and Steve Granick. Directed self-assembly of a colloidal kagome lattice. *Nature*, 469(7330):381, January 2011.

[94] Yugang Zhang, Fang Lu, Kevin G. Yager, Daniel van der Lelie, and Oleg Gang. A general strategy for the DNA-mediated self-assembly of functional nanoparticles into heterogeneous systems. *Nature Nanotechnology*, 8(11):865, November 2013.

[95] Greg van Anders, Daphne Klotsa, Andrew S. Karas, Paul M. Dodd, and Sharon C. Glotzer. Digital Alchemy for Materials Design: Colloids and Beyond. *ACS Nano*, 9(10):9542–9553, October 2015.

[96] Sanat K. Kumar, Guruswamy Kumaraswamy, Bhagavatula L. V. Prasad, Rajdip Bandyopadhyaya, Steve Granick, Oleg Gang, Vinothan N. Manoharan, Daan Frenkel, and Nicholas A. Kotov. Nanoparticle assembly: A perspective and some unanswered questions. *Current Science*, 112(8):1635–1641, April 2017.

[97] Berend van der Meer, Marjolein Dijkstra, and Laura Filion. Diffusion and interactions of point defects in hard-sphere crystals. *The Journal of Chemical Physics*, 146(24):244905, June 2017.

[98] Eli Yablonovitch. Inhibited Spontaneous Emission in Solid-State Physics and Electronics. *Physical Review Letters*, 58(20):2059–2062, May 1987.

[99] E. Yablonovitch, T. J. Gmitter, and K. M. Leung. Photonic band structure: The face-centered-cubic case employing nonspherical atoms. *Physical Review Letters*, 67(17):2295–2298, October 1991.

[100] Martin Maldovan and Edwin L. Thomas. Diamond-structured photonic crystals. *Nature Materials*, 3(9):593, September 2004.

[101] K. M. Ho, C. T. Chan, and C. M. Soukoulis. Existence of a photonic gap in periodic dielectric structures. *Physical Review Letters*, 65(25):3152–3155, December 1990.

[102] Youngeun Kim, Robert J. Macfarlane, Matthew R. Jones, and Chad A. Mirkin. Transmutable nanoparticles with reconfigurable surface ligands. *Science*, 351(6273):579–582, February 2016.

[103] Konstantin V. Tretiakov and Krzysztof W. Wojciechowski. Partially auxetic behavior in fcc crystals of hard-core repulsive Yukawa particles. *physica status solidi (b)*, 251(2):383–387, February 2014.

[104] E. Zaccarelli, G. Foffi, K. A. Dawson, F. Sciortino, and P. Tartaglia. Mechanical properties of a model of attractive colloidal solutions. *Physical Review E*, 63(3):031501, February 2001.

[105] Alessio Zaccone, Hua Wu, and Emanuela Del Gado. Elasticity of Arrested Short-Ranged Attractive Colloids: Homogeneous and Heterogeneous Glasses. *Physical Review Letters*, 103(20):208301, November 2009.

[106] Gregory M. Grason. Perspective: Geometrically frustrated assemblies. *The Journal of Chemical Physics*, 145(11):110901, September 2016.

[107] Guangnan Meng, Jayson Paulose, David R. Nelson, and Vinothan N. Manoharan. Elastic Instability of a Crystal Growing on a Curved Surface. *Science*, 343(6171):634–637, February 2014.

[108] Amir Azadi and Gregory M. Grason. Emergent Structure of Multidislocation Ground States in Curved Crystals. *Physical Review Letters*, 112(22):225502, June 2014.

[109] Zhenwei Yao. Topological vacancies in spherical crystals. *Soft Matter*, 13(35):5905–5910, 2017.

[110] J. E. Jones and D. Sc. On the determination of molecular fields. —II. From the equation of state of a gas. *Proc. R. Soc. Lond. A*, 106(738):463–477, October 1924.

[111] John Weeks, David Chandler, and Hans C. Andersen. Role of Repulsive Forces in Determining the Equilibrium Structure of Simple Liquids. *The Journal of Chemical Physics*, 54(12):5237–5247, June 1971.

[112] Joshua A. Anderson, Chris D. Lorenz, and A. Travesset. General purpose molecular dynamics simulations fully implemented on graphics processing units. *Journal of Computational Physics*, 227(10):5342–5359, May 2008.

[113] Jens Glaser, Trung Dac Nguyen, Joshua A. Anderson, Pak Lui, Filippo Spiga, Jaime A. Millan, David C. Morse, and Sharon C. Glotzer. Strong scaling of general-purpose molecular dynamics simulations on GPUs. *Computer Physics Communications*, 192(Supplement C):97–107, July 2015.

[114] Y. P. Chiu. On the Stress Field Due to Initial Strains in a Cuboid Surrounded by an Infinite Elastic Space. *Journal of Applied Mechanics*, 44(4):587–590, December 1977.

[115] Murray S. Daw. Elasticity effects in electronic structure calculations with periodic boundary conditions. *Computational Materials Science*, 38(2):293–297, December 2006.

[116] Konstantin V. Tretiakov and Krzysztof W. Wojciechowski. Quick and accurate estimation of the elastic constants using the minimum image method. *Computer Physics Communications*, 189:77–83, April 2015.

[117] Alexander Stukowski. Visualization and analysis of atomistic simulation data with OVITO– the Open Visualization Tool. *Modelling and Simulation in Materials Science and Engineering*, 18(1):015012, 2010.

[118] Bradley Efron and R. J. Tibshirani. *An Introduction to the Bootstrap*. CRC Press, May 1994. Google-Books-ID: gLlpIUxRntoC.

[119] A. Stukowski and A. Arsenlis. On the elastic–plastic decomposition of crystal deformation at the atomic scale. *Modelling and Simulation in Materials Science and Engineering*, 20(3):035012, 2012.

[120] Sander Pronk and Daan Frenkel. Can stacking faults in hard-sphere crystals anneal out spontaneously? *The Journal of Chemical Physics*, 110(9):4589–4592, March 1999.

[121] D. C. Chrzan, M. P. Sherburne, Y. Hanlumyuang, T. Li, and J. W. Morris. Spreading of dislocation cores in elastically anisotropic body-centered-cubic materials: The case of gum metal. *Physical Review B*, 82(18):184202, November 2010.

[122] Y. T. Chou and G. T. Sha. ¡110¿ Dislocation in Cubic Crystals. *Journal of Applied Physics*, 42(7):2625–2631, June 1971.

[123] D. Roundy, C. R. Krenn, Marvin L. Cohen, and J. W. Morris. Ideal Shear Strengths of fcc Aluminum and Copper. *Physical Review Letters*, 82(13):2713–2716, March 1999.

[124] Krassimir P. Velikov, Christina G. Christova, Roel P. A. Dullens, and Alfons van Blaaderen. Layer-by-Layer Growth of Binary Colloidal Crystals. *Science*, 296(5565):106–109, April 2002.

[125] Mirjam E. Leunissen, Christina G. Christova, Antti-Pekka Hynninen, C. Patrick Royall, Andrew I. Campbell, Arnout Imhof, Marjolein Dijkstra, Ren van Roij, and Alfons van Blaaderen. Ionic colloidal crystals of oppositely charged particles. *Nature*, 437(7056):235, September 2005.

[126] Karol Miszta, Joost de Graaf, Giovanni Bertoni, Dirk Dorfs, Rosaria Brescia, Sergio Marras, Luca Ceseracciu, Roberto Cingolani, Ren van Roij, Marjolein Dijkstra, and Liberato Manna. Hierarchical self-assembly of suspended branched colloidal nanocrystals into superlattice structures. *Nature Materials*, 10(11):872–876, November 2011.

[127] Teun Vissers, Zdenk Preisler, Frank Smallenburg, Marjolein Dijkstra, and Francesco Sciortino. Predicting crystals of Janus colloids. *The Journal of Chemical Physics*, 138(16):164505, April 2013.

[128] Lei Lu, Yongfeng Shen, Xianhua Chen, Lihua Qian, and K. Lu. Ultrahigh Strength and High Electrical Conductivity in Copper. *Science*, 304(5669):422–426, April 2004.

[129] O. Painter, R. K. Lee, A. Scherer, A. Yariv, J. D. O'Brien, P. D. Dapkus, and I. Kim. Two-Dimensional Photonic Band-Gap Defect Mode Laser. *Science*, 284(5421):1819–1821, June 1999.

[130] Yoshihiro Akahane, Takashi Asano, Bong-Shik Song, and Susumu Noda. High-*Q* photonic nanocavity in a two-dimensional photonic crystal. *Nature*, 425(6961):944–947, October 2003.

[131] P. W. Voorhees. The theory of Ostwald ripening. *Journal of Statistical Physics*, 38(1):231–252, January 1985.

[132] Morris E. Fine. Precipitation hardening of aluminum alloys. *Metallurgical Transactions A*, 6(4):625, April 1975.

[133] John W. Cahn. Phase Separation by Spinodal Decomposition in Isotropic Systems. *The Journal of Chemical Physics*, 42(1):93–99, January 1965.

[134] J. W. Matthews and A. E. Blakeslee. Defects in epitaxial multilayers: I. Misfit dislocations. *Journal of Crystal Growth*, 27:118–125, December 1974.

[135] P. Bellon. Nonequilibrium Roughening and Faceting of Interfaces in Driven Alloys. *Physical Review Letters*, 81(19):4176–4179, November 1998.

[136] Raúl A. Enrique and Pascal Bellon. Compositional patterning in immiscible alloys driven by irradiation. *Physical Review B*, 63(13):134111, March 2001.

[137] Alan C. Lund and Christopher A. Schuh. Driven Alloys in the Athermal Limit. *Physical Review Letters*, 91(23):235505, December 2003.

[138] A. R. Bausch, M. J. Bowick, A. Cacciuto, A. D. Dinsmore, M. F. Hsu, D. R. Nelson, M. G. Nikolaides, A. Travesset, and D. A. Weitz. Grain Boundary Scars and Spherical Crystallography. *Science*, 299(5613):1716–1718, March 2003.

[139] K. Hima Nagamanasa, Shreyas Gokhale, Rajesh Ganapathy, and A. K. Sood. Confined glassy dynamics at grain boundaries in colloidal crystals. *Proceedings of the National Academy of Sciences of the United States of America*, 108(28):11323–11326, 2011.

[140] Volkert W. A. de Villeneuve, Roel P. A. Dullens, Dirk G. A. L. Aarts, Esther Groeneveld, Johannes H. Scherff, Willem K. Kegel, and Henk N. W. Lekkerkerker. Colloidal Hard-Sphere Crystal Growth Frustrated by Large Spherical Impurities. *Science*, 309(5738):1231–1233, August 2005.

[141] Sharon J. Gerbode, Stephanie H. Lee, Chekesha M. Liddell, and Itai Cohen. Restricted Dislocation Motion in Crystals of Colloidal Dimer Particles. *Physical Review Letters*, 101(5):058302, August 2008.

[142] Alfons van Blaaderen, Rene Ruel, and Pierre Wiltzius. Template-directed colloidal crystallization. *Nature*, 385(6614):321–324, January 1997.

[143] Tonnishtha Dasgupta, John R. Edison, and Marjolein Dijkstra. Growth of defect-free colloidal hard-sphere crystals using colloidal epitaxy. *The Journal of Chemical Physics*, 146(7):074903, February 2017.

[144] Volkert W. A. de Villeneuve, Leonie Derendorp, Danny Verboekend, Esther C. M.Vermolen, Willem K.Kegel, Henk N. W.Lekkerkerker, and Roel P. A.Dullens. Grain boundary pinning in doped hard sphere crystals. *Soft Matter*, 5(12):2448–2452, 2009.

[145] Caitlin E. Cash, Jeremy Wang, Maya M. Martirossyan, B. Kemper Ludlow, Alejandro E. Baptista, Nina M. Brown, Eli J. Weissler, Jatin Abacousnac, and Sharon J. Gerbode. Local Melting Attracts Grain Boundaries in Colloidal Polycrystals. *Physical Review Letters*, 120(1):018002, January 2018.

[146] Andrea R. Tao, Susan Habas, and Peidong Yang. Shape Control of Colloidal Metal Nanocrystals. *Small*, 4(3):310–325, 2008.

[147] Soshan Cheong, John D.Watt, and Richard D.Tilley. Shape control of platinum and palladium nanoparticles for catalysis. *Nanoscale*, 2(10):2045–2053, 2010.

[148] Marek Grzelczak, Jorge Prez-Juste, Paul Mulvaney, and Luis M.Liz-Marzn. Shape control in gold nanoparticle synthesis. *Chemical Society Reviews*, 37(9):1783–1791, 2008.

[149] Trung Dac Nguyen, Carolyn L. Phillips, Joshua A. Anderson, and Sharon C. Glotzer. Rigid body constraints realized in massively-parallel molecular dynamics on graphics processing units. *Computer Physics Communications*, 182(11):2307–2313, November 2011.

[150] H. Risken and H. D. Vollmer. Brownian motion in periodic potentials; nonlinear response to an external force. *Zeitschrift fr Physik B Condensed Matter*, 33(3):297–305, September 1979.

[151] Alexander Stukowski and Karsten Albe. Extracting dislocations and non-dislocation crystal defects from atomistic simulation data. *Modelling and Simulation in Materials Science and Engineering*, 18(8):085001, 2010.

[152] Shuguang Li, Richa Batra, David Brown, Hyun-Dong Chang, Nikhil Ranganathan, Chuck Hoberman, Daniela Rus, and Hod Lipson. Particle robotics based on statistical mechanics of loosely coupled components. *Nature*, 567(7748):361, March 2019.

[153] A. H. Cottrell and B. A. Bilby. Dislocation Theory of Yielding and Strain Ageing of Iron. *Proceedings of the Physical Society. Section A*, 62(1):49, 1949.

[154] H. Yoshinaga and S. Morozumi. The solute atmosphere round a moving dislocation and its dragging stress. *The Philosophical Magazine: A Journal of Theoretical Experimental and Applied Physics*, 23(186):1367–1385, June 1971.

[155] Yue Fan, Yuri N. Osetskiy, Sidney Yip, and Bilge Yildiz. Mapping strain rate dependence of dislocation-defect interactions by atomistic simulations. *Proceedings of the National Academy of Sciences*, 110(44):17756–17761, 2013.

[156] Frdric Cazals and Tom Dreyfus. The structural bioinformatics library: modeling in biomolecular science and beyond. *Bioinformatics*, 33(7):997–1004, April 2017.

[157] David Chandler. *Introduction to modern statistical mechanics*. Oxford University Press, New York, 1985.

[158] G. M. Viswanathan, Sergey V. Buldyrev, Shlomo Havlin, M. G. E. da Luz, E. P. Raposo, and H. Eugene Stanley. Optimizing the success of random searches. *Nature*, 401(6756):911–914, October 1999.

[159] Frederic Bartumeus, Francesc Peters, Salvador Pueyo, Clia Marras, and Jordi Catalan. Helical Lvy walks: Adjusting searching statistics to resource availability in microzooplankton. *Proceedings of the National Academy of Sciences*, 100(22):12771–12775, October 2003.

[160] A. M. Reynolds and C. J. Rhodes. The Lvy flight paradigm: random search patterns and mechanisms. *Ecology*, 90(4):877–887, 2009.

[161] Nicolas E. Humphries, Henri Weimerskirch, Nuno Queiroz, Emily J. Southall, and David W. Sims. Foraging success of biological Lvy flights recorded in situ. *Proceedings of the National Academy of Sciences*, 109(19):7169–7174, May 2012.

[162] Hseyin Hakl and Harun Uuz. A novel particle swarm optimization algorithm with Levy flight. *Applied Soft Computing*, 23:333–345, October 2014.

[163] Jean-Franois Rupprecht, Olivier Bnichou, and Raphael Voituriez. Optimal search strategies of run-and-tumble walks. *Physical Review E*, 94(1):012117, July 2016.

[164] Qian Yu, Liang Qi, Tomohito Tsuru, Rachel Traylor, David Rugg, J. W. Morris, Mark Asta, D. C. Chrzan, and Andrew M. Minor. Origin of dramatic oxygen solute strengthening effect in titanium. *Science*, 347(6222):635–639, February 2015.

[165] Frank R. N. Nabarro and John P. Hirth, editors. *Dislocations in Solids*, volume 12. North Holland, 1 edition, August 2004.

[166] H. O. Moser, B. D. F. Casse, O. Wilhelmi, and B. T. Saw. Terahertz Response of a Microfabricated Rod–Split-Ring-Resonator Electromagnetic Metamaterial. *Physical Review Letters*, 94(6):063901, February 2005.

[167] Alberto Brunete, Avinash Ranganath, Sergio Segovia, Javier Perez de Frutos, Miguel Hernando, and Ernesto Gambao. Current trends in reconfigurable modular robots design. *International Journal of Advanced Robotic Systems*, 14(3):1729881417710457, May 2017.

[168] Daniela Rus and Marsette Vona. Crystalline Robots: Self-Reconfiguration with Compressible Unit Modules. *Autonomous Robots*, 10(1):107–124, January 2001.

[169] J. W. Suh, S. B. Homans, and M. Yim. Telecubes: mechanical design of a module for self-reconfigurable robotics. In *Proceedings 2002 IEEE International Conference on Robotics and Automation (Cat. No.02CH37292)*, volume 4, pages 4095–4101 vol.4, May 2002.

[170] K. Gilpin, A. Knaian, and D. Rus. Robot pebbles: One centimeter modules for programmable matter through self-disassembly. In *2010 IEEE International Conference on Robotics and Automation*, pages 2485–2492, May 2010.

[171] S. C. Goldstein, J. D. Campbell, and T. C. Mowry. Programmable matter. *Computer*, 38(6):99–101, May 2005.

[172] M. Shimizu, A. Ishiguro, and T. Kawakatsu. Slimebot: A Modular Robot That Exploits Emergent Phenomena. In *Proceedings of the 2005 IEEE International Conference on Robotics and Automation*, pages 2982–2987, April 2005.

[173] Robert Fitch and Zack Butler. Million Module March: Scalable Locomotion for Large Self-Reconfiguring Robots. *The International Journal of Robotics Research*, 27(3-4):331–343, March 2008.

[174] Greg Aloupis, Sbastien Collette, Mirela Damian, Erik D. Demaine, Robin Flatland, Stefan Langerman, Joseph O'Rourke, Suneeta Ramaswami, Vera Sacristn, and Stefanie Wuhrer. Linear reconfiguration of cube-style modular robots. *Computational Geometry*, 42(6):652–663, August 2009.

[175] Jakub Lengiewicz and Pawe Hoobut. Efficient collective shape shifting and locomotion of massively-modular robotic structures. *Autonomous Robots*, 43(1):97–122, January 2019.

[176] Michael Rubenstein, Alejandro Cornejo, and Radhika Nagpal. Programmable self-assembly in a thousand-robot swarm. *Science*, 345(6198):795–799, August 2014.

[177] Alicia Altemose, Mara Antonieta SnchezFarrn, Wentao Duan, Steve Schulz, Ali Borhan, Vincent H. Crespi, and Ayusman Sen. Chemically Controlled Spatiotemporal Oscillations of Colloidal Assemblies. *Angewandte Chemie International Edition*, 56(27):7817–7821, 2017.

[178] Jingyan Zhang, Xiaoze Jiang, Yanfeng Zhang, Yuting Li, and Shiyong Liu. Facile Fabrication of Reversible Core Cross-Linked Micelles Possessing Thermosensitive Swellability. *Macromolecules*, 40(25):9125–9132, December 2007.

[179] Xiaoze Jiang, Zhishen Ge, Jian Xu, Hao Liu, and Shiyong Liu. Fabrication of Multiresponsive Shell Cross-Linked Micelles Possessing pH-Controllable Core Swellability and Thermo-Tunable Corona Permeability. *Biomacromolecules*, 8(10):3184–3192, October 2007.

[180] Heinz R. Paneth. The Mechanism of Self-Diffusion in Alkali Metals. *Physical Review*, 80(4):708–711, November 1950.

[181] Frank Smallenburg, Laura Filion, Matthieu Marechal, and Marjolein Dijkstra. Vacancy-stabilized crystalline order in hard cubes. *Proceedings of the National Academy of Sciences*, 109(44):17886–17890, October 2012.

[182] B. van der Meer, R. van Damme, M. Dijkstra, F. Smallenburg, and L. Filion. Revealing a Vacancy Analog of the Crowdion Interstitial in Simple Cubic Crystals. *Physical Review Letters*, 121(25):258001, December 2018.

[183] K. Stoy and R. Nagpal. Self-repair through scale independent self-reconfiguration. In *2004 IEEE/RSJ International Conference on Intelligent Robots and Systems (IROS) (IEEE Cat. No.04CH37566)*, volume 2, pages 2062–2067 vol.2, September 2004.

[184] M. De Rosa, S. Goldstein, Peter Lee, J. Campbell, and P. Pillai. Scalable shape sculpting via hole motion: motion planning in lattice-constrained modular robots. In *Proceedings 2006 IEEE International Conference on Robotics and Automation, 2006. ICRA 2006.*, pages 1462–1468, May 2006.

[185] D. J. Dewey, M. P. Ashley-Rollman, M. De Rosa, S. C. Goldstein, T. C. Mowry, S. S. Srinivasa, P. Pillai, and J. Campbell. Generalizing metamodules to simplify planning in modular robotic systems. In *2008 IEEE/RSJ International Conference on Intelligent Robots and Systems*, pages 1338–1345, September 2008.

[186] Ju Li. *Atomistic Visualization*, pages 1051–1068. Springer Netherlands, Dordrecht, 2005.